

Simultaneous Measurements of Secondary Gamma Rays and Neutrons from Fast Neutron
Scattering on ^{56}Fe with GENESIS

By

Joseph Michael Gordon

A dissertation submitted in partial satisfaction of the

requirements for the degree of

Doctor of Philosophy

in

Engineering - Nuclear Engineering

in the

Graduate Division

of the

University of California, Berkeley

Committee in charge:

Professor Lee Bernstein, Co-chair
Professor Bethany Goldblum, Co-chair
Professor Kai Vetter
Professor Gabriel Orebi Gann

Fall 2023

Simultaneous Measurements of Secondary Gamma Rays and Neutrons from Fast Neutron
Scattering on ^{56}Fe with GENESIS

Copyright 2023
By
Joseph Michael Gordon

Abstract

Simultaneous Measurements of Secondary Gamma Rays and Neutrons from Fast Neutron Scattering on ^{56}Fe with GENESIS

By

Joseph Michael Gordon

Doctor of Philosophy in Engineering - Nuclear Engineering

University of California, Berkeley

Professor Lee Bernstein, Co-chair

Professor Bethany Goldblum, Co-chair

Improved inelastic neutron scattering and neutron-induced gamma ray production data are needed for many of the next generation nuclear technologies, from advanced reactors to space exploration, shielding applications, and detection platforms based on prompt neutron interrogation analysis. The data for these applications come from evaluated libraries like ENDF/B-VIII.0, which are derived from calculations that have been validated against measurements of reaction cross sections and a set of standard benchmarks. Historically, the generation of these libraries has relied on the separate measurements of the outgoing neutrons and γ -rays from $(n, n'\gamma)$. The Gamma Energy Neutron Energy Spectrometer for Inelastic Scattering (GENESIS) located at the 88-Inch Cyclotron at Lawrence Berkeley National Laboratory (LBNL) is an experimental platform containing organic liquid scintillators for measurements of secondary neutron energy and angle distributions and high-purity germanium (HPGe) detectors for simultaneous measurements of gamma-ray production cross sections. The array attempts to bridge the gap between evaluators and experimentalists and produce nuclear data of maximal utility via the simultaneous measurement and a nuclear reaction modeling based analysis approach.

The establishment of GENESIS as viable experimental platform was accomplished through a series of calibrated source and beam measurements. The characteristics of this array were measured, including the timing resolution and delays of each detector and the energy and light yield resolution and gain of the detectors. The efficiency of the HPGe CLOVER detectors was measured experimentally using a calibrated ^{152}Eu point source and an elliptical ^{56}Mn sample. A GEANT4 model of the CLOVERs was developed and validated against the efficiency measurements to within 5% allowing for calculations of single leaf or full-CLOVER efficiency for different target geometries and gamma ray energies. The neutron energy and

light yield dependent response of the neutron detectors was investigated using spontaneous fission neutrons from an encapsulated ^{252}Cf spontaneous fission source. A GEANT4 model of the array, including the CLOVERs, organic scintillators, and support structures was developed to calculate the absolute in-situ efficiency of the neutron detectors. This simulation was validated against the measurements carried out with the ^{252}Cf source to within 5%.

Experiments with a 99.98%-enriched ^{56}Fe target were performed using GENESIS with a broad-energy, collimated, time-resolved neutron beam generated via the break-up of 14 MeV deuterons in a thick carbon target. Two analysis techniques were pursued, including a novel forward-modeling approach enabled by the well validated GEANT4 simulation and a new C++ interface to the nuclear reaction code TALYS. Differential gamma-ray production cross sections for the yrast¹ $4 \rightarrow 2$ and $6 \rightarrow 4$ transitions, and 8 other off-yrast transitions were obtained using conventional analysis techniques. The yrast $2 \rightarrow 0$ gamma ray production cross section was determined using the forward modeling approach. Total secondary neutron energy/angular distributions as a function of incident neutron energy were also obtained using the forward-modeling approach. The results of the forward modeling approach were found to be in agreement with the results obtainable through conventional means and to previous measurements found in the literature. This work establishes the forward modeling analysis approach as a valid method to obtain cross sections with GENESIS. Finally, the possibilities for analyses of secondary neutron/gamma coincidences in the ^{56}Fe data and the prospects for coincidence analysis in future GENESIS experiments is discussed.

¹States with the lowest ratio of excitation energy to total angular momentum.

Observation is a thousand times more difficult, error perhaps a condition of observation in general. ²

²Friedrich Nietzsche, trans. Walter Kaufmann. "Book III: Principles of a New Evaluation, Part 2: The Epistemological Starting Point No. 472" *Will to Power*

Contents

Contents	ii
List of Figures	iv
List of Tables	xi
1 Introduction	1
1.1 Motivation	1
1.2 Past Measurements	3
1.3 GENESIS: A New Experimental Platform	4
2 Experimental Design	6
2.1 Neutron Beam Characteristics	6
2.2 Fast neutron detection with organic liquid scintillators	9
2.3 Gamma-ray detection with HPGe CLOVER detectors	12
2.4 Data Acquisition	14
3 Array Characteristics	19
3.1 Event Timing	19
3.2 Energy Resolution and Gain Calibration	22
3.3 Detection Efficiency: Experiment and Modeling	27
4 Neutron Scattering Cross Sections: Theory and Modeling	41
4.1 Theoretical Background	41
4.2 Reaction Modeling with TALYS	46
5 Measuring Reaction Cross Sections with GENESIS	53
5.1 Traditional Approach	53
5.2 Forward Modeling	54
5.3 Source Term Modeling with TALYS	62
6 ^{56}Fe Experimental Campaign	66
6.1 Target Characterization	67

6.2	Data Acquisition Issues	68
6.3	Activation Foil Analysis	70
7	Secondary Neutron Distributions	73
7.1	Data Analysis	73
7.2	Results	78
8	Gamma-ray Production	82
8.1	Data Analysis	82
8.2	Results	87
9	Towards $n - \gamma$ Coincidence Measurements	98
10	Conclusion	103
	Bibliography	107
A	Scintillator Locations	114

List of Figures

2.1	Current 14 MeV TTDB on Carbon neutron spectrum for the June '21 GENESIS experiment measured using the sToF detector. The x-errors are the bin widths, which were set to $\sigma/3$ of the incoming TOF resolution. The y-errors represent the statistical uncertainty.	7
2.2	Overhead view of a portion of the 88-Inch Cyclotron, deuteron breakup target, and copper collimator which are located in the vault. GENESIS is located in Cave 5 and downstream of the GENESIS array is the sToF neutron beam monitor.	8
2.3	A view looking downstream, lower right to upper left, at GENESIS, including A) Eurisys HPGe CLOVER detectors with BGO anti-Compton shields, B) an Ortec PopTop HPGe detector, C) the sToF neutron beam monitor, D) a Saint-Gobain LaBr ₃ (Ce) detector (not used in this work), E) EJ-309 organic liquid scintillators, and F) the inelastic scattering target.	9
2.4	Tail-to-total ratio versus total integral for a single EJ-309 detector measured using an encapsulated ²⁵² Cf spontaneous fission source. The short integral was 25 ns and the long integral was 500 ns.	15
2.5	Experimental setup to optimize the “TF_INT_DIFF” parameter on the Mesytec MDPP16 board configured with the SCP firmware. 511 keV γ coincidences were built between antipodal leaves on the two CLOVERs: (0.1,1.4), (0.2,1.3), (0.3,1.2), (0.4,1.0).	15
2.6	TDC differences between two 511 keV γ rays from ²² Na for two CLOVER leaves, Clover 0 Leaf 1 and Clover 1 Leaf 4. The red curve is a Gaussian fit to the coincidence peak, with a mean of -2.94 ± 0.45 TDC units, and a standard deviation of 66.66 ± 0.34 TDC units.	16
2.7	The average time resolution of a single CLOVER leaf as a function of the “TF_INT_Diff” parameter, calculated using coincident 511 keV γ rays from ²² Na.	17
2.8	The trigger probability for a single CLOVER leaf as a function of γ energy measured using a ¹⁵² Eu point source. The red line is a fit to 2.8 ($\chi^2/\text{NDF} = 2.05/12$), with $A_0 = 1.045$, $E_0 = 45.82$, $C_0 = 3.843 \times 10^6$ and $C_1 = 97.63$	18

3.1	A timing diagram for the GENESIS TOF technique. The real times, t_0 , t_R , $t_{\gamma'}$, and $t_{n'}$ represent the arrival of the charged particle beam bunch on the neutron production target, the arrival of neutrons at the target in the GENESIS array, the arrival of an inelastic γ ray at an HPGe detector, and the arrival of an outgoing neutron on a scintillator, respectively. The signal processing delays, Δ_{RF} , Δ_{γ}^j , and Δ_n^i , indexed by detector, give rise to measured times T_{RF} , $T_{\gamma'}$, and $T_{n'}$, respectively.	20
3.2	^{252}Cf prompt γ -ray time differences in ns between all γ -ray events in EJ-309 Detector 0 and γ rays between 710 and 1910 keV in Clover 0, Leaf 0. A Gaussian distribution of true coincidences, with a mean of -21.2 ± 0.1 ns and standard deviation of 3.3 ± 0.1 ns, was fitted ($\chi^2/\text{ndf} = 0.749$) which allows for the determination of $\delta_{\gamma}^{0,0}$ and σ_T	21
3.3	Gamma-flash from the deuteron pulse interacting in the carbon break-up target following Compton scattering in the ^{56}Fe target as seen by organic scintillator Detector 4. Data taken with no target present in the array was used as a background subtraction. A fit to a Gaussian is also shown. The mean of the peak after correcting for the flight time of the γ -ray from the break-up target to the scattering target and the scattering target to the detector gives Δ_{RF} . The FWHM is approximately 9.1 ns.	22
3.4	A 2D plot of the ^{252}Cf neutron TOF versus light yield for a single EJ-309 detector (Detector 8). The TOF was calculated using a γ in any other EJ-309 detector as a start time. The region labeled I indicates the range of TOFs from which the quasi-monoenergetic response function were selected. The regions labeled II were used to for background subtractions for the response functions.	25
3.5	Result of the simultaneous fit of scintillator gain and light yield resolution shown for a single experimentally measured quasi-monoenergetic neutron response function for a single EJ-309 neutron detector. Each response function was integral-normalized. For the simultaneous fit across the four response functions, $\chi^2/\text{ndf} = 1.36$	26
3.6	A view of the GEANT4 model of GENESIS. For clarity, a few of the supporting aluminum bars have been excluded from the image, but they are present when calculations are performed. Suspended in the center of the array is the model of the ^{56}Fe target.	27
3.7	Background subtracted gamma-ray spectrum from Clover 0 Leaf 1 taken with the neutron-activated ^{56}Fe target hanging in the center of the GENESIS array. The starred peaks are from the decay of ^{56}Mn : 846.8 keV, 1810.7 keV, 2113.1 keV, 2523.1 keV, 2657.6 keV.	28

3.8	Gamma efficiency for Leaf 3 on Clover 0 (at 90°) measured using a $0.916 \mu\text{Ci}$ ^{152}Eu point source located at the center of the GENESIS array. Also shown is the efficiency measured using a neutron-activated ^{56}Fe source, mounted in the center of the array. The decay of ^{56}Mn , produced via $^{56}\text{Fe}(n,p)$, emits γ rays with energies from 846.7 to 2657.6 keV. The curve is a fit to the Debertin efficiency function [62], the width represents the uncertainty in the fit.	30
3.9	The CLOVER GEANT4 model without the aluminum can containing the crystals.	31
3.10	Schematic representation of the dead layers in a CLOVER leaf. The dead layer at the front of the crystal is of order $t_{dl} \sim 20 \mu\text{m}$, the length of the dead layer surrounding the coaxial hole is $h_{dl} \sim 12 \text{ mm}$, the radius of the dead layer surrounding the coaxial hole is $r_{dl} \sim 5 \text{ mm}$	31
3.11	Setup for the CLOVER scanning. A ^{137}Cs source was attached to the back of 10 cm long copper collimator with a 1 mm diameter hole. The collimator was mounted to a 2D translation stage. The stage was positioned 36.64 cm from the front face of the crystals.	32
3.12	Count rate in the 661.657 keV ^{137}Cs peak as a function of the collimator+source position for all leaves. The scan was done across Leaf 2.	33
3.13	Experimental and simulated 661.657 keV count rate as a function of collimator+source location.	34
3.14	Comparison of simulated (red and black lines) and experimentally measured (data points) γ -ray detection efficiency for a Leaf 3 of Clover 1 in the GENESIS array. The simulations were run with source geometries equivalent to the ^{152}Eu point-source and extended ^{56}Fe source.	35
3.15	Add-back factor for the two CLOVER detectors measured using a ^{152}Eu source. There is no loss in efficiency at low energy and a gain of up to 45% at 1408 keV. The cross are calculations of the add-back factor using the GEANT4 model described in the text. The experiment agrees with the calculation to within 1% for Clover 0 and within 4.5% for Clover 1.	36
3.16	^{252}Cf PFNS from the evaluation of Mannhart. The errors represent the uncertainty on the spectrum from the reported fit parameter uncertainties and covariance.	37
3.17	GEANT4 model of the EJ-309 organic liquid scintillator detector used in GENESIS (right hand side) and the ^{252}Cf container (left hand side).	37
3.18	$\gamma\gamma$ time differences from ^{252}Cf for a single EJ-309 detector (Detector 4) and every other scintillator in the GENESIS array. The dashed (red) curve is a Gaussian distribution plus linear background fit to the data. The linear background was fitted on data from -100 to -30 ns and 30 to 100 ns. The tailing on either side of the peak is due to coincidences with non-prompt fission γ -rays.	38

3.19	Measured and modeled neutron spectrum in a single EJ-309 detector in ratio to the ^{252}Cf PFNS from Mannhart [53]. The width of the simulated curve reflects the statistical uncertainty of the calculation. Neutron energy was calculated from TOF using the rest of EJ-309 detectors in the array as γ detectors. The presence of a small fraction of non-prompt gamma rays gives rise to an increase in the observed-to-modeled ratio at high neutron energy. [66]	39
3.20	Total neutron detection efficiency as a function of neutron energy for 16 EJ-309 detectors (representing 61.6% of the total neutron detector solid angle) calculated using GEANT4. The y -error bars are a quadrature sum of the statistical uncertainty and the systematic uncertainty arising from the scintillator light yield gain and resolution calibration parameters.	40
4.1	Total $^{56}\text{Fe}(\text{n,tot})$ cross section calculated with TALYS1.96. The contributions from the different reaction components are also shown.	42
4.2	Parameters for the contributions of the various potential wells in the Koning-Delaroche neutron optical model potential for ^{56}Fe	43
4.3	χ^2 between experimental and calculated Total-time-since-last-RF versus detector light yield for different values of the TALYS keyword <code>avadjust n</code> . The χ^2 is summed over detectors 8, 7, 6, and detector between $60^\circ - 120^\circ$	49
4.4	χ^2 between experimental and calculated Time-since-last-RF versus gamma yield for different values of the TALYS keyword <code>s2adjust 26 56</code> . The χ^2 is given in Eq. 8.7.	51
5.1	Level total spin J versus level excitation energy E_{ex} for ^{56}Fe based on RIPL3 [80]. The observed γ -transitions that do not suffer from neutron frame overlap are indicated by a blue dot-long-dashed line. The observed transitions that suffer partially from frame overlap (i.e. those that contain some regions of Time-since-last-RF that can be uniquely attributed to a single neutron energy) are indicated by a red dashed line. The 846.8 keV $2_0^+ \rightarrow 0_0^+$ is fully wrapped.	55
5.2	PDF of the γ flash seen by the reference EJ-309 Detector 4.	57
5.3	Visual representation of the neutron flux matrix for 14 MeV TTDB on Carbon over a flight path of 7.365 m, plotted as incident neutron energy versus Time-since-last-RF. Each bin is 8.068 ns wide.	57
5.4	The yield of the 846.8 keV γ -ray versus Time-since-last-RF calculated using a cross section from TALYS1.96 and the flux matrix of Fig. 5.3. The black points are the total yield, the contributions from the different beam pulses are shown in color. The dominant contribution across most of the Time-since-last-RF domain is from the second most recent beam pulse.	58

5.5	The yield of the 1037.8 keV γ versus time since last RF, calculated using the cross section from TALYS1.96 and the flux matrix of Fig. 5.3. The total yield is shown in black and the contributions from different beam pulses are shown in color. Across the entire Time-since-last-RF domain, only one beam pulse is constituting the entire yield.	59
5.6	Secondary neutron energy distribution at $0^\circ - 2^\circ$ from a TALYS1.96 calculation convolved with the flux matrix.	60
5.7	Correlation matrix for the parameters of the Debertin fit function from a fit to GEANT4 calculated efficiency for a single CLOVER leaf.	61
5.8	Slices of the neutron response function R showing neutron energy versus light yield at four different initial neutron angles for a single neutron detector (Detector 8, 13°). The scale represents the number of neutrons reaching the detector normalized by the number of source neutrons used in the calculation (2×10^9). The primary efficiency is from neutrons with initial angles in a narrow range around the detector angle.	62
5.9	Flow chart showing the forward modeling analysis. First (Loop 1), the nOMP parameters (Table 4.1) are optimized on the neutron data with the rest of the parameters fixed at default values with keyword <code>best y</code> . The parameters in Table 4.2 are optimized in Loop 2 on the γ -ray data, with nOMP parameters from the neutron optimization. The final χ^2 (Loop 3) is calculated against the neutron and gamma data and the uncertainty on the optimal parameters is found.	64
6.1	Map of the thickness of the ^{56}Fe target determined using an ^{241}Am point source. The x and y axes represent the 0.5 cm grid the target and source were placed on. The average thickness is 0.603 ± 0.042 mm.	68
6.2	The probability for a neutron to undergo more than one reaction within the ^{56}Fe target as a function of the initial neutron energy. The probabilities were calculated using forced collision Monte Carlo.	69
6.3	ADC spectra versus experiment time for a single EJ-309 detector (Detector 22) on the second Mesytex MDPP16 board with the QDC firmware. All the detectors on this board had similar distortions of the ADC spectrum each time the DAQ was stopped and started for a new file.	69
6.4	ADC spectra versus the time since the start of a single file for EJ-309 Detector 7. For every file where a gain offset like the one between 0-1500 seconds above, the offset data was discarded.	70
6.5	Activation foil cross sections with uncertainties from IRDFF-II [88]	71
7.1	Experimental TTOF versus light yield for scintillator 8 at 13.1° relative to the neutron beam.	74
7.2	Experimental TTOF versus light yield for scintillators with angles between 60° and 120°	75
7.3	Calculated TTOF versus light yield for EJ-309 Detector 8 at 13.1°	76

7.4	Calculated TTOF versus light yield for EJ-309 detectors between 60° and 120°.	77
7.5	Experimental and calculated light yield spectra in EJ-309 Detector 8 for two TTOF slices at 60-61 ns and 20-21 ns. The first edge in both spectra is from elastic scattering in the ^{56}Fe target by neutrons from the dominant wrap. The elastic scattering edge from neutrons in the wrap before are visible at ≈ 0.6 MeVee for the slice on right left and ≈ 0.8 MeVee for the slice on the right.	78
7.6	^{56}Fe elastic scattering cross section calculated using TALYS parameters obtained from the forward model minimization against GENESIS neutron singles data. The y-errors are computed from the covariance obtained at the end of the minimization. Also plotted is the cross section from the ENDF/B-VIII.0 library.	80
7.7	$^{56}\text{Fe}(n, n_1\gamma)$ partial inelastic scattering cross section calculated using TALYS parameters obtained from the forward model minimization against GENESIS neutron singles data. The y-errors are computed from the covariance obtained at the end of the minimization. Also plotted is the cross section from the ENDF/B-VIII.0 library.	80
7.8	^{56}Fe elastic scattering relative angular distributions for 3 EJ-309 detectors (6, 7, 8) calculated using TALYS parameters obtained from the forward model minimization against GENESIS neutron singles data. The y-errors are computed from the covariance obtained at the end of the minimization.	81
8.1	Background subtracted Time-since-last-RF relative to the 3 RF signals nearest the event time versus gamma energy for Clover 1 in total detection mode. The 846.8 keV, 1037.8 keV, 1238.3 keVs and 1810.8 keV transitions can be clearly seen.	83
8.2	Gamma spectrum for Clover 1 showing the inelastic scattering gamma transitions	84
8.3	Angular distribution for the 846.8 keV $2_1^+ \rightarrow \text{G.S.}$ transition for Time-since-last-RF between 0 and 12.09 ns. The curve is a fit to Eq 8.4, with $\alpha = 1.432 \times 10^8 \pm 23534.8$, $a_2 = -0.0866 \pm 7 \times 10^{-4}$ and $a_4 = -0.4054 \pm 7 \times 10^{-4}$	85
8.4	Yield of the 846.8 keV gamma-ray versus Time-since-last-RF for CLOVER 1 (49.2°). The red data points are calculated using the flux matrix and the measurement by Negret [9]. The ratio of the experimental yield to the calculated yield is also shown. The upper x-axis shows the energies of the neutrons contributing to the yield in each TOF bin.	86
8.5	Yield ratio for the 846.8 keV and 1238.3 keV γ transitions in ^{56}Fe . Two forward-modeled yields are also plotted based on two TALYS calculations with different values for the keyword <code>s2adjust 26 56</code> . The χ^2 when this keyword set to 1.0 (red curve) was 7.89. When the keyword set to 3.0 (blue curve) the χ^2 was 24.48.	87
8.6	1238.3 keV production at 49.2 degrees	89
8.7	1810.8 keV production at 49.2 degrees	90
8.8	1037.8 keV production at 49.2 degrees	90
8.9	1303.4 keV production at 49.2 degrees	91
8.10	2094.9 keV production at 49.2 degrees	91
8.11	2113.1 keV production at 49.2 degrees	92

8.12	2273.2 keV production at 49.2 degrees	92
8.13	1670.8 keV production at 49.2 degrees	93
8.14	2523.1 keV production at 49.2 degrees	93
8.15	2034.8 keV production at 49.2 degrees	94
8.16	Experimental and calculated 846.8 keV gamma yield versus Time-since-last-RF. The TALYS calculation used the minimum parameters.	95
8.17	Ratio of gamma-ray yields measured at the two GENESIS CLOVER angles. Where available, the GENESIS data is compared to the measurement by Savin [92].	96
8.18	Ratio of gamma-ray yields measured at the two GENESIS CLOVER angles. Where available, the GENESIS data is compared to the measurement by Savin [92].	97
9.1	Signal-to-noise ratio for the neutron detectors with and without a coincident 846.8 keV gamma-ray detection in any of the CLOVER leaves.	99
9.2	Neutron/846.8 keV gamma coincidence yield for EJ-309 detector 8 and both CLOVER detectors as a function of Time-since-last-RF. The red line is the yield in coincidence with portions of the gamma-ray spectrum to the left and right of the 846.8 keV peak and represents the random-coincidence background rate. . .	100
9.3	Outgoing neutron energy spectrum for neutrons in coincidence with the $E_\gamma =$ 846.8 keV transition in ^{56}Fe for EJ-309 Detector 8.	100
9.4	Outgoing neutron energy spectrum for neutrons in coincidence with the $E_\gamma =$ 1238.3 keV transition in ^{56}Fe for EJ-309 Detector 8.	101
9.5	Time since last RF versus light yield for neutrons in EJ-309 Detector 8 in coin- cidence with an 846.8 keV gamma detected by either CLOVER.	102
10.1	Correlation matrix for the simultaneous forward model	105

List of Tables

3.1	GENESIS HPGe energy resolution.	24
4.1	TALYS keywords used for secondary neutron energy/angle forward modeling . .	48
4.2	TALYS keywords for gamma ray production forward modeling	50
5.1	HPGe detector efficiencies, parameterized using the Debertin fit function.	60
5.2	TALYS outputs used by default	63
6.1	Total deuteron beam charge and average beam current for the three different target configurations.	66
6.2	Experimental parameters and results of the activation foil neutron flux normalization.	72
7.1	Optimal values for TALYS keywords when compared against GENESIS secondary neutron energy/angle data.	79
8.1	Optimal values for TALYS keywords when compared against GENESIS gamma ray production data.	89
9.1	Potential grouping of all neutron detectors into angles for $n\gamma$ coincidence measurements	101
10.1	Summary of uncertainties or corrections in the measurement of gamma-ray production and secondary neutron energy/angle distributions, based on [17].	106
A.1	Scintillator detector locations relative to the center of the GENESIS frame. The EJ-309 detectors are not pointed at the GENESIS target, so the normal vector of the front face of the detector is given. The neutron beam travels in the $-\hat{x}$ direction.	115

Acknowledgments

I remember leaving Nuclear Engineering 101 lecture one day in the Fall semester of 2016 with a sense that I had just experienced a kind of moment that I have seldom felt and that some people never feel. I cannot recall what the lecture was about, but what became clear was how incredible the nucleus was. That there is this system, so important to the foundations of modern physics and society, yet still not fully understood and still posing new mysteries for scientists nearly a century after the discovery of fission, was not something I had anticipated encountering when I was going around telling people I was studying nuclear engineering because of things like ITER. Calling it sublime may be inappropriate but I certainly felt that in that moment something had reached down and showed me a path that, while long and arduous, would lead to a place where my curiosity, both scientific and not, would feel no barriers. The path continues to wind, the forest is still thick, but my step is sure, my pace is steady, and my eyes and ears have learned to see and hear the patterns in nature from which the truth can be learned.

This work would not be possible without the many people who have helped me in all domains of life. First, I'd like to thank Dr. Lee Bernstein for that lecture seven years ago, for the opportunity to be part of the teaching team for NE101 in the Spring of 2023, and for the opportunity to work on the GENESIS project. The version of myself who walked out of lecture that day in 2016 would be in disbelief if he knew that his PhD in experimental nuclear physics and nuclear data would be carried out under the tutelage of Dr. Bernstein. The path behind and ahead of me would not exist without Dr. Bernstein's knowledge, creativity, passion, and support.

My research career started as an undergraduate student with the URAP program working with Dr. Bethany Goldblum's Bay Area Neutron Group (BANG). I am deeply thankful for her continued support and insight over the years. It was clear after the first time I presented a graph, and I failed to introduce the axes whose labels were much too small, there were error bars and features that I could not explain because I had not been careful, that nobody understood what the figure was supposed to say because I had not given any context, that working with Dr. Goldblum meant doing high quality work. The precision and quality she demanded in presenting my work reflected her desire for precision and quality in my thought while doing the work, a skill that was not easy to learn but one I am grateful for having been taught.

The moment I became enamored with experimental work occurred during my first 88-Inch Cyclotron experiment, measuring the $^{40}\text{Ar}(d,p)$ cross section with Dr. Darren Bleuel. As usual, we did not get beam until the dead of night, but when we placed the gas cell in the Room 131 detector and started counting, Dr. Bleuel casually pointed out the small 1293.64 keV peak and said "there it is, Argon-41". It was a simple moment, late at night, and a tad cliché, but I couldn't believe we had transmuted a material, and I was hooked. Since then, and after many conversations in the cubicles, over Zoom, or over a beer, Dr. Bleuel has taught me how to live and breathe experimental science, how to enjoy when

something works and the planned-for signal is in the data, but also how to plan for and anticipate failure.

When I started attending the weekly BANG meetings, there was a PhD student preparing for his qualifying exam. Dr. Goldblum turned to one of the new faces in the crowd and asked me if I understood what he had just said about his scintillator calibration gain and light yield calibration procedure, including the definition of the light yield units, MeVee, that were used. I did not. I had not yet taken a class on radiation detectors and I had only been mostly paying attention because I was already so lost. Hopefully Dr. Josh Brown did not mind too much reexplaining and revising his slides after that, and hopefully he has not minded the thousand other questions and discussions we have had the past four and half years. The execution of this dissertation research would have been much more difficult without Dr. Brown's deep knowledge and help in the Cave, in the counting area, in front of my monitor, and on the software repository. The many hours spent with Dr. Brown and Dr. Thibault Laplace putting together pieces of 80/20, solving issues with the data acquisition, taking calibration data, writing analysis code while the cyclotron operators tuned the beam, keeping the detectors cold, and planning and developing an analysis chain were at times long but always interesting, thoughtful, and deeply meaningful.

Life as a graduate student was not easy, but it could have been worse if not for the company of my friends and peers in the classrooms, the cubicles, or somewhere out in Berkeley. I would like to especially thank Mallory. It would have been very difficult to reach this point if I did not have her care, support, and company during my most stressful hours and sleepless nights. I would also like to thank Nick and Hannah for their continued friendship since that first summer internship at NIF and all the ups, downs, twists, and turns that life has taken since then.

Finally, I would like to thank my family. It has been a long and at times bumpy road since we said good bye in the courtyard of the Unit 2 dorms in August of 2014 but their love and support has been the constant and solid ground upon which I have been able to reach for and accomplish everything in my life. All of my best and favorite parts of myself I see also in my mom, dad, or sister, and I am eternally grateful for all the tangible and intangible lessons they have taught me.

Chapter 1

Introduction

1.1 Motivation

The next generation of nuclear technologies tend to deal with fast neutrons, both in reality and in simulation space. The need for these models in the design and optimization of the development stage of these technologies is multiple and varied. The models are needed to demonstrate that the proposed concept can work and to begin scoping out the problem space that would need to be addressed via further research in basic science or with engineering. As the solutions to those initial problems are found, the models continue to play a role in further elucidating the engineering and science challenges that can take the technology out of the model space and into the real world. The models themselves continue to change as new data becomes available, either as inputs or as benchmarks against which the models can be tested. Considerations like safety and economy necessitate investigation into construction or operational tolerances based on the uncertainties of the model and its underlying data. These technologies are complex and the models are therefore multi-physics, but a critical component is still the neutronics — the where, when, and how the neutrons move and interact with the environment. As a result, the nuclear data remains an important input, and the better the data are known, in terms of the accuracy of the data and in some cases the existence of data at all, the better these technologies can perform. Ultimately, the model calculations serve as a predictor of full system performance in lieu of a prototype. The results of those calculations can be used to move the technology from model space to the real world if and only if the model itself has been sufficiently verified in its description of the physics it purports to model and validated against benchmarked data sets. The lack of benchmark data sets in many applications means that significant attention must be given to the analysis of the uncertainties associated with the input data.

The Experimental Breeder Reactor II (EBR-II) was a sodium cooled fast reactor located at Idaho National Laboratory that operated from 1964 to 1994. EBR-II remains one of the only actually constructed and operated fast reactors against which modern fast reactor designers can benchmark their model calculations of important reactor parameters, like the

eigenvalue. Despite the paucity of data, a model of the EBR-II validated against that data can serve as a tool to investigate the effect of other model-input uncertainties, including the nuclear data. A study by Bostelmann *et al.* used this model to investigate the impact of nuclear data and associated uncertainties on the predicted k_{eff} and control rod worth uncertainties [1]. Two evaluated nuclear data libraries, ENDF/B-VII.1 [2] and ENDF/B-VIII.0 [3], were tested. The uncertainty on k_{eff} changed by -53% (i.e. ENDF/B-VIII.0 reduced the uncertainty) and the control rod worth changed by 6.8% . A more comprehensive study by Bostelmann *et al.* looked at the nuclear data needs for multiple advanced reactor designs via studies of the sensitivity of key reactor parameters to changes in the relevant data (e.g. (n, γ) cross sections and associated uncertainties, average fission neutron multiplicities, thermal scattering laws, etc.) between evaluated nuclear data libraries and via perturbations about central values from the uncertainties contained within evaluated data libraries [4]. The results bring to light a key difference between the advanced thermal and fast reactors: the importance of inelastic scattering on structural and fuel elements plays little to no role when the vast majority of the neutron population is at energies below the first excited state of the constituent nuclei. Improving inelastic scattering data, both total cross section and the uncertainties associated with secondary particle angular distributions, is highlighted as key need for all three fast reactor designs studied.

Neutron active interrogation is a powerful tool for examining objects of interest and determining, among other things, the presence of special nuclear material or other illicit substances. These platforms generally use a pulsed deuterium-tritium (DT) neutron generator, or a continuous DT source with some kind of associated-particle imaging (API) capability, aimed at an object of interest [5]. A variety of detectors are used to observe secondary neutrons and/or gammas created from individual DT neutron pulses or API tagged neutrons. Discrete gamma transitions from the de-excitation cascade following inelastic scattering can be used to identify specific isotopes if high-resolution gamma-ray detectors are used. Neutron detectors can be used to identify and excess of neutrons, indicating the presence of fissile (neutron-multiplying) material, and the existence of neutron spectroscopic or imaging capabilities can provide even more information on the nature of the secondary neutrons and the distribution of the source in space [6]. Looking at long times relative to a burst of neutrons can reveal the presence of β -delayed neutron emission or fission product decay. A primary challenge with these platforms, especially when trying to identify spoofed special nuclear material, is the complex environment that the incident and secondary particles travel through, necessitating the development of neutron transport models and forward modeling analysis algorithms. A study by McChonchie *et al.* [7] looked at the nuclear data needs for active interrogation platforms relying on secondary gamma emission for two kinds of users, those who are interested in average spectra collected over multiple neutron pulses or a certain time of continuous neutron irradiation and those who are interested in event-by-event coincidences. For the first group, the report highlighted the discrepancies between various evaluated nuclear data libraries, especially the existence of certain discrete or capture γ information in ENSDF and the corresponding lack of reaction cross section data in ENDF/B-VIII.0. For the second group, besides the issue shared with the first group over the

lack of information available in the evaluated libraries, the report found that the ability to model correctly the correlated behavior was not feasible with current modeling codes. The development of new modeling capabilities would require the benchmarking of those codes against a set of benchmarks that may or may not contain sufficiently detailed information.

1.2 Past Measurements

In all of these applications, elastic scattering, inelastic scattering, and γ production on structural materials like steel — or the primary component of steel, iron — is an important nuclear data quantity to understand. Iron has long been a structural component, including in the existing fleet of reactors in the United States, and as such there exists a wealth of experimental data. Nevertheless, there are still areas where the data can be improved. Recently, the international CIELO collaboration sought to generate the most high quality evaluation of neutron reactions on the iron isotopes, specifically focusing on improving inelastic scattering cross sections and angular distributions for elastic and inelastic scattering [8]. Despite their efforts and some choices made during the evaluation about what data to favor, some issues still remain. Four of the primary datasets used in the evaluation were never published in peer-reviewed journals. There is still a lack of clarity from the available experimental data about the elastic angular distributions below 4 MeV and the competition between elastic and inelastic in the range of 4 to 8 MeV. The following two sections will review some of the peer-reviewed data used in the evaluation, with a goal to highlight the experimental techniques and sources of systematic uncertainty.

Gamma-ray Only Measurements

One of the major data sets used in the CIELO evaluation was the high resolution γ -spectroscopy based measurement published by Negret *et al.* in 2014 [9]. The experimental and analysis procedures used in this work are similar to those found in [10, 11, 12]. The measurement was performed at the GELINA facility, with a broad energy neutron beam from 0.1 to 18 MeV monitored by a ^{235}U fission chamber, at an experimental end station 200 m from the neutron source. An unknown number of 1 mm thick natural iron foils were used as a target, surrounded by 8 single crystal, high purity germanium (HPGe) detectors at either 110° or 150° relative to the neutron beam. The detectors were placed at those angles to properly integrate the angle-differential data into total cross sections. The efficiency of the detectors was measured using a ^{152}Eu point source, with an correction for the target geometry calculated using MCNP.

Negret *et al.* report production cross sections for 20 transitions, from the yrast $2 \rightarrow 0$ transition up to transitions from the first 3^- excited state at 4509.6 keV. For certain neutron energy ranges (threshold up to 4.5 MeV), gamma production cross sections were used to calculate total inelastic (ENDF MT=4) and partial inelastic scattering to discrete states (MT=51-90) based on known branching ratios for the γ transitions observed. The

partial inelastic scattering cross sections are the nuclear data products that directly affect the neutron transport calculations. This analysis technique, in addition to its strict validity for nuclei with well known level schemes and for neutron energy ranges below the threshold for continuum excitation, results in larger uncertainties than experiments that observe level population directly.

The angular distribution of the yrast $2 \rightarrow 0$ transition ($E_\gamma = 846.8$ keV) was measured at high angular and energy resolution from threshold to the opening of the second excited state at 2085.1 keV [13]. The data were fit to a linear combination of zero-th, second, and fourth degree Legendre polynomials. Significant P_4 terms were required to achieve agreement, indicating that the common technique of integrating the 55° angle-differential production does not yield the full, angle-integrated cross section.

Neutron Only Measurements

The elastic scattering and partial inelastic scattering cross sections can be measured directly by observing scattered neutrons scattered. In general, these experiments used a combination of neutron time-of-flight (TOF) and light yield information in a scintillator(s) placed a fixed distance from an in-beam sample. Ramirez *et al.* used a monoenergetic neutron source, an enriched ^{56}Fe target, a single deuterated organic liquid scintillator detector placed on a 4 m goniometer to measure the cross sections and angular distributions for elastic scattering and inelastic scattering to the first three excited states via TOF [14]. Pirovano *et al.* used a broad spectrum neutron with a natural iron sample and an array of deuterated and non-deuterated scintillators. They measured the same angular distributions and cross sections as a function of incident neutron energy via a combination of TOF and spectrum unfolding, possible due to the anisotropy of (n, d) elastic scattering [15]. In both studies, the extraction of partial inelastic scattering cross sections to higher excited states was infeasible due to the resolution of the detectors being on the order of the separation of the levels. Smith reported partial inelastic cross sections to the first three excited states and two collections of states around 3.0 MeV and 3.450 MeV for an organic scintillator located 16 m from the a natural iron sample with a quasi-monoenergetic neutron beam [16]. The contributions from individual levels in these groups could not be resolved due to the detector resolution.

1.3 GENESIS: A New Experimental Platform

One commonality with the past measurements is their restriction to a single observational modality, either looking at γ production to deduce cross sections for partial inelastic scattering to discrete states, or looking at neutron distributions, both elastic and partial inelastic. Combining these two different kinds of measurements, including reconciling the associated systematic uncertainties, into a single picture of neutron scattering that can be used to validate nuclear reaction model calculations is the work of evaluation efforts like CIELO. For example, partial inelastic scattering cross sections to higher excited states could be mea-

sured, using detectors of similar resolution to those discussed above, if the neutrons yields could be looked at in coincidence with discrete gamma transitions.

The Gamma Energy Neutron Energy Spectrometer for Inelastic Scattering (GENESIS) is the first attempt at such a platform. By combining high resolution gamma-ray spectroscopy with high resolution neutron spectroscopy at a facility with a broad energy, pulsed neutron beam, GENESIS can simultaneously measure gamma production, inelastic scattering, and elastic scattering cross sections across a range of incident neutron energies. However, this simultaneous measurement is not done without some difficulty, which has necessitated the development of alternative analysis techniques than those discussed above.

This dissertation is organized in three parts. The first part discusses the physical array (Chapter 2), measurements done to characterize and optimize the array (Chapter 3), and the development and validation of a model of the array to aid in the analysis (Chapter 3). The second part provides an overview of the cross sections measured with GENESIS (Chapter 4), and details the methods used to analyze the data and extract cross sections and secondary particles distributions (Chapter 5). The final part (Chapter 6) describes the experimental campaign on ^{56}Fe , the analysis of the data, and the results, including secondary neutron energy/angle distributions (Chapter 7) and gamma-ray production cross sections (Chapter 8) Chapter 10 summarizes the results of the analysis of simultaneous gamma ray and neutron singles data, including a summary of the uncertainties in accordance with [17]. Also discussed is the plausibility of performing neutron/gamma coincidence measurements with GENESIS, which would be a novel and unique window into the inelastic scattering process.

Chapter 2

Experimental Design

This chapter will provide an overview of the GENESIS array starting with a description of the neutron beam facility and the arrangement of the detectors. The basic operating principles of the organic scintillators and HPGe CLOVER detectors will then be given. A description of the data acquisition system and the measured operational characteristics will also be presented.

2.1 Neutron Beam Characteristics

GENESIS is located at the Lawrence Berkeley National Laboratory (LBNL) 88-Inch Cyclotron, a $K = 140$, isochronous cyclotron that delivers pulsed beams of charged particles. Neutrons are created at the facility using thick-target deuteron break-up (TTDB) on low- Z (e.g., Be, C [18]) or higher- Z targets (e.g., Ti, Ta [19, 20, 21]), which results in a broad-spectrum, tunable neutron beam. Neutron production targets are mounted in a Faraday cup to monitor charged-particle flux. Due to the high deuteron beam repetition rate at the 88-Inch Cyclotron, fast neutrons created from a given beam pulse can arrive at experimental stations at the same time as slower neutrons from previous pulses, a phenomenon known as frame overlap [18]. The issue of frame overlap will be discussed in more detail in Sec. 5.1.

The neutron spectrum from TTDB was previously measured at the 88-Inch Cyclotron for 16 MeV deuterons on a Be target using a double time-of-flight (dTOF) technique [18] and activation foil unfolding [20]. Neutron production using TTDB has also been theoretically studied [22, 23] and extensively experimentally measured [24, 25, 26, 27, 28], but discrepancies in measured TTDB spectra, the angular dependence of the TTDB spectrum, and the possibility of other neutron production methods necessitates the use of active neutron beam monitoring in GENESIS experiments, both for spectral shape and fluence. At other facilities (e.g. [9] and [29]), neutron beam monitoring is accomplished using a fission chamber. The neutron beam monitoring at GENESIS is accomplished via activation foils for absolute normalization and a kinematic neutron spectrometer, the Scatter Time-of-Flight or “sToF” detector, adapted from the dTOF technique [18] for neutron energy-differential spectrum.

Briefly, the system utilizes neutron coincidences between an in-beam scintillator, the “target cell”, and one of four out-of-beam detectors, the “scatter cells,” located at a known distances from the target cell and angles relative to the incident neutron beam. The energy of the incident neutron can be inferred using any combination of the incoming or the outgoing TOF and the light yield in the target cell. Figure 2.1 shows the spectrum for 14 MeV TTDB on Carbon measured during the ^{56}Fe experimental campaign. The normalization for this figure is from the GEANT4 [30] calculated detection efficiency, the detector solid angle, and the integrated current over the observation time. The absolute normalization based on activation foils will be given in Sec 6.3. Currently, the only errors included are the statistical uncertainty in the observed data and from the calculated efficiency.

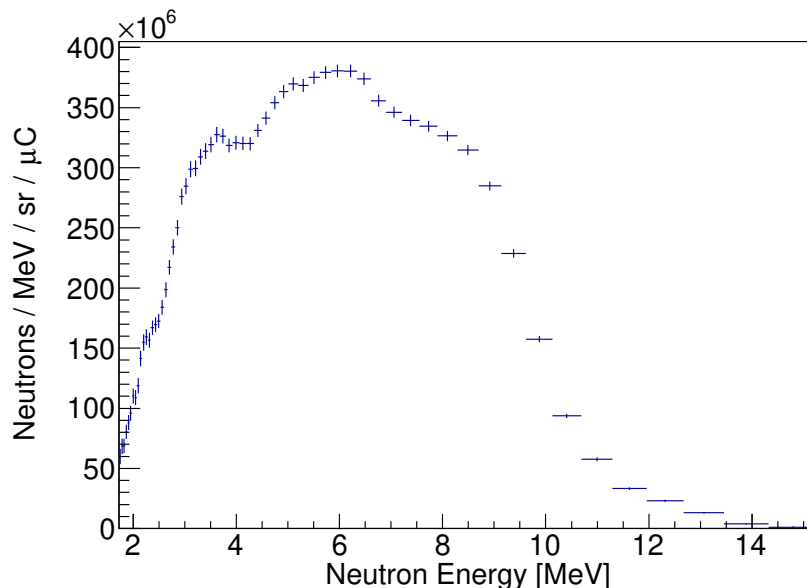


Figure 2.1: Current 14 MeV TTDB on Carbon neutron spectrum for the June '21 GENESIS experiment measured using the sToF detector. The x-errors are the bin widths, which were set to $\sigma/3$ of the incoming TOF resolution. The y-errors represent the statistical uncertainty.

A schematic of the 88-Inch Cyclotron and select experimental endstations is shown in Figure 2.2. GENESIS is housed in the Cave 5 experimental area, which is separated from the cyclotron and neutron production target (located in the “Vault”) by a 2.44 m wall, with 1.52 m of concrete on the experimental area side and 0.91 m of steel on the source side. A 10-cm-diameter iron beam pipe penetrates the shielding wall to allow an open-air neutron beam to enter the experimental area. Current configurations admit neutron flight paths ranging from 6.856 m to 7.856 m. A copper collimator is located between the neutron source and the shielding wall in the vault (see Fig. 2.2) to constrain the beam spot size to scattering-target dimensions and reduce background rates due to neutron interactions with the iron beam pipe and the air. The collimator is cylindrical in geometry, 7.62 cm in radius

and 60 cm in length, divided in six 10-cm segments with borehole radii ranging from 0.33 cm to 0.6 cm, in 0.05 or 0.06 cm increments, with the smallest opening nearest to the neutron source.

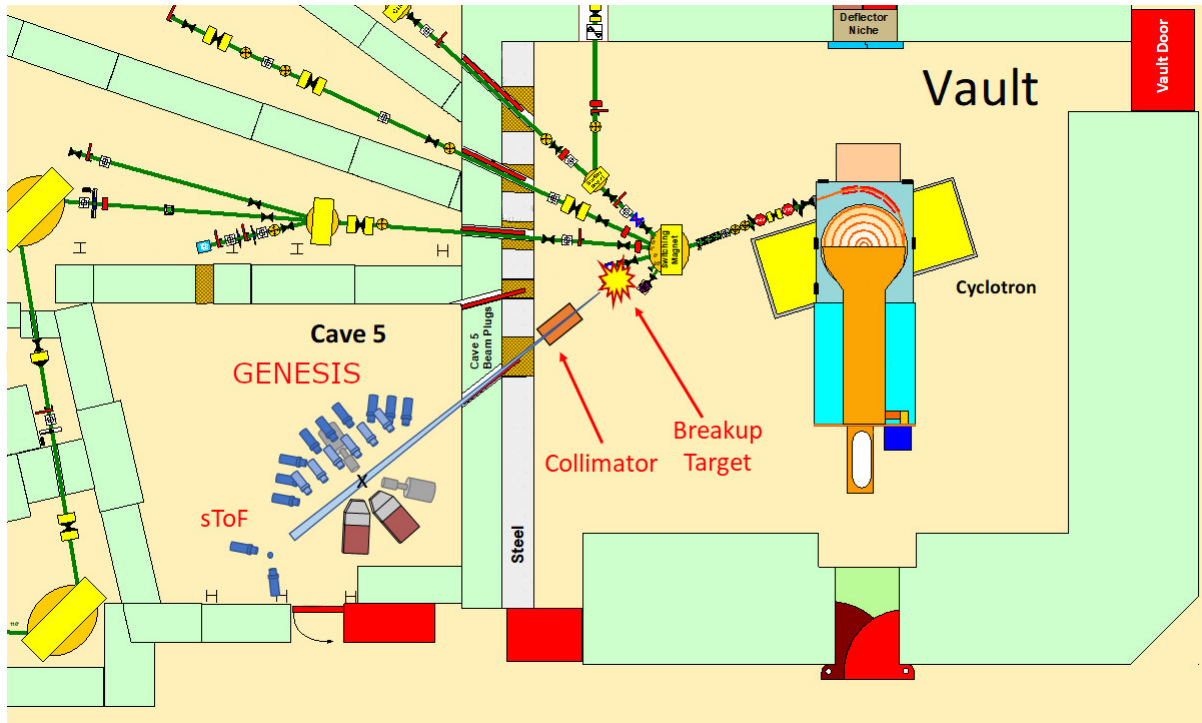


Figure 2.2: Overhead view of a portion of the 88-Inch Cyclotron, deuteron breakup target, and copper collimator which are located in the vault. GENESIS is located in Cave 5 and downstream of the GENESIS array is the sToF neutron beam monitor.

The GENESIS array currently features twenty-six 5.08 cm dia. x 5.08 cm h. right-circular cylindrical PSD-capable EJ-309 organic liquid scintillators [31] for neutron detection coupled to Hamamatsu H1949-51 or H1949-50 PMTs [32]. For γ -ray detection, GENESIS includes two Eurisys 2-fold segmented HPGe N-type CLOVER detectors, each containing four individual HPGe crystals, with Scionix V-0210 bismuth germanate oxide (BGO) anti-Compton shields [33], and two Ortec PopTop HPGe detectors [34]. Activation foils and the sToF spectrometer (see Sec. 2.1) are fielded in conjunction with the GENESIS array for neutron beam flux monitoring. Figure 2.3 shows the elements of the GENESIS array staged in a typical runtime configuration. A single Saint-Gobain type B380, 5.08 cm dia. x 5.08 cm h. right-circular cylindrical $\text{LaBr}_3(\text{Ce})$ crystal [35] mounted to a Hamamatsu R2083 PMT [36] is also pictured (not used in this work, see Sec. 6.2). The positions of the detectors and the distance from the break-up target to the center of the GENESIS array were measured using a Leica Distro S910 mounted to a Leica TRI 70 tripod. The uncertainty on the measured positions is estimated to be 1 mm. The target (labeled F in Fig. 2.3) is positioned at the

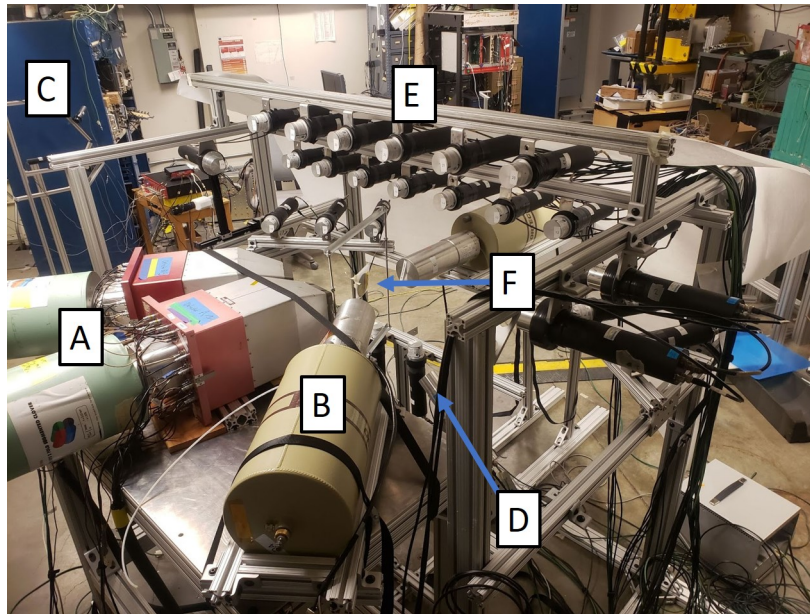


Figure 2.3: A view looking downstream, lower right to upper left, at GENESIS, including A) Eurisy HPGe CLOVER detectors with BGO anti-Compton shields, B) an Ortec PopTop HPGe detector, C) the sToF neutron beam monitor, D) a Saint-Gobain $\text{LaBr}_3(\text{Ce})$ detector (not used in this work), E) EJ-309 organic liquid scintillators, and F) the inelastic scattering target.

height of the beam line, 1.2 m above the floor of Cave 5, a room 2.44 m in height. The detectors are supported by a frame constructed of T-slotted aluminum extrusion.

2.2 Fast neutron detection with organic liquid scintillators

The process by which neutrons or gamma rays are detected with organic scintillators is multi-stage. First, the neutron or gamma must interact with the organic material, creating a recoiling charged particle. The neutrons primarily scatter elastically off the hydrogen, creating recoiling protons, or elastically scatter off carbon. Other scattering reactions on carbon do occur, including inelastic scattering and $^{12}\text{C}(n, n')3\alpha$, but the cross sections for these processes are much lower than the elastic scattering cross section in the typical neutron energy range at GENESIS and they seldom produce recoils that possess sufficient energy to be detected. The energies of the gamma rays typical in GENESIS experiments greatly exceed the binding energy of the electrons, which can therefore be considered free, and the gamma rays primarily undergo Compton-scattering.

The amount of energy lost by the neutron and imparted to the recoiling particle from the

elastic collision can be calculated using non-relativistic 2-body kinematics, assuming that the target hydrogen or carbon is at rest and that any effects to the molecular structure are negligible. Let E be the initial energy of the neutron, E' be the final neutron energy, A be the mass of the target nucleus and θ the angle of the scattered neutron with respect to its initial momentum. The energy lost by the neutron in the non-relativistic limit, ΔE , is

$$\Delta E = E - E' = E \left(1 - \frac{A^2 + 1 + 2A \cos \theta}{(A + 1)^2} \right) = E_{recoil} . \quad (2.1)$$

For neutron-proton (np) scattering, $A = 1$ and the above equation can be simplified to yield the energy of the recoiling proton E_p :

$$E_p = \frac{E}{2}(1 - \cos \theta) . \quad (2.2)$$

Assuming that np scattering is isotropic, the above formula can yield the shape of the 0th-order mono-energetic response function for the detector, which is a uniform distribution in proton recoil energy with an endpoint at the energy of the neutron. For elastically scattered carbon recoils, Eq 2.1 can be simplified to yield the energy of the carbon recoil, E_C :

$$E_C = E(0.14201 - 0.14793 \cos \theta) . \quad (2.3)$$

The maximum carbon recoil energy is a factor of approximately 3.5 less than a proton recoil. The energy of a recoiling electron, E_e from Compton-scattering by a γ with energy E_γ can be derived assuming the electron is initially at rest,

$$E_e = E_\gamma \left(1 - \frac{1}{1 + E_\gamma/m_e c^2(1 - \cos \theta)} \right) , \quad (2.4)$$

where θ is the scattering angle of the gamma-ray. The probability for a γ at a certain energy to Compton-scatter into some angle θ is given by the Klein-Nishina distribution. For the γ energies relevant to GENESIS experiments ($\approx 0.5 - 8$ MeV), the Klein-Nishina distribution is forward peaked [37].

A portion of the recoil particle kinetic energy is converted into light. The precise mechanisms responsible for the generation of scintillation light is complicated but a brief explanation will be given because the result of these mechanisms, and the resulting differences in the temporal distribution of the light, is what enables the detectors to be used in mixed radiation fields. As the charged particles slow down, the scintillating molecules are excited and de-excite by emitting an optical photon. There are three types of de-excitation: 1) fluorescence, which is the direct de-excitation of states in singlet configurations, 2) phosphorescence, which is the direct de-excitation of states in triplet configurations and 3) delayed fluorescence, which results when triplet states transition into singlet states which then de-excite [37]. The three processes occur on different time scales, with fluorescence occurring the fastest ($\sim 10^{-9}$ s) and phosphorescence the slowest ($\sim 10^{-4}$ s) [38]. The relative number of scintillation photons

generated from each process depends in part on the linear energy transfer (LET) of the recoiling charged particle. Thus, the recoiling particle can be identified by associating pulse shapes with proportionally more of the slower light components with recoiling particles that have higher LET. The number of photons created by the recoiling particle, the light yield, is a property of the scintillator material and is proportional to the energy of the particle and the type, with higher- Z particles generating less light due to quenching mechanisms. Additionally, the number of photons is Poisson distributed, leading to an intrinsic resolution of the detector [37].

The scintillation light is converted into an electric signal that can be processed by the data acquisition system through the use of a photomultiplier tube (PMT). The PMT contains a photocathode that converts the optical scintillation photons into photoelectrons, a multiplication stage that amplifies the photo-electron signal, and an anode that converts the multiplied photo-electron bunch into a voltage that is propagated down a cable.

The EJ-309 cells are arranged in a quarter-shell centered on the GENESIS target location, spanning roughly $11-165^\circ$ with respect to the neutron beam direction, and at radial distances of 35 – 85 cm, with an average standoff of 60 cm. The locations of all 26 scintillators for the ^{56}Fe experiment are given in Appendix A. To reduce inter-element neutron scattering, the scintillators were placed at least 20 cm from their nearest neighbor. The amount of inter-element scattering was quantified via a simulation study using GEANT4 [30]. The calculation included the aluminum GENESIS frame, all 26 scintillators and an isotropic point source at the center of the array emitting neutrons with energies uniformly distributed from 0.5 to 20 MeV. The energy deposited by protons or carbon ions in each cell was tallied and converted into light output using a fitted EJ-309 proton light yield curve (for more details see 3.2). An event was defined as a > 0.2 MeVee (MeV electron equivalent) deposition in a scintillator. “Bad” events were defined as a single source neutron resulting in an event in ≥ 2 scintillators. The inter-element scattering fraction is

$$F_{i.e.s} = \frac{\text{Bad Events}}{\text{Total Events}} \quad (2.5)$$

The calculated average $F_{i.e.s.}$ for all 26 scintillators was $0.202 \pm 0.194\%$.

The EJ-309 scintillating volume is contained within a 1-mm-thick aluminum cylinder and capped with a 3-cm-radius, 1-mm-thick quartz window. The quartz window is coupled to a PMT via a thin layer of EJ-550 silicone optical grease [39]. The PMTs are housed in a 1-mm-thick permalloy magnetic shield, 23.5 cm long and 3.0 cm in radius. The EJ-309 detectors are mounted on the GENESIS frame with an L-bracket attached just behind scintillator-PMT interface, providing an unobstructed line-of-sight from the target to the active detector volume. For simplicity in construction and modeling of the GENESIS array, the scintillator detectors are mounted perpendicular to the 80/20 aluminum bars. Bias voltages are supplied through a 16-channel CAEN R8033DN [40] and two 8-channel CAEN R1470ETD [41] power supplies, which are controlled and monitored remotely.

2.3 Gamma-ray detection with HPGe CLOVER detectors

The gamma rays created in GENESIS experiments (0.1-10 MeV [42]) interact with matter via three mechanisms: photoelectric absorption, Compton scattering, and pair production [37]. Photoelectric absorption dominates at low γ -ray energies and pair production dominates at high energies. Photoelectric absorption is the process by which the full energy of the incident γ is converted into the recoil (kinetic) energy of an electron. Compton scattering is an elastic scattering of the incident γ ray on an electron. The formula for the energy of the recoiling electron is given above (Sec 2.2). Pair production occurs when the incident γ , in the presence of a strong electric field (e.g. the field generated by a high-Z nucleus), creates an electron/positron pair. The kinetic energies of the electron and positron do not sum to the full energy of the incident γ because of the energy required to create the pair of particles must come from the energy of the incident photon. The positron can subsequently annihilate after some amount of slowing down; the two resultant 511 keV γ 's can then undergo further interactions, like Compton scattering or photoelectric absorption. The idealized response function of a moderately sized gamma ray detector to a photon with $E_\gamma \geq 1.022$ MeV can be built from these three interactions. There will be a photopeak corresponding to photoelectric absorption and pair-production where both annihilation photons were captured within the detector, a Compton distribution with an edge at the maximum electron recoil (180°), and two more photopeaks at $E_\gamma - 511$ keV and $E_\gamma - 1.022$ MeV corresponding to pair-production interactions where one or both annihilation photon did not interact within the the detector.

The idealized γ ray detector response function derived above can be most nearly realized using semiconducting high purity Germanium detectors (HPGe). The details about the operating principles of HPGe can be found in e.g. [37], but a few important aspects will be highlighted. At liquid nitrogen temperatures, the ionization energy for germanium is 2.96 eV, meaning a 1 MeV incident particle that undergoes photoelectric absorption will generate 3.38×10^5 charge carriers, leading to an intrinsic resolution of 0.13% (assuming a Fano factor of 0.1). This energy resolution is far superior to scintillator detectors and allows for the differentiation of discrete γ -rays from the cascade as a nucleus de-excites from neutron inelastic scattering. To first order, the active volume of the detector can be found by calculating the volume of the region between the p and n contacts. However, the width of these contacts gives rise to dead regions at the surfaces, which reduces the overall efficiency and can introduce incident γ -ray energy and direction dependencies on the efficiency. The signal rise time is both long, due to the slow drift velocities of the charge carriers, and can vary depending on the location within the crystal where the γ -ray interaction occurs. This leads to a poor timing resolution for HPGe.

While the photo-peak resolution of HPGe detectors is limited by the physics of their operation and engineering and design aspects of the crystals, the amount of background present in gathered spectra can be reduced through various methods. One widely used method is the use of an external, high efficiency detector to detect Compton scattering

events within the HPGe crystal [43] and exclude these events from the spectrum. This anti-Compton shield can be implemented by, for example, surrounding the sides of the crystal with bismuth germanate ($(\text{Bi}_4\text{Ge}_3)_{12}$ or BGO) scintillators and, via proper timing synchronization, coincidences between the HPGe and the BGO can be definitively identified as a background event, either a γ that Compton-scattered first in the BGO and then within the HPGe or vice-versa. The rejection of these events leads to a reduction in the magnitude of the Compton continuum associated with the various photo-peaks from whatever γ 's are emitted from a source under investigation. This Compton veto can also reduce the background from natural radioactivity present within the environment.

A second method to improve the signal-to-noise in HPGe data is similar to the anti-Compton veto. Instead of rejecting the Compton-scattered events via a coincidence with a high efficiency but low resolution scintillator like BGO, Compton-scattered γ 's from one HPGe crystal can be photoelectrically absorbed by a second crystal in close proximity to the first. The energies detected in the two crystals in this coincidence event can be summed to recover the full energy of the γ , resulting in a greater photo-peak efficiency than when using the two crystals separately. Various considerations enter into the design and optimization of clustered HPGe detectors, but of interest to GENESIS experiments is that a composite detector with small crystals can be made with a total photo-peak efficiency matching or exceeding larger single-crystal detectors. The size of the crystals has an impact on the timing resolution, with larger crystals having worse timing than smaller crystals, meaning a composite detector can match the efficiency of a large single-crystal detector and outperform that detector applications like GENESIS where timing is important.

For the ^{56}Fe experiment (see Chapter 6 for more details), two HPGe CLOVER detectors were placed in the hemisphere opposite the EJ-309 array on an aluminum table. One CLOVER (Clover 0) was placed roughly perpendicular to the neutron beam (91.5°), at a radial distance of 20.01 cm, measured to the front face of the HPGe crystals. The second CLOVER (Clover 1) was placed at a forward angle of 49.2° relative to the neutron beam and at a radial distance of approximately 26.66 cm. Each HPGe CLOVER is two-fold segmented, and each leaf is 45 mm dia. and 80 mm in length [44]. Signals from each of the four crystals were read out individually and signals from edge-contact anodes, which can provide coarse interaction tracking, were not used. Surrounding each CLOVER was approximately 25 kg of BGO in 16-fold segmentation, with four segments on each side of the CLOVER, housed in a trapezoidal aluminum casing. The signals from the 16 Hamamatsu R3998-2 PMTs [45] mounted to the BGOs were bussed together and read out as one signal, a choice motivated by experimental investigations of the Compton-rejection efficiency. The Peak-to-Compton ratio from the 661.7 keV gamma in ^{137}Cs was used as a quantitative measure of the Compton-rejection efficiency and is defined as the ratio number of counts C in the photopeak to the number of counts in Compton continuum, from 185 keV to 478 keV:

$$PC = \frac{\sum_{658 \text{ keV}}^{668 \text{ keV}} C}{\sum_{185 \text{ keV}}^{478 \text{ keV}} C} \quad (2.6)$$

Three different signal configurations were tested: 1) all 16 signals bussed together, 2) each

signal read out individually, and 3) the four signals nearest each leaf read out as one group. The difference in the three configurations was 3.7%, with configuration 3) performing best. Since little difference was observed, and for simplicity in detector operation and data analysis, configuration 1) was used.

The Ortec PopTops were also located at beam height center, one on the table with the CLOVER HPGe detectors, at approximately 130°, and one in the opposite hemisphere at 90°. Bias voltages for the CLOVERs and PopTops were applied using an iseg NHR-42-60r high voltage power supply module [46].

2.4 Data Acquisition

Three Mesytec MDPP-16 boards were used to acquire list-mode data [47, 48]. Scintillator signals, including the BGO anti-Compton detectors, were processed through two boards configured with the Mesytec QDC [49] firmware to handle pulse integration and timing. For each collected event, a short integral and a long integral of the signal pulse were read out along with a timestamp derived using Constant-fraction discrimination (CFD) [50]. The short and long integrals both start at the beginning of the signal, as determined by the CFD derived timestamp. The short integral is set to a sufficiently short time to cover only the peak of pulse and the long integral is set to a value sufficient to cover the whole pulse. The PSD or shape metric used in GENESIS experiments is the tail-to-total ratio, computed as the difference between the long (total) and short (peak) integrals divided by the long (total) integral.

$$\text{PSD Metric} = \frac{\text{Total Integral} - \text{Peak Integral}}{\text{Total Integral}} \quad (2.7)$$

A typical tail-to-total versus total integral plot for one of the EJ-309 scintillators is shown in Figure 2.4. An event is considered a neutron if its total amplitude is above a detector specific value (99 ADC channels for the data in Figure 2.4) and if its PSD metric is above a certain value (0.174 in Figure 2.4) Events that satisfy the same amplitude threshold and have a PSD metric below that same value are considered gamma rays. The classification of events as arising from a neutron or gamma ray is done during post-processing.

The HPGe signals from the CLOVER and PopTop detectors were processed on a third board with the firmware set to the standard charge preamplifier (SCP) configuration [49], which manages adjustable trapezoidal filtering and timing filtering. This signal processing is handled separately in two different branches. For each collected event, the pulse amplitude and timestamp were read out [49]. The timing resolution of the HPGe signals was adjusted through a single parameter, “TF_INT_DIFF”, on the MDPP-16 SCP firmware [49]. This parameter, and only this parameter, controls the shaping of the signal in the timing branch with smaller values giving rise to smaller amplitude signals. To optimize the timing resolution, a study was performed using a ^{22}Na source to build $\gamma\gamma$ coincidences between the HPGe CLOVER detectors. The detectors were placed on a table facing each other, with roughly 6 cm between the front faces, shown in Figure 2.5. The source was placed in between the

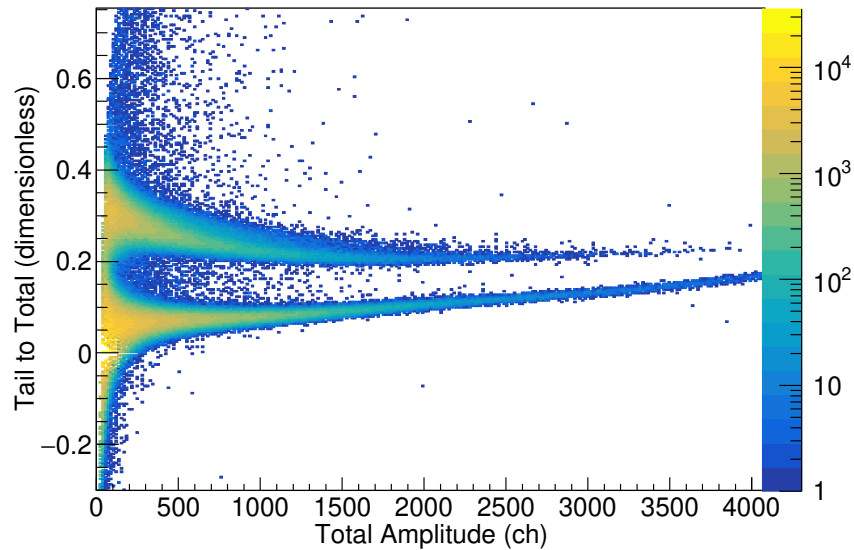


Figure 2.4: Tail-to-total ratio versus total integral for a single EJ-309 detector measured using an encapsulated ^{252}Cf spontaneous fission source. The short integral was 25 ns and the long integral was 500 ns.

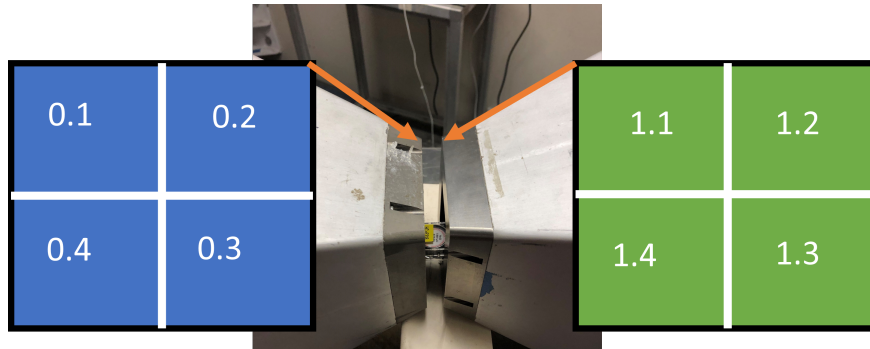


Figure 2.5: Experimental setup to optimize the “TF_INT_DIFF” parameter on the Mesytec MDPP16 board configured with the SCP firmware. 511 keV γ coincidences were built between antipodal leaves on the two CLOVERs: (0.1,1.4), (0.2,1.3), (0.3,1.2), (0.4,1.0).

detectors at height equivalent to the middle of the detectors. Coincidences between 511 keV γ s were built for each pair of opposite leaves on each clover. Figure 2.6 shows a histogram of the TDC differences between coincident 511 keV γ 's in Clover 0, Leaf 1 and Clover 1, Leaf 4 from a data set where the “TF_INT_DIFF” was set to 1, its lowest value. fitted to a Gaussian distribution with a mean of -2.91 ± 0.45 and a standard deviation of 66.66 ± 0.34 in TDC units. This is equivalent to a standard deviation of 6.51 ± 0.3 ns and assuming the timing resolution of the individual leaves are identical, this yields a single leaf time resolution

of 4.60 ± 0.02 ns. Figure 2.7 shows the single leaf standard deviation as a function of the

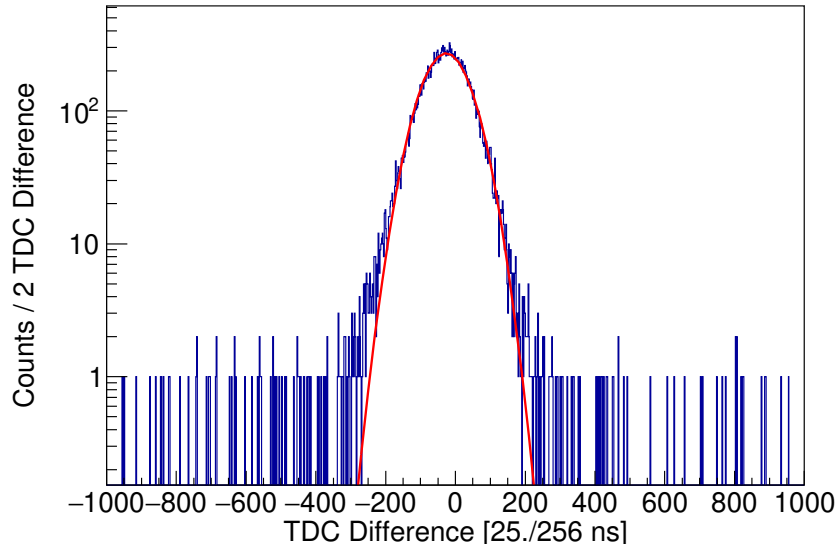


Figure 2.6: TDC differences between two 511 keV γ rays from ^{22}Na for two CLOVER leaves, Clover 0 Leaf 1 and Clover 1 Leaf 4. The red curve is a Gaussian fit to the coincidence peak, with a mean of -2.94 ± 0.45 TDC units, and a standard deviation of 66.66 ± 0.34 TDC units.

“TF_INT_DIFF” parameter, calculated from the four pairs of leaves and assuming that each individual leaf in the pairs has the same timing resolution. The best timing resolution for the HPGe detectors was achieved by setting this parameter to the lowest allowable value.

While this choice yielded the best time resolution, it resulted in the loss of a fraction of events at low charge, due to the inability of the timing branch processing to successfully extract signal time. To characterize the probability of triggering as a function of γ -ray energy, spectra were gathered with a ^{152}Eu source at the center of the frame at multiple values of the timing parameter, ranging from the lowest allowable value (where the charge-dependent trigger probability was observed over the largest energy range) to the highest (where the trigger probability was constant over the considered range). The trigger probability can thus be defined as the count rate corresponding to a γ ray from ^{152}Eu in ratio to the count rate from data taken at the maximum value of the timing parameter. A biexponential envelope for the probability of triggering as a function of incident γ -ray energy was used to quantify this effect:

$$P(E_\gamma) = A_0 e^{-(E_\gamma - E_0)/C_0} (1 - e^{-(E_\gamma - E_0)/C_1}) \quad (2.8)$$

where E_γ represents the γ -ray energy, E_0 represents the γ -ray energy corresponding to a trigger probability of 0%, and the parameters C_0 and C_1 characterize how quickly the probability approaches and stays at unity. For each leaf in each CLOVER and each PopTop

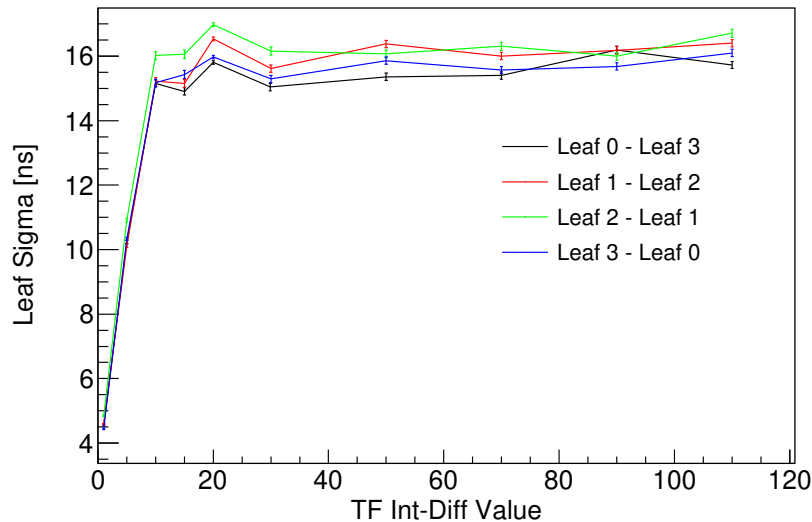


Figure 2.7: The average time resolution of a single CLOVER leaf as a function of the “TF_INT_Diff” parameter, calculated using coincident 511 keV γ rays from ^{22}Na .

HPGe detector, a χ^2 minimization was performed between the measured trigger probability and Eq. 2.8 considering only the statistical uncertainty with A_0 , E_0 , C_0 , C_1 treated as fit parameters. Figure 2.8 shows the trigger probability for a single CLOVER leaf from peak fits to ^{152}Eu point source data and the result of the fit to Eq 2.8.

A constant-fraction-discriminated timing signal from the cyclotron radio-frequency (RF) generator is fed into a trigger channel on each board. This provides time synchronization with the cyclotron to allow for incoming neutron time-of-flight (TOF) determinations. Each channel on all three boards is allowed to generate a trigger signal, which is passed to a Lecroy 429A logic fan-in/fan-out module [51] and propagated back to all three boards to ensure inter-board temporal synchronicity.

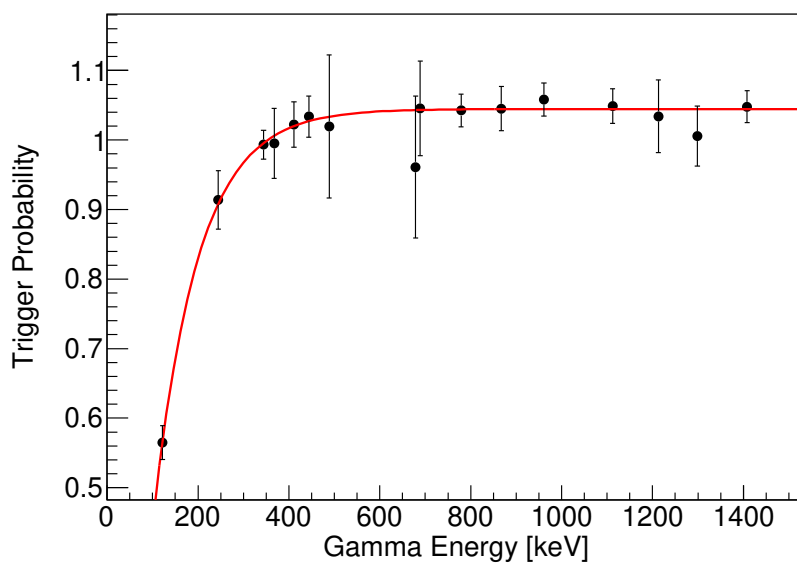


Figure 2.8: The trigger probability for a single CLOVER leaf as a function of γ energy measured using a ^{152}Eu point source. The red line is a fit to 2.8 ($\chi^2/\text{NDF} = 2.05/12$), with $A_0 = 1.045$, $E_0 = 45.82$, $C_0 = 3.843 \times 10^6$ and $C_1 = 97.63$

Chapter 3

Array Characteristics

The previous chapter covered the design of the GENESIS array, the operating principles of the HPGe and organic liquid scintillators, and the data acquisition system. This chapter will present the experimentally determined characteristics of the array necessary to extract reaction cross sections from GENESIS data. The measurements of the array properties were also used to validate a GEANT4 model of the array. The design of the model and the validation will also be presented.

3.1 Event Timing

To determine the neutron TOF (either incoming or outgoing) and reconstruct coincident events from the list mode data, calibration is required to correct for temporal delays in the detection readout, signal propagation, and pulse processing. Figure 3.1 provides a timing diagram for a representative neutron-gamma coincident event, showcasing the principles of the GENESIS TOF technique. The time resolution and signal processing offsets were determined through a combination of experiments using a $0.96 \mu\text{g } ^{252}\text{Cf}$ spontaneous fission source placed in the center of the GENESIS frame and TTDB neutron beam data.

To establish the absolute time delays between individual detectors, a single liquid scintillator detector was chosen as a reference for all other detectors. This gives rise to δ_n^i , which is used to represent the time difference between the i_{th} neutron detector and the chosen reference detector, and δ_γ^j , which is used to represent the time difference between the j_{th} γ -ray detector and the reference detector. To calculate the delays, coincidences between γ -ray events in the reference detector and all other detectors were selected from the ^{252}Cf data, and the raw measured time differences were accumulated into histograms.

The observed TOF T_i for a γ to any scintillator or HPGe detector i at a radial distance D_i from the ^{252}Cf source is

$$T_i = TOF_i + \Delta_\gamma^i = \frac{D_i}{c} + \Delta_\gamma^i. \quad (3.1)$$

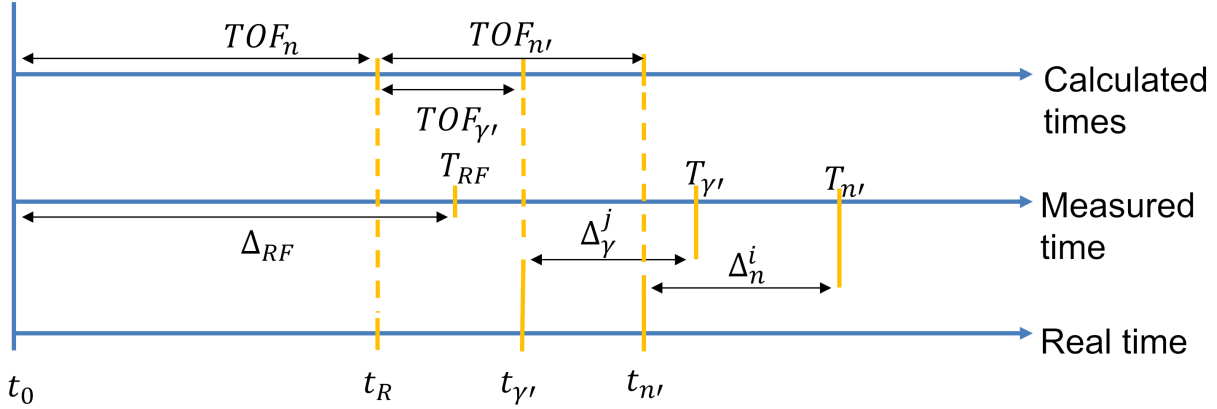


Figure 3.1: A timing diagram for the GENESIS TOF technique. The real times, t_0 , t_R , $t_{\gamma'}$, and $t_{n'}$ represent the arrival of the charged particle beam bunch on the neutron production target, the arrival of neutrons at the target in the GENESIS array, the arrival of an inelastic γ ray at an HPGe detector, and the arrival of an outgoing neutron on a scintillator, respectively. The signal processing delays, Δ_{RF} , Δ_{γ}^j , and Δ_n^i , indexed by detector, give rise to measured times T_{RF} , $T_{\gamma'}$, and $T_{n'}$, respectively.

The time difference between a γ in the reference detector and a γ in any other detector i is

$$\Delta T = T_{ref} - T_i = \frac{D_{ref}}{c} - \frac{D_i}{c} + (\Delta_{ref} - \Delta_{\gamma}^i). \quad (3.2)$$

Eq 3.2 can be solved for $(\Delta_{ref} - \Delta_{\gamma}^i) = \delta_n^i$ or δ_{γ}^i . Figure 3.2 shows an example of such a histogram for time differences between the reference EJ-309 detector (Detector 4, 44.8 cm from the source) and an individual CLOVER leaf (20.4 cm from the source) for events that deposited between 710 and 1910 keV in the CLOVER leaf. The peak represents coincidences between prompt fission γ -rays produced in spontaneous fission. The mean of the peak, after correcting for the total γ flight times to each detector, gives the detector timing offset constant, δ_{γ}^j . The width of the peak represents the quadrature sum of the resolution of the individual detectors, here approximately 350 ps for the EJ-309 detector and approximately 3.3 ns for the CLOVER leaf.

To establish the system timing against the cyclotron, Δ_{RF} must be determined representing the phase offset between the instrument timing and the cyclotron timing. To accomplish this, beam data for the reference detector with the scattering target present in the center of the frame were accumulated, and PSD was used to select γ -ray events. A large portion of the signal is due to scattering of γ 's on air as they travel from the break-up target to the array. Data was also taken with no target present to be used as a background subtraction. For each event, the time difference between a series of RF observations and a signal in the reference detector was calculated. The resulting histogram contained several peaks corresponding to γ rays created when the charge particle beam interacted with the neutron production target

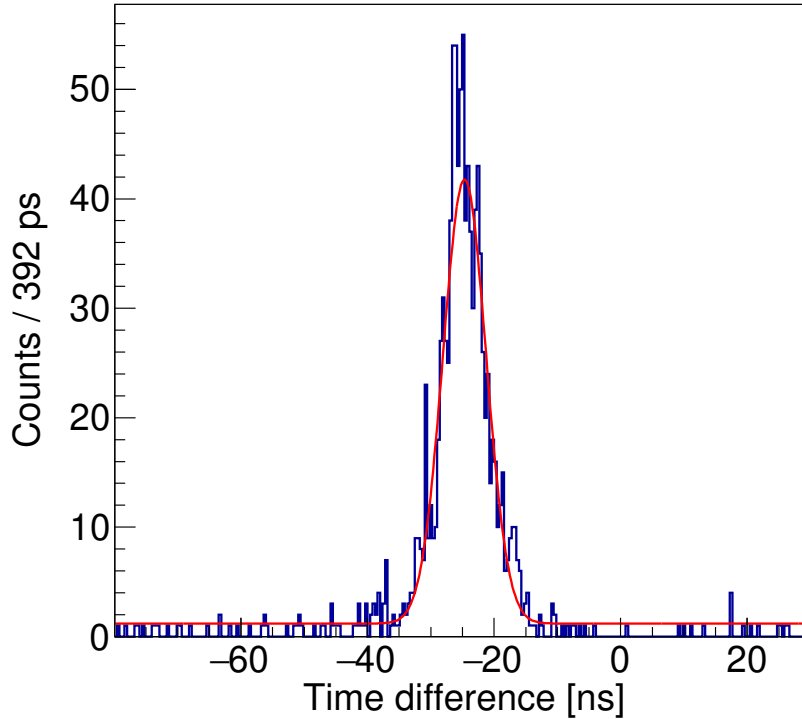


Figure 3.2: ^{252}Cf prompt γ -ray time differences in ns between all γ -ray events in EJ-309 Detector 0 and γ rays between 710 and 1910 keV in Clover 0, Leaf 0. A Gaussian distribution of true coincidences, with a mean of -21.2 ± 0.1 ns and standard deviation of 3.3 ± 0.1 ns, was fitted ($\chi^2/\text{ndf} = 0.749$) which allows for the determination of $\delta_\gamma^{0,0}$ and σ_T .

and then Compton scattered off the target into the reference detector. The Δ_{RF} was then computed using this in conjunction with the known flight-path of the γ rays.

The TOF of the incoming neutron was determined using the detection time, $T_{\gamma'}$, of γ rays produced via inelastic scattering in the target that traveled a distance D_γ^j from the center of the GENESIS array to the j^{th} HPGe detector:

$$TOF_n^j = T_{\gamma'}^j - \frac{D_\gamma^j}{c} - b \times T_{RF} - (\delta_\gamma^j - \Delta_{RF}) \quad (3.3)$$

where c is the speed of light and T_{RF} is the measured time of the RF signal. Due to the frame overlap of beam pulses at the 88-Inch Cyclotron, the reacting neutrons could have come from the b^{th} previous charged-particle bunch [18]. Similarly, the TOF of an outgoing neutron detected in the i^{th} neutron detector and in coincidence with a γ -ray in the j^{th} γ -ray detector is given by:

$$TOF_{n'}^{ij} = T_n^i - T_{\gamma'}^j + \frac{D_\gamma^j}{c} - (\delta_n^i - \delta_\gamma^j), \quad (3.4)$$

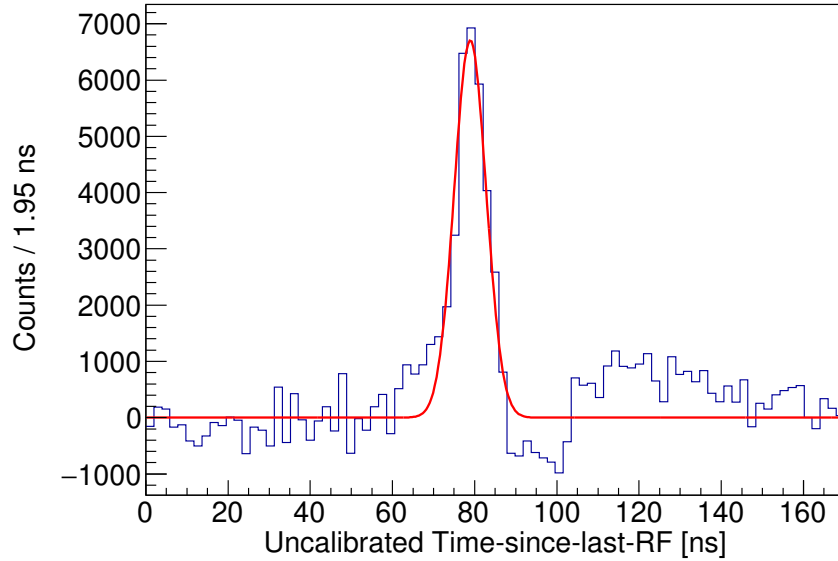


Figure 3.3: Gamma-flash from the deuteron pulse interacting in the carbon break-up target following Compton scattering in the ^{56}Fe target as seen by organic scintillator Detector 4. Data taken with no target present in the array was used as a background subtraction. A fit to a Gaussian is also shown. The mean of the peak after correcting for the flight time of the γ -ray from the break-up target to the scattering target and the scattering target to the detector gives Δ_{RF} . The FWHM is approximately 9.1 ns.

where T_n^i is the measured time of the neutron detected in the i^{th} neutron detector. The detection times T_γ and T_n are uncertain by the intrinsic timing resolution of the detectors, σ_T deduced from the $\gamma\gamma$ coincidence data. The timing offsets δ_γ^j , δ_n^i , and Δ_{RF} are uncertain by the estimates on the centroids of the coincidence peaks, σ_δ .

3.2 Energy Resolution and Gain Calibration

The conversion of raw signal, either the signal amplitude for the HPGe detectors or the pulse integral for the scintillators, into energy, either γ -ray energy or light yield, is the needed for the analysis of γ -ray production or secondary neutron distributions. The precision with which photo-peaks in the HPGe detectors or proton-recoil edges in the scintillator detectors can be associated with specific scattering processes in the GENESIS target is dependent on the energy resolution of the detectors. This section details the measurement of these two detector properties.

HPGe

The energy resolution and gain of the HPGe detectors were measured using a ^{152}Eu source placed in the center of the GENESIS array. The uncalibrated ^{152}Eu spectrum for each leaf was analyzed using a script whose input was a visual estimation of the mean of the 1408.0 keV peak, in units of channel from the analog-to-digital converter (ADC) on the MDPP16-QDC board. That estimate was used to perform a least-squares fit of the peak to a Gaussian plus first degree polynomial background. The mean of that fitted curve, μ_{1408} , was used to estimate the slope m of a linear gain calibration, $m = 1408 \text{ keV}/\mu_{1408}$. The mean of the 121.8 keV peak, $\mu_{121.8}$ was then estimated from the slope and a peak fit was performed in that region. The mean of that fit was used to refine the estimate of the slope and fit the intercept for a linear gain calibration. That estimated calibration was used to estimate the uncalibrated value of the rest of the commonly used ^{152}Eu lines, those with an intensity relative to the 1408.0 keV γ greater than 0.1, and peak fits were performed at each estimated peak location. The doublet at 1085.8 keV and 1089.7 keV was not included. A least-squares fit of a linear and quadratic gain calibration was performed on the full set of fitted peak means. The linear calibration was ultimately used to generate calibrated gamma-ray spectra.

Small variations in the gain of the CLOVER leafs was observed over the five day ^{56}Fe experiment. To maintain alignment, the cosine similarity was used to find a scalar multiplier to the gain calibration slope. The cosine similarity is a measure of similarity between two vectors and is defined as the dot product of the vectors divided by their norms

$$S_c = \frac{\vec{A} \cdot \vec{B}}{\|\vec{A}\| \|\vec{B}\|} \quad (3.5)$$

The entire data set was divided into 30-minute time segments and a single segment of the ^{56}Fe data was selected as a reference spectrum. Spectra for every other time segment were individually regenerated using a calibration curve of the form

$$E_\gamma = cm_0(\text{ch}) + b_0 \quad (3.6)$$

where m_0 and b_0 are the slope, with units of ch/keV, and intercept, in units of keV, extracted from the ^{152}Eu data and c is a constant. The maximum cosine similarity for each time segment for values of c between $1 \pm .002$ was found via a grid search.

The FWHM of a photopeak in a single leaf/crystal or for the CLOVER in total-detection mode can be written as the quadrature sum of a constant noise term, N , and a term proportional to the energy of the γ ray [44]:

$$\text{FWHM} = \sqrt{\alpha E_\gamma + N^2}, \quad (3.7)$$

where α is the proportionality constant and E_γ is the γ -ray energy. The parameters α and N are reported in Table 3.1 for each leaf of the two CLOVERs, the two CLOVERs operated in total-detection mode, and the two PopTop detectors. These parameters were obtained from least-squares fits of a Gaussian distribution plus linear background to the common photo-peaks in calibrated ^{152}Eu spectra.

HPGe Detector	$\alpha(\times 10^{-3})$ [keV]	N^2 [keV ²]	Covariance ($\sigma_{\alpha N^2}^2$) [keV ³]
Clover 0, Leaf 1	4.975 ± 0.008	0.834 ± 0.003	-2.286×10^{-12}
Clover 0, Leaf 2	5.299 ± 0.008	0.903 ± 0.003	-2.581×10^{-12}
Clover 0, Leaf 3	6.134 ± 0.009	0.787 ± 0.004	-3.187×10^{-12}
Clover 0, Leaf 4	5.016 ± 0.008	1.017 ± 0.003	-2.756×10^{-12}
Clover 1, Leaf 1	2.214 ± 0.008	1.697 ± 0.004	-3.132×10^{-12}
Clover 1, Leaf 2	2.763 ± 0.011	1.703 ± 0.005	-4.791×10^{-12}
Clover 1, Leaf 3	2.818 ± 0.011	1.658 ± 0.005	-4.455×10^{-12}
Clover 1, Leaf 4	2.675 ± 0.012	1.967 ± 0.006	-6.070×10^{-12}
Clover 0 Total Detection	7.968 ± 0.003	0.068 ± 0.002	-3.309×10^{-13}
Clover 1 Total Detection	4.262 ± 0.003	1.338 ± 0.002	-4.915×10^{-13}
PopTop 0	2.251 ± 0.011	3.212 ± 0.008	-7.298×10^{-12}
PopTop 1	2.085 ± 0.014	4.464 ± 1.0	-1.672×10^{-11}

Table 3.1: GENESIS HPGe energy resolution.

Organic Liquid Scintillators

The light yield resolutions and gains of the EJ-309 scintillators were determined using a procedure similar to that described in [52]. A $0.96 \mu\text{g}$ ^{252}Cf spontaneous fission source was positioned in the center of the GENESIS array and used to construct quasi-monoenergetic neutron response functions for each neutron detector with a coincident γ ray in any other EJ-309 detector serving as the start time for neutron TOF. These response functions were background subtracted using average light yield spectra from TOFs outside the true neutron-gamma coincidence region. An energy deposition spectrum for each quasi-monoenergetic neutron response function was constructed in GEANT4 [30] using the model of the GENESIS array described in Sec. 3.3 with the Mannhart [53] ^{252}Cf prompt fission neutron spectrum (PFNS) as a source positioned at the center of the GENESIS frame. The simulated proton energy deposition in each scintillator was converted into relative light output in MeVee using a fitted EJ-309 proton light yield curve interpolated on a step-by-step basis as the proton slowed to generate the total light output for an event. The EJ-309 relative proton light yield curve was based on prior measurements from Brown *et al.* [52] and Laplace *et al.* [54], fitted with the light yield model of Yoshida *et al.* [55] in accordance with the methods described in [56]. Figure 3.4 shows the experimental TOF vs light-yield for a single EJ-309 detector. The quasi-monoenergetic response functions were selected from the region label ‘‘I’’ and the background was taken by averaging the data in the regions marked ‘‘II’’.

The gain calibration and energy-dependent resolution of each scintillator was determined by simultaneously minimizing χ^2 between four integral-normalized experimentally measured quasi-monoenergetic neutron response functions and the corresponding integral-normalized modeled energy deposition spectra. In the minimization, the experimental quasi-

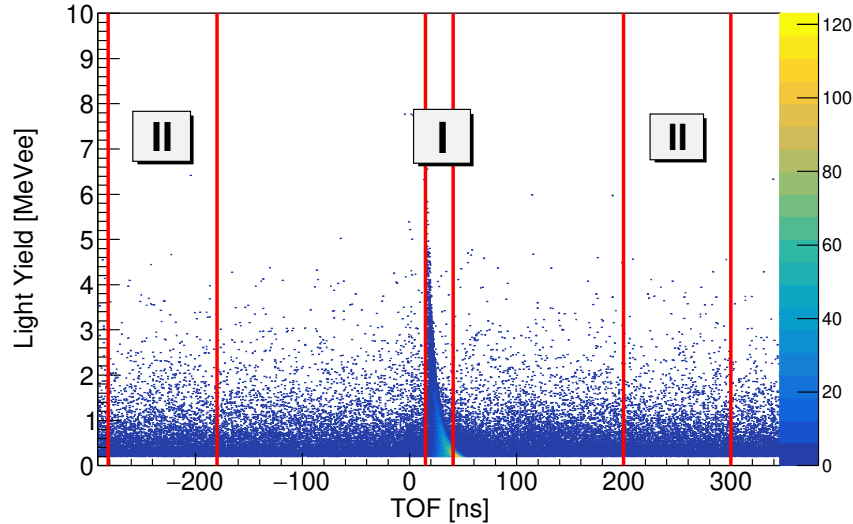


Figure 3.4: A 2D plot of the ^{252}Cf neutron TOF versus light yield for a single EJ-309 detector (Detector 8). The TOF was calculated using a γ in any other EJ-309 detector as a start time. The region labeled I indicates the range of TOFs from which the quasi-monoenergetic response function were selected. The regions labeled II were used to for background subtractions for the response functions.

monoenergetic neutron response functions were scaled by a linear gain calibration of the form

$$L = ax + b \quad (3.8)$$

where L is the light output, x is the ADC channel, and a and b are free parameters. Additionally, the modeled energy deposition spectra were convolved with the Dietze and Klein parameterized resolution function [57]:

$$\frac{\Delta L}{L} = \sqrt{\alpha^2 + \frac{\beta^2}{L} + \frac{\gamma^2}{L^2}}, \quad (3.9)$$

where α , β , and γ are free parameters. The Dietze and Klein resolution function is a semi-empirical model of the detector response: the parameter α represents the variance in the number of photons reaching the PMT photocathode due to location of the light generation, the parameter β represents the statistical variance due to the optical photon transport and the photo-electron generation and multiplication, the parameter γ represents intrinsic noise contributions from the PMT and cables. Figure 3.5 shows the result of the minimization for a single quasi-monoenergetic ($E_n \approx 3.54$ MeV) response function for a single neutron detector at a radial distance of 40.1 cm from the ^{252}Cf source.

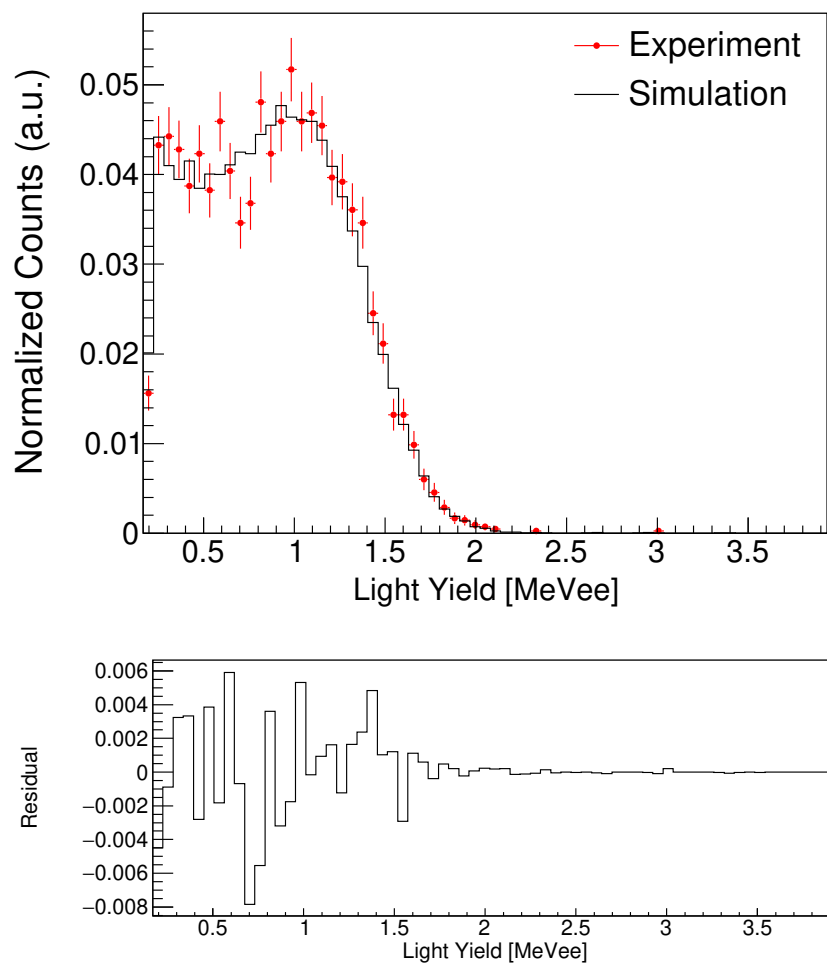


Figure 3.5: Result of the simultaneous fit of scintillator gain and light yield resolution shown for a single experimentally measured quasi-monoenergetic neutron response function for a single EJ-309 neutron detector. Each response function was integral-normalized. For the simultaneous fit across the four response functions, $\chi^2/\text{ndf} = 1.36$.

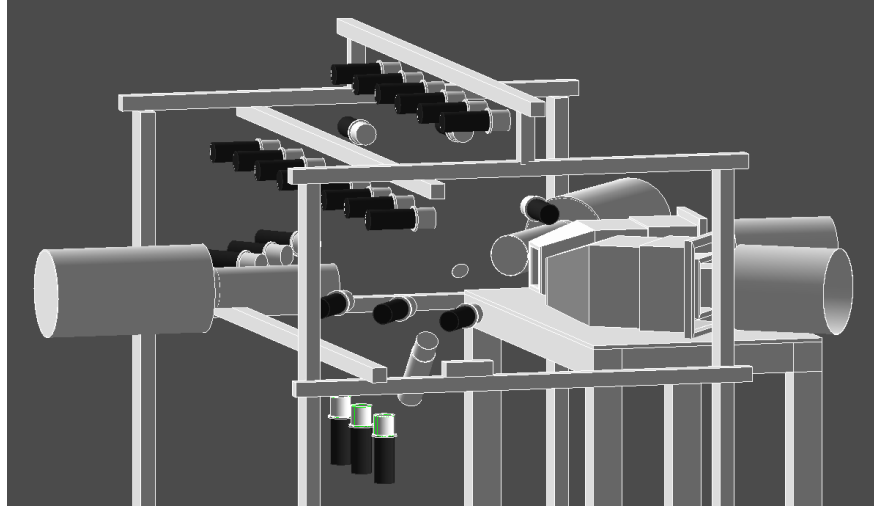


Figure 3.6: A view of the GEANT4 model of GENESIS. For clarity, a few of the supporting aluminum bars have been excluded from the image, but they are present when calculations are performed. Suspended in the center of the array is the model of the ^{56}Fe target.

3.3 Detection Efficiency: Experiment and Modeling

To calculate the detection efficiency of the array for extended volumes and at energies outside the range of ^{152}Eu and the ^{252}Cf PFNS, a detailed GEANT4 [58, 30] model of the GENESIS array was constructed, shown in Figure 3.6. The modeled geometry included the aluminum GENESIS frame, a 2.44×2.44 m section of the concrete floor and ceiling of the room, the scintillators and PMTs, the PopTops, the CLOVER and BGO detectors, and the $\text{LaBr}_3(\text{Ce})$ detector. The model of each EJ-309 cell and PMT included the container of the liquid scintillator, a 3% gas bubble in the scintillator volume [31], the magnetic shield surrounding the PMT, the quartz window between the PMT and the scintillating volume, and the glass of the PMT. The simulation was constructed to store full particle track information for identified volumes of interest. The particle track information included kinetic energy, global time, location, energy deposited in the detector volume, and the energy of the source particle for each step considered.

The modeled response of the HPGe detectors was validated against measurements of the detection efficiency derived from two calibrated sources: a ^{56}Mn distributed source and a ^{152}Eu point source. The neutron response of the GEANT4 model was validated against measurements of the ^{252}Cf PFNS. Descriptions of the gamma-ray and neutron measurements and modeled responses are given below. For all GEANT4 calculations, the Shielding Physics List [59] with the ENDF/B-VIII.0 version of G4NDL [60] was used. The G4EmStandardPhysics option4 was used to most accurately model the performance of the detectors at lower γ -ray energies.

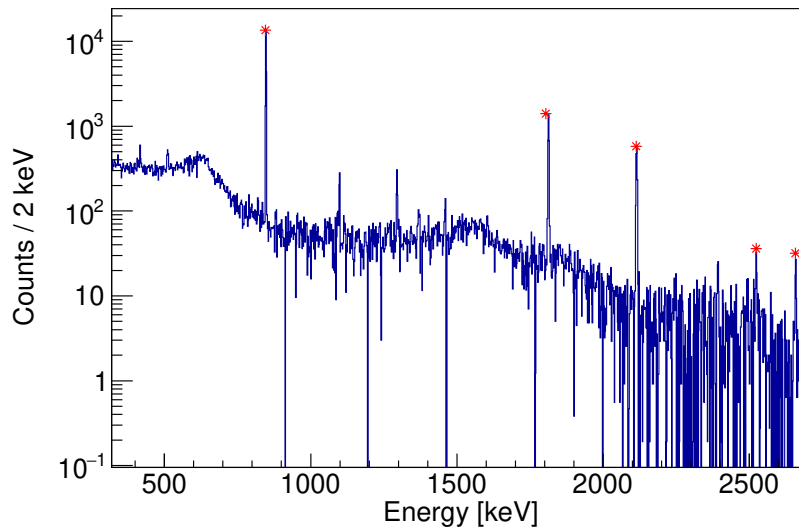


Figure 3.7: Background subtracted gamma-ray spectrum from Clover 0 Leaf 1 taken with the neutron-activated ^{56}Fe target hanging in the center of the GENESIS array. The starred peaks are from the decay of ^{56}Mn : 846.8 keV, 1810.7 keV, 2113.1 keV, 2523.1 keV, 2657.6 keV.

Gamma-Ray Detection Efficiency

Although the γ -ray detection efficiency, ϵ_γ , of a point source can be measured directly using, e.g. a ^{152}Eu sealed source of known activity [37], a correction may be needed to account for distributed sources such as the GENESIS scattering targets emitting gamma rays following neutron inelastic scattering. To measure ϵ_γ and the degree of validity of a point-source approximation for the configuration of the target and HPGe detectors in the GENESIS array, a 99.98% enriched ^{56}Fe elliptical target, with a major radius of 3.6 cm, minor radius of 1.75 cm, and thickness of 0.6 mm (See Sec 6.1 for more details on the target), was irradiated in a TTDB neutron beam produced using a 23 MeV deuteron beam incident on a thick carbon break-up target. The target was placed inside the “vault” (See Fig. 2.2) below the beam box containing the break-up target and irradiated for two days with an average deuteron beam current of approximately $4\ \mu\text{A}$. The $^{56}\text{Fe}(n,p)$ reaction produces ^{56}Mn ($t_{1/2} = 2.5789\ \text{h}$) that beta decays back into ^{56}Fe and gives off γ rays with energies from 846.7 keV to 2657.6 keV, which overlap with the energy range of γ rays given off in ^{152}Eu decay (i.e., 121.8–1408 keV), thus allowing for a test of the point-source approximation and an extension of the efficiency measured using the ^{152}Eu source to higher energy. Two CLOVERs were present, one at 90.0° and 17.0 cm from the center and one at 56.1° and a distance of 23.9 cm. The irradiated Fe target was mounted in the center of the GENESIS frame at an angle of 45° relative to the 90° CLOVER and counted for approximately 3 hours. Figure 3.7 shows the room-background

subtracted γ ray spectrum from the ^{56}Mn decay for a single CLOVER leaf. The peaks used to calculate efficiency are noted by stars. Following the in-array counts, the activity of the target was determined by counting at 31 cm from the front face of an HPGe detector with a well characterized efficiency [61]. The number of decays yielding a specific γ ray during the GENESIS array count, ΔN_i , can be calculated from the measured peak areas P_i , the efficiency of the calibration detector $\epsilon_0(E_i)$, the dwell time in front of the calibration detector T_d , the time between the count in GENESIS and the calibration count T_b and the count time in the GENESIS array T_G

$$\Delta N_i = \frac{P_i/\epsilon_0(E_i)}{1 - \exp(-\lambda T_d)} e^{\lambda(T_b+T_G)} (1 - e^{-\lambda T_G}) \quad (3.10)$$

Figure 3.8 shows the single-leaf efficiency determined using both the ^{152}Eu point source and ^{56}Mn distributed source. Also shown is a fit to the Debertin efficiency function [62, 63] performed using χ^2 minimization. The Debertin efficiency function is

$$\epsilon_\gamma = A_0 \log(E_\gamma) + A_1 \log(E_\gamma)/E_\gamma + A_2 \log(E_\gamma)^2/E_\gamma + A_3 \log(E_\gamma)^4/E_\gamma + A_4 \log(E_\gamma)^5/E_\gamma \quad (3.11)$$

where ϵ_γ is the gamma-ray energy dependent detector efficiency and the A_i are fit parameters. The width of the curve represents the uncertainty in the fit calculated analytically from the covariance matrix V and the sensitivity matrix S using the generalized error propagation formula [64]:

$$\sigma_{\epsilon_\gamma}^2(E_\gamma) = S^T V S \quad (3.12)$$

Since the Debertin function is linear in all the parameters A_i , the sensitivity matrix can be reduced to a vector of partial derivatives $\partial\epsilon_\gamma/dA_i$

$$S^T = (\log(E_\gamma) \quad \log(E_\gamma)/E_\gamma \quad \log(E_\gamma)^2/E_\gamma \quad \log(E_\gamma)^4/E_\gamma \quad \log(E_\gamma)^5/E_\gamma) \quad (3.13)$$

The GEANT4 model of the CLOVER detector was based on specification sheets from the manufacturer obtained at the time of purchase (July 1999). Figure 3.9 shows the GEANT4 implementation of the CLOVER detector with BGO anti-Compton shield. The aluminum can that contains the crystals is not shown so that the models of the crystals themselves are visible. Missing from the available documents was the diameter and length of the coaxial hole. Also unknown were the dimensions of the dead layers in each crystal, which are expected to vary with the age of the crystal and its operational history. These missing pieces of information are crucial to properly modeling the behavior of the individual leaves or the composite detector. A schematic of the dead layers in each CLOVER leaf that were included are shown in Figure 3.10. An additional dead layer surrounding the outer contact exists for n-type HPGe detectors but is generally on the order of microns, whereas the dead layer surrounding the inner contact is on the order of millimeters and was therefore not included [65]. The dead layers were implemented in post-processing by excluding energy depositions within the dead regions.

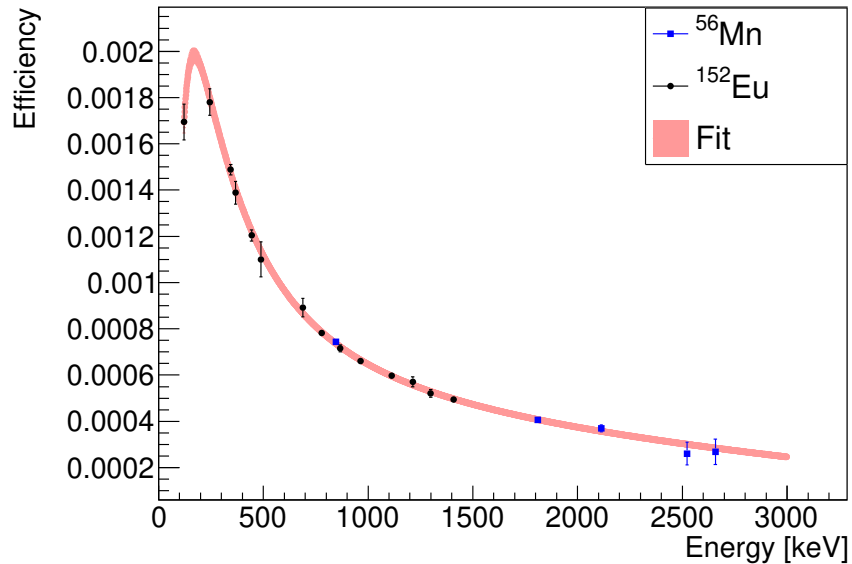


Figure 3.8: Gamma efficiency for Leaf 3 on Clover 0 (at 90°) measured using a $0.916 \mu\text{Ci}$ ^{152}Eu point source located at the center of the GENESIS array. Also shown is the efficiency measured using a neutron-activated ^{56}Fe source, mounted in the center of the array. The decay of ^{56}Mn , produced via $^{56}\text{Fe}(n,p)$, emits γ rays with energies from 846.7 to 2657.6 keV. The curve is a fit to the Debertin efficiency function [62], the width represents the uncertainty in the fit.

To compare the GEANT4 model to the γ -ray measurements, two sets of calculations were performed: one where the γ rays were generated from a point source corresponding to the location of the ^{152}Eu source in the measurement and one with γ rays generated from a volume equivalent to the irradiated ^{56}Fe target, also placed where the target was mounted in the measurement. For both source geometries, the angular distribution was treated as isotropic and the modeled γ -ray energy spectrum was a uniform distribution from 0 to 4 MeV. For each source gamma ray that resulted in a finite energy deposition in at least one crystal, the energy deposited in each crystal was tallied, excluding energy depositions occurring within the dead-layers. The trigger probability was included by calculating the probability P from the fits to Eq 2.8 for each leaf, sampling a random number $0 \leq \xi \leq 1$. There were two requirements for the event to be accepted: $\xi > P$ and if the energy deposited was within 2.5 keV of the source gamma. If a source gamma ray gave rise to ≥ 2 events that passed the trigger probability in the same clover, and if both events deposited energy above the experimental add-back energy thresholds, then the energies were summed and if the summed energy was within 2.5 keV of the source gamma, the summed event was included in the simulated total detection mode histograms.

To help constrain the size of the dead layer surrounding the coaxial hole, the setup in

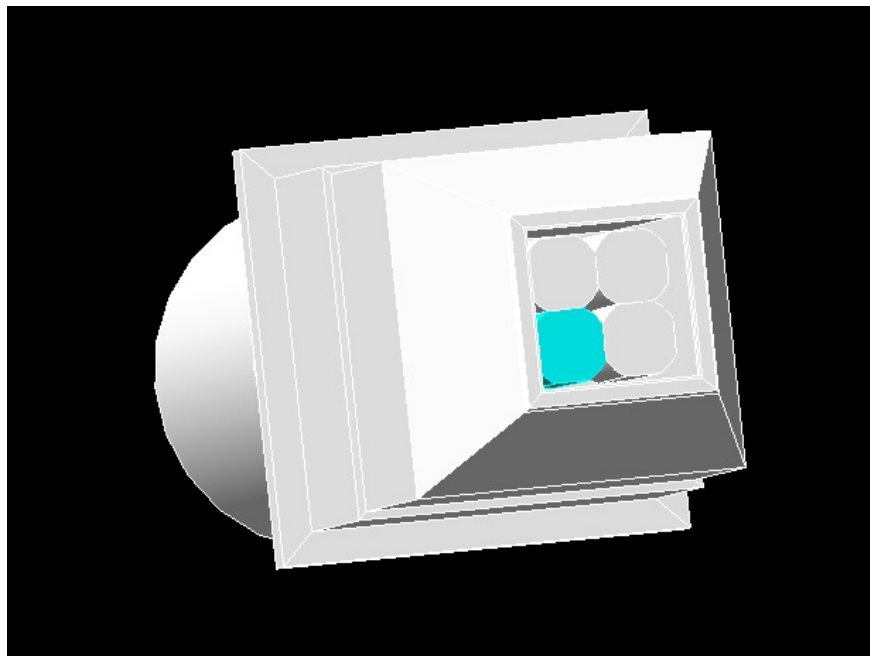


Figure 3.9: The CLOVER GEANT4 model without the aluminum can containing the crystals.

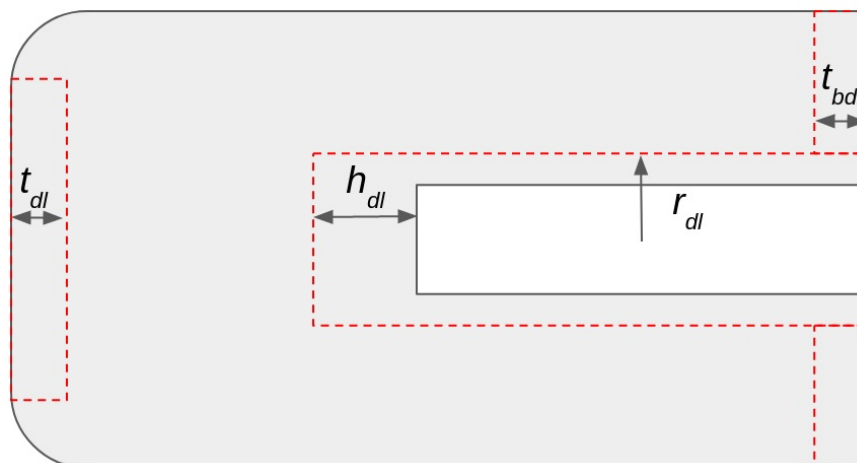


Figure 3.10: Schematic representation of the dead layers in a CLOVER leaf. The dead layer at the front of the crystal is of order $t_{dl} \sim 20 \mu\text{m}$, the length of the dead layer surrounding the coaxial hole is $h_{dl} \sim 12 \text{ mm}$, the radius of the dead layer surrounding the coaxial hole is $r_{dl} \sim 5 \text{ mm}$.

Figure 3.11 was used. A ^{137}Cs point source was attached to the back of a 10 cm long copper tube, 2.54 cm in diameter with a 1 mm diameter hole. The collimated source was attached

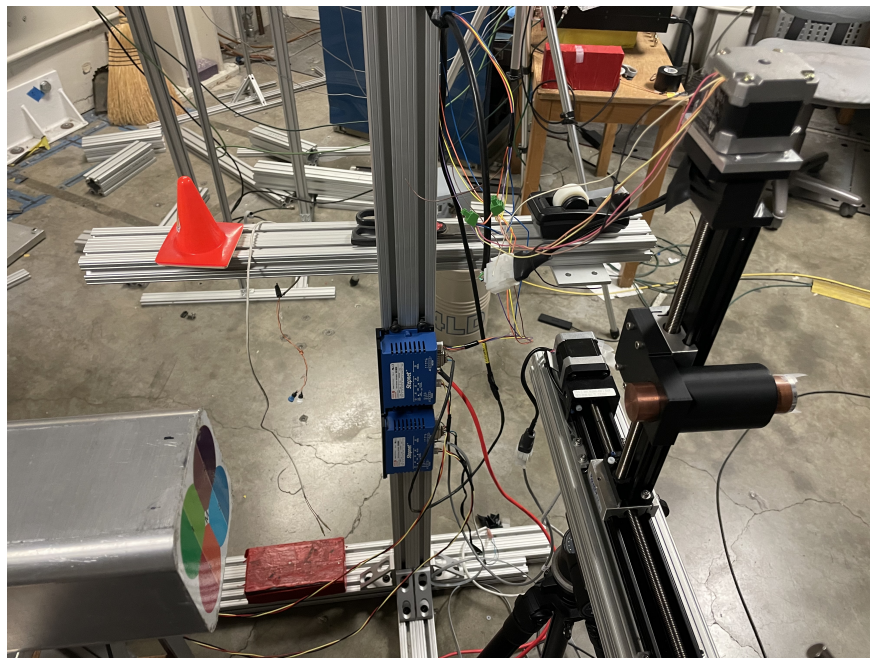


Figure 3.11: Setup for the CLOVER scanning. A ^{137}Cs source was attached to the back of 10 cm long copper collimator with a 1 mm diameter hole. The collimator was mounted to a 2D translation stage. The stage was positioned 36.64 cm from the front face of the crystals.

to a 2D translation stage that was aligned to the center of the CLOVER detector, which was located 36.64 cm from the front face of the HPGe crystals. The collimated source was moved horizontally across the midline of each leaf, stopping every 0.2 cm to count for 10 minutes. The stage recorded its position every second. The CLOVER data were recorded using a Mesytec MDPP16 board configured to the SCP firmware. The “TF_INT_DIFF” parameter was set to its maximum value (see Sec. 2.4). The count rate for the ^{137}Cs peak as a function of the collimated source location for a scan across Leaf 2 is shown in Figure 3.12. The collimated source was also modeled in GEANT4. A set of simulations were run with the collimated source at the experimental locations and the number of 661.657 keV gamma rays was recorded using the same processing described above. The values for the dead layer were the same for all the simulations in the set. Multiple sets of simulations were run with different parameters for r_{dl} and h_{dl} . The best agreement between the simulated and experimental distributions was achieved with a thin dead layer at the front of each individual crystal of thickness $t_{dl} = 20 \mu\text{m}$ and a larger dead region surrounding the inner contact of radius $r_{dl} = 6 \text{ mm}$ and length $h_{dl} = 2 \text{ mm}$. Figure 3.13 shows the simulated and experimental count rates as a function of collimator location for Leaf 2 using the dead layers specified above.

Figure 3.14 shows the modeled and experimentally measured γ -ray detection efficiency for a single CLOVER leaf. To quantify the agreement between experimental and simulated

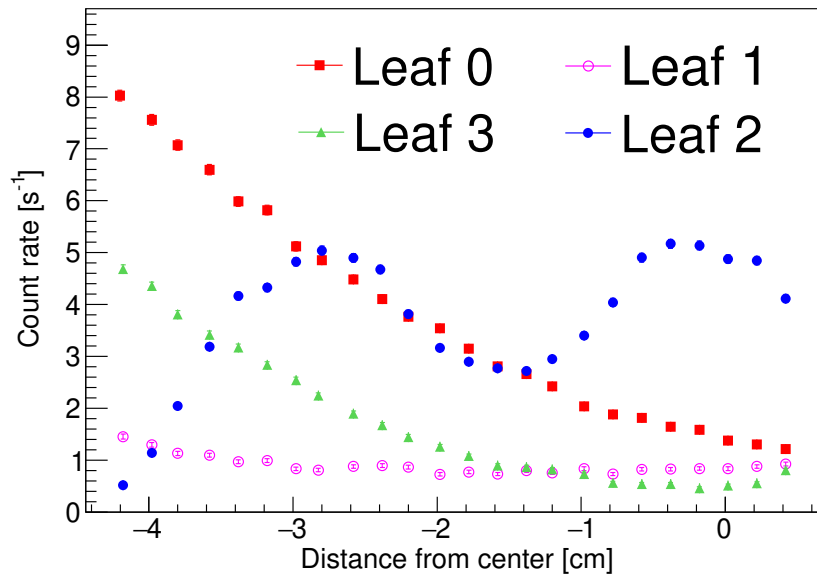


Figure 3.12: Count rate in the 661.657 keV ^{137}Cs peak as a function of the collimator+source position for all leaves. The scan was done across Leaf 2.

efficiency, the Debertin efficiency function [62] was fitted to either the ^{152}Eu data, from 244.7 to 1408 keV, or the ^{56}Mn data from 846.7 to 2657.6 keV, using a χ^2 minimization. The average deviation of the simulations from the fitted curves was computed. On average, across the energy range 244.7 to 1408.0 keV, the ^{152}Eu data agrees with the point source simulation to within $2.1 \pm 2.3\%$ and the extended source simulation to within $1.1 \pm 3.3\%$. On average, across the energy range 846.7 to 2657.6 keV, the ^{56}Mn data agrees with the point source simulation to within $3.0 \pm 6.8\%$ and the extended source simulation to within $2.7 \pm 7.3\%$.

The CLOVERs can be operated in total detection mode, where the energies of coincident γ -ray interactions in separate leaves are summed to recover the full energy deposited by the incident γ ray. The add-back factor is a measure of the increase in photopeak efficiency from a CLOVER operating in total detection mode (add-back multiplicity ≥ 1) over a CLOVER operating in full singles mode [44]. Figure 3.15 shows the add-back factor for total detection mode measured using data obtained from a $0.916 \mu\text{Ci}$ ^{152}Eu source and results from a GEANT4 calculation. As anticipated, there is no loss in photopeak efficiency at low energy, and a gain of up to 45% is achieved at 1408 keV. The difference between the observed add-back factors for the two CLOVERs is due primarily to the interplay of four factors: the gain of each CLOVER leaf, the energy threshold, the non-unity trigger probability for low-energy γ -ray events, and the differences in the dead layers of each crystal. Further experimental work is planned to investigate the influence of the dead layer at the back of each CLOVER leaf on the calculated add-back factor.

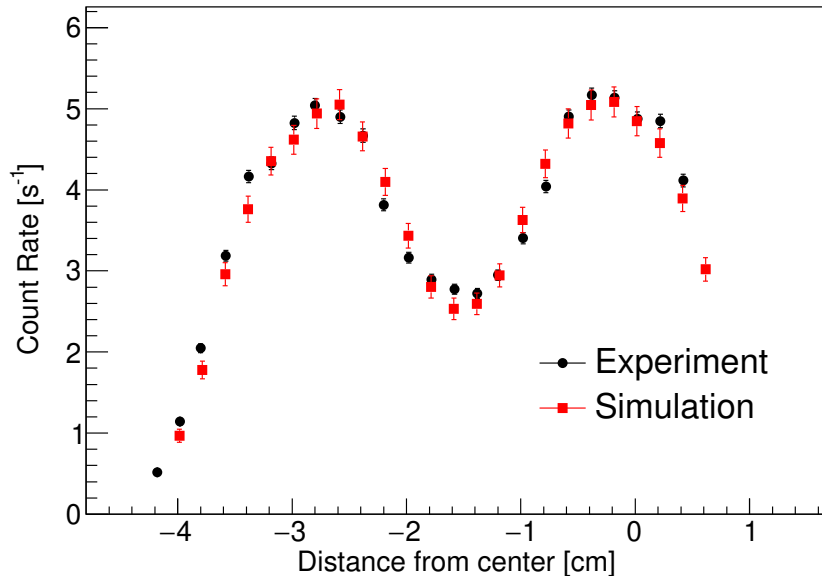


Figure 3.13: Experimental and simulated 661.657 keV count rate as a function of collimator+source location.

^{252}Cf Spontaneous Fission Neutron Measurements

Measurements of calibrated neutron sources with the same dimensions as a target of interest for the GENESIS array are infeasible. More practical is a measurement using a neutron source of known activity and geometry that can be used to benchmark a model of the neutron detectors, which can then be used to calculate efficiencies for each specific target geometry. This section describes a measurement and calculation of the neutron detector response to a ^{252}Cf spontaneous fission source.

^{252}Cf is an ideal source to use for characterizing the neutron response of the GENESIS EJ-309 organic scintillator detectors. It has a half-life of 2.645 years, and decays via spontaneous fission 3.09% of the time, with $\bar{\nu} = 3.759$ giving a neutron emission rate of $2.314 \times 10^6 \text{ s}^{-1} \mu\text{g}^{-1}$. The α -decay branch goes to ^{248}Cm with a half-life of 3.48×10^5 years and decays via spontaneous fission 8.39% of the time. Neither α decay branches lead to detectable γ 's that could affect measurements of neutrons using fission γ 's as a tag. The prompt fission neutron spectrum (PFNS) of ^{252}Cf has been well studied because of its importance as a neutron source. The standard evaluation of the ^{252}Cf PFNS was done by Mannhart in 1989. The data available at that time were fit using least squares to

$$N_W(E_n) = \frac{2}{\sqrt{\pi b a^3}} e^{-ab/4} e^{-E_n/a} \sinh(\sqrt{b E_n}) \quad (3.14)$$

with $a = 1.209 \pm 0.015 \text{ MeV}$, $b = 0.836 \pm 0.107 \text{ MeV}^{-1}$, and $\text{cov}(a, b) = -1.573 \times 10^{-3}$. Figure 3.16 shows the PFNS using the results of Mannhart. The width of the curve represents

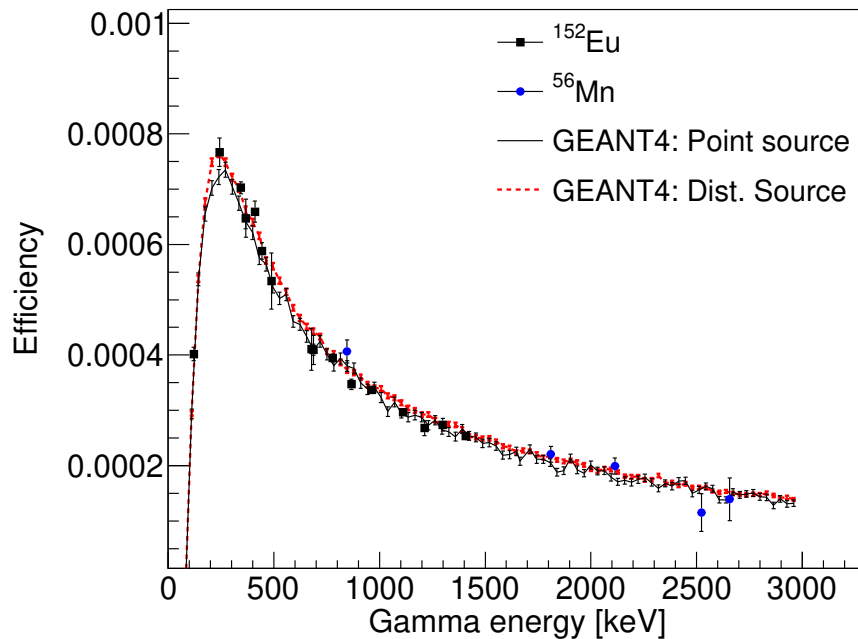


Figure 3.14: Comparison of simulated (red and black lines) and experimentally measured (data points) γ -ray detection efficiency for a Leaf 3 of Clover 1 in the GENESIS array. The simulations were run with source geometries equivalent to the ^{152}Eu point-source and extended ^{56}Fe source.

the uncertainty in the spectrum from the fit and the uncertainties and covariance. The main drawback of using the ^{252}Cf spontaneous fission to characterize the response of the neutrons detectors is made clear in Figure 3.16: the number of neutrons drops by an order of magnitude from 1 MeV to 6 MeV such that data must be collected for sufficiently long in order to characterize the high neutron energy response.

A $0.96 \mu\text{g } ^{252}\text{Cf}$ source, enclosed in a cylinder of 304L stainless steel, 2.13 cm tall, with an outer radius of 0.471 cm, a wall thickness of 0.254 cm, with a 0.775 cm long cap on top, and 0.851 cm long cap on the bottom was used to characterize the neutron detector response. Figure 3.17 shows the GEANT4 model of the ^{252}Cf container and the model of the EJ-309 detectors. Data were taken with the source at the center of the GENESIS frame without the CLOVERs, BGOs, and PopTops present. To distinguish neutrons from γ rays in the EJ-309 detectors, two software constraints were applied: only events depositing greater than 0.2 MeVee were accepted and events with a tail-to-total pulse integral greater than a certain value were classified as neutrons (e.g., tail-to-total > 0.18 for the scintillator shown in Fig. 2.4). Neutron energy was determined via TOF with a coincident γ -ray interaction in another EJ-309 detector acting as the start time. Ten of the EJ-309 detectors were not operational during this measurement. The gains and light output resolutions of the detectors

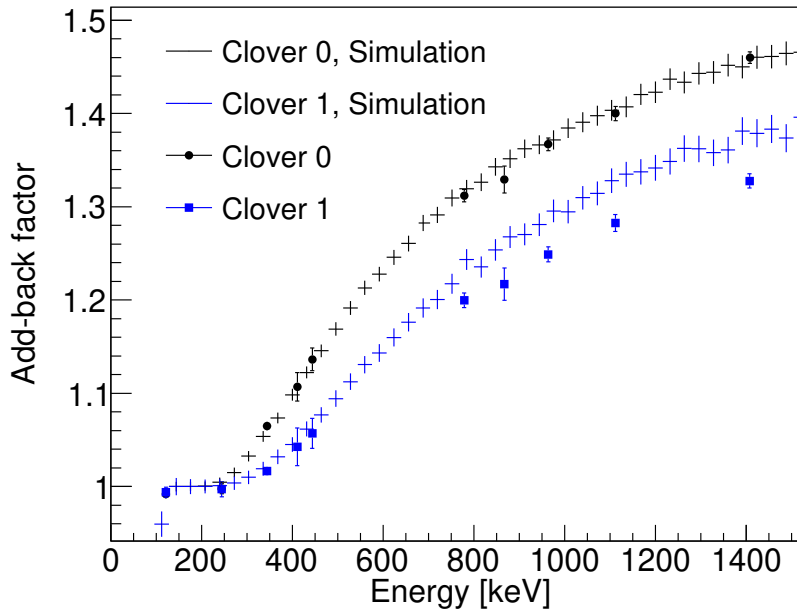


Figure 3.15: Add-back factor for the two CLOVER detectors measured using a ^{152}Eu source. There is no loss in efficiency at low energy and a gain of up to 45% at 1408 keV. The cross are calculations of the add-back factor using the GEANT4 model described in the text. The experiment agrees with the calculation to within 1% for Clover 0 and within 4.5% for Clover 1.

were determined using the method described in Sec. 3.2.

To accurately model the observed neutron spectrum, the ^{252}Cf PFNS from Mannhart [53] was transported through the stainless steel housing. Additionally, a small fraction of fission-product isomers undergo decay within 10 – 50 ns following fission, emitting γ rays that give rise to neutron TOF values with ostensibly short durations, resulting in an overestimation of the high-energy neutron flux [66]. The non-prompt γ -ray tag was modeled by building $\gamma\gamma$ time differences, corrected for γ -ray flight paths from the experimental data. For example, Fig. 3.18 shows the $\gamma\gamma$ time differences between a single EJ-309 detector and every other scintillator along with a fit to the data using a Gaussian distribution plus a linear background (the latter fit to time differences between -100 to -30 ns and 30 to 100 ns). To account for both the temporal resolution and the non-prompt γ -ray emission, the simulated TOF was convolved with the $\gamma\gamma$ time difference distribution via random sampling. A GEANT4 calculation was performed with the ^{252}Cf source modeled as an isotropic point source located inside the stainless steel housing emitting one neutron at a time, with an energy sampled from the PFNS from Mannhart [53].

Simulated proton energy depositions in each scintillator volume were then converted

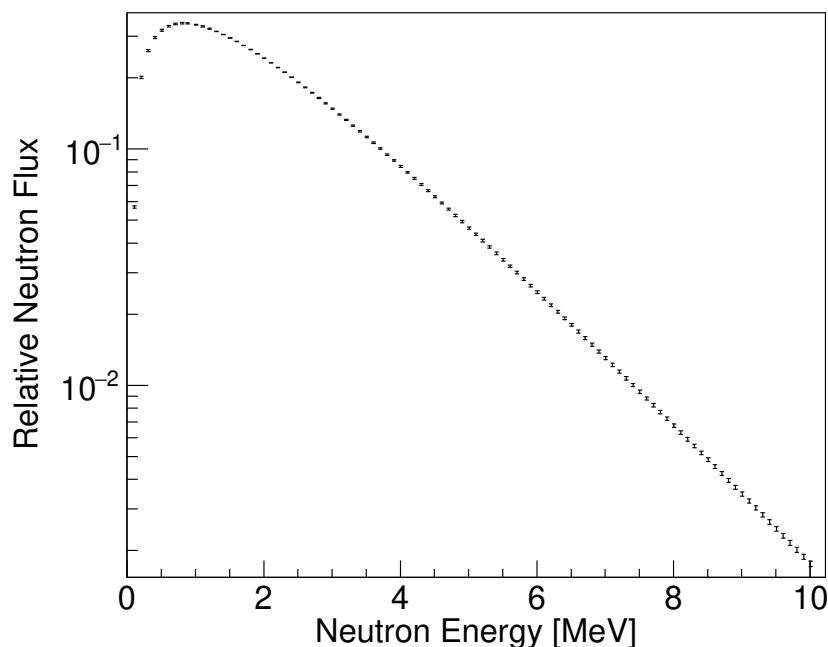


Figure 3.16: ^{252}Cf PFNS from the evaluation of Mannhart. The errors represent the uncertainty on the spectrum from the reported fit parameter uncertainties and covariance.

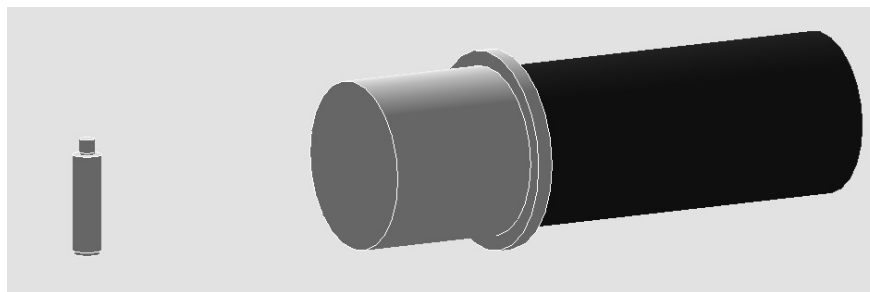


Figure 3.17: GEANT4 model of the EJ-309 organic liquid scintillator detector used in GENESIS (right hand side) and the ^{252}Cf container (left hand side).

into relative light output in MeVee using the methods described in Section 3.2. The total simulated light output was then convolved with the experimentally determined light output resolution (see Sec. 3.2) for each EJ-309 detector and a light output threshold was applied corresponding to that set in post-processing of the experimental data. The TOF for each simulated neutron event was taken from the simulated global event time broadened by re-sampling experimental ^{252}Cf $\gamma\gamma$ data as described above. Figure 3.19 shows a comparison of the experimental and simulated neutron energy spectra in ratio to the ^{252}Cf PFNS from

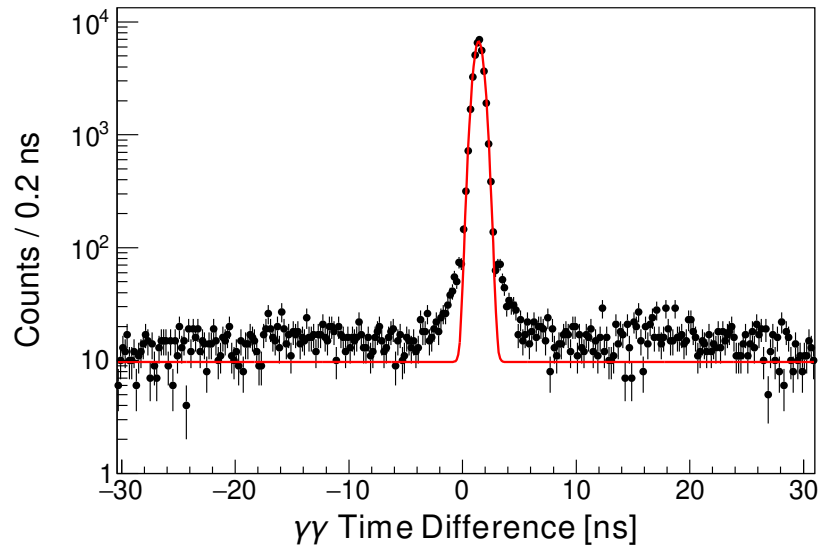


Figure 3.18: $\gamma\gamma$ time differences from ^{252}Cf for a single EJ-309 detector (Detector 4) and every other scintillator in the GENESIS array. The dashed (red) curve is a Gaussian distribution plus linear background fit to the data. The linear background was fitted on data from -100 to -30 ns and 30 to 100 ns. The tailing on either side of the peak is due to coincidences with non-prompt fission γ -rays.

Mannhart [53]. The empirical and simulated spectrum ratios in Figure 3.19 were separately normalized to the integrated efficiency determined experimentally and from the simulation, respectively. There is good agreement across the full energy range covered, including the ostensible increase in observed neutron flux above 10 MeV.

The neutron detection efficiency used to extract cross sections in GENESIS experiments was calculated with the validated GEANT4 model using a uniform energy, isotropic neutron source with a spatial geometry equivalent to the scattering target under investigation. This calculation was performed for an ellipsoidal target composed of air with a major radius of 3.6 cm, minor radius of 1.75 cm, and thickness of 0.6 mm hanging in the center of the array at an angle of 50.3° relative to the $-\hat{x}$ axis (See Chapter 6 for details about the target and location). The simulation output was processed as described above. The uncertainties on the light yield resolution parameters and the gain calibration, from the procedures described in Section 3.2, give rise to a systematic uncertainty in the efficiency that was calculated using the Cholesky decomposition [67] of the covariance matrix to generate a random set of light yield resolution and gain parameters. Let $\hat{\beta}$ be the values from the result of the simultaneous light yield and resolution fit, with a covariance matrix \mathbf{V} . The Cholesky decomposition can be thought of as the square-root of a matrix

$$\mathbf{V} = \mathbf{L}\mathbf{L}^T \quad (3.15)$$

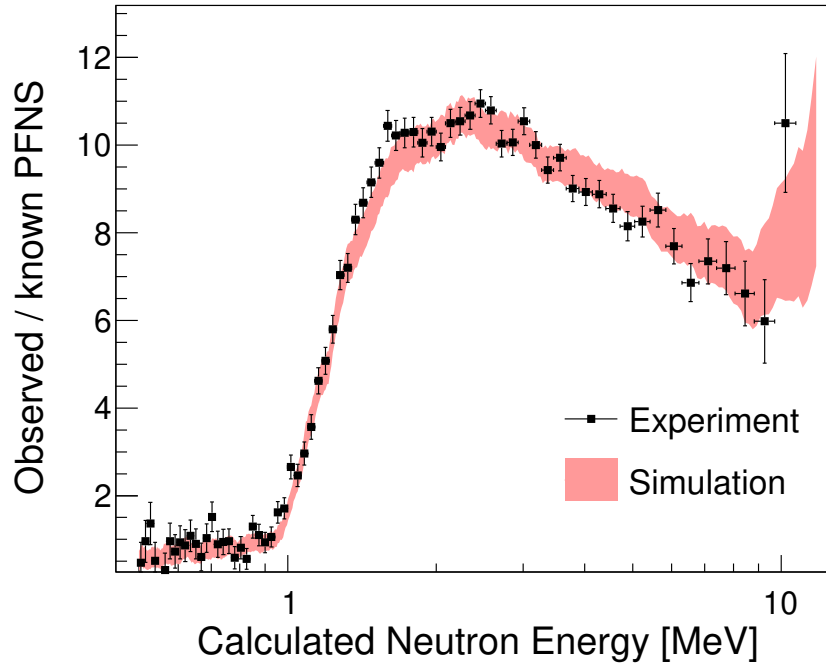


Figure 3.19: Measured and modeled neutron spectrum in a single EJ-309 detector in ratio to the ^{252}Cf PFNS from Mannhart [53]. The width of the simulated curve reflects the statistical uncertainty of the calculation. Neutron energy was calculated from TOF using the rest of EJ-309 detectors in the array as γ detectors. The presence of a small fraction of non-prompt gamma rays gives rise to an increase in the observed-to-modeled ratio at high neutron energy. [66]

Let $\vec{X} \sim \mathcal{N}(0, 1)$ be a set of random numbers. A new set of parameters $\vec{\beta}$ can be generated with proper correlations by

$$\vec{\beta} = L\vec{X} + \hat{\beta} \quad (3.16)$$

The simulation was then reprocessed with these new parameters and the efficiency was recalculated. This process was repeated for 10,000 trials and the systematic uncertainty was added in quadrature with the statistical uncertainty from the simulation. Figure 3.20 shows the calculated total neutron detection efficiency of the sixteen operational detectors (Detectors 0 - 15) from the ^{252}Cf measurement with a light yield threshold of 0.2 MeVee. The detectors are located at various radial distances from the center of the array (see Appendix A for exact locations) and represent 61.6% of the total neutron detector solid angle. The full response function of the neutron detectors contains more information than shown in Figure 3.20. The details of the neutron detector response functions will be given in Sec. 5.2 but the construction follows the same procedure outline above.

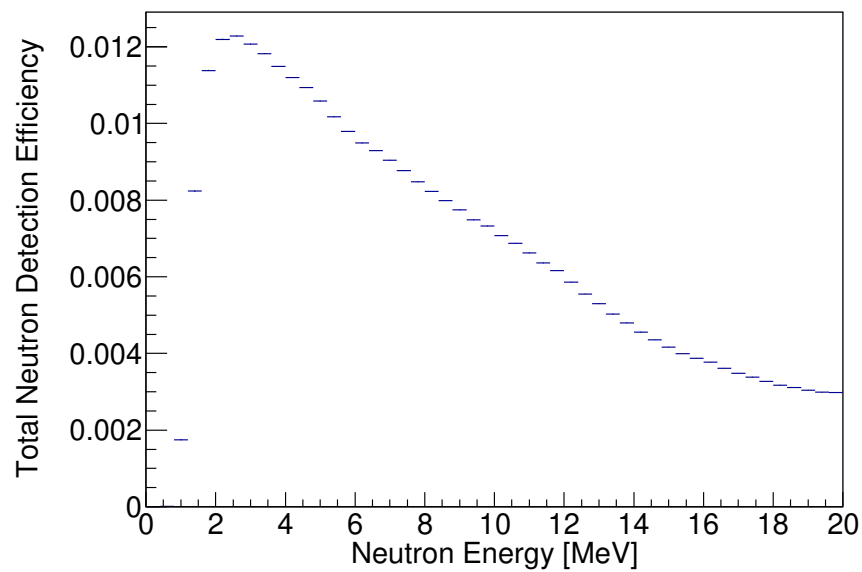


Figure 3.20: Total neutron detection efficiency as a function of neutron energy for 16 EJ-309 detectors (representing 61.6% of the total neutron detector solid angle) calculated using GEANT4. The y -error bars are a quadrature sum of the statistical uncertainty and the systematic uncertainty arising from the scintillator light yield gain and resolution calibration parameters.

Chapter 4

Neutron Scattering Cross Sections: Theory and Modeling

The previous two chapters detailed the construction of the GENESIS array, the neutron beam facility at which it is located and the operating characteristics of the detectors, including a detailed and validated GEANT4 model. This chapter and the next will serve as a transition between those experimental details and characteristics and Chapters 6-8 which present the results of nuclear reaction cross section measurements with GENESIS. This transition will be facilitated by way of a brief discussion of nuclear reaction theory and modeling (this chapter) and the different methodologies employed to analyze and extract cross sections (Chapter 5). The importance of this work is the development of the forward modeling approach as a general method to bridge the gap between nuclear data experimentalists and evaluators.

4.1 Theoretical Background

Currently, there is not one single model that fully describes all the observed properties of all observed nuclei. Rather, there exists a collection of models, with various degrees of validity, based on a variety of different assumptions, that give rise to computations and solutions of varying degrees of difficulty and complexity. Similarly, and notwithstanding the dependence on the nuclear structure, there exists various models for the description of nuclear reactions, based on the types of nuclei involved, the total kinetic and mass energy available, and the predicted observables. The commonly used codes used to calculate nuclear reaction cross sections (e.g. TALYS [68], Empire [69], YAHFC [70], etc.) have implementations of these various models and their use cases. For the fast neutron induced reactions observed at GENESIS, the number of models can be limited to those that deal with direct and compound reactions. Figure 4.1 shows the result of a TALYS1.96 calculation of the total cross section for neutrons on ^{56}Fe and the contributions from the different reaction mechanisms. The details of the pre-equilibrium exciton model used by TALYS will not be given here because the pre-equilibrium reactions do not contribute significantly in the range of neutron energies

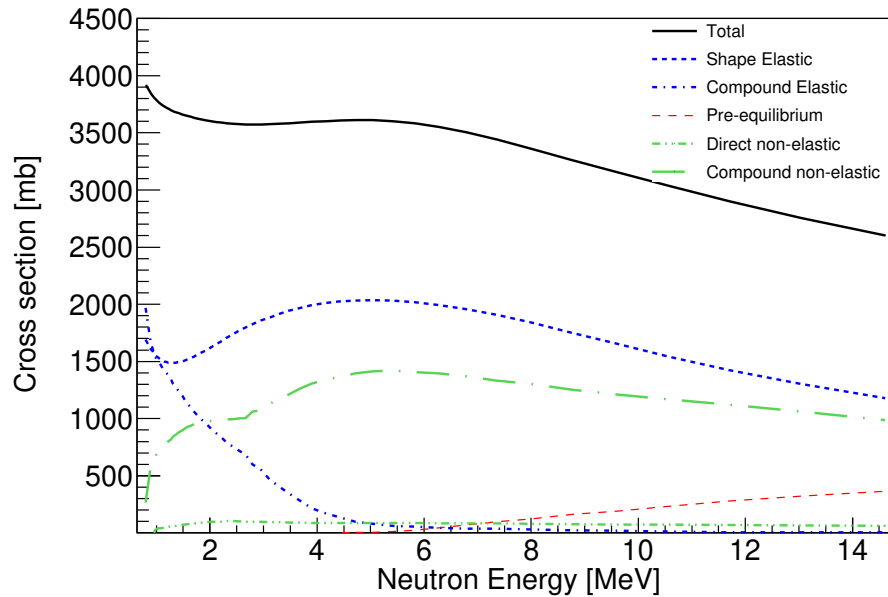


Figure 4.1: Total $^{56}\text{Fe}(n,\text{tot})$ cross section calculated with TALYS1.96. The contributions from the different reaction components are also shown.

from 14 MeV TTDB. This section will give a brief description of the relevant models as they are implemented in TALYS1.96.

The computation of nuclear reaction cross sections with TALYS starts with a calculation of the total reaction cross section, the direct elastic and inelastic scattering cross sections and the direct elastic and inelastic secondary particle distributions. TALYS uses ECIS-06 [71] to perform these calculations. Computing these cross sections involves solving the Schrödinger equation describing the interaction of a projectile (a neutron) and a target nucleus (e.g. ^{56}Fe) via a complex mean-field potential. Let the wave function describing the internal structure of projectile p be ϕ_{pi} , ϕ_{tj} be the wave function describing the internal structure of the target nucleus t and $\psi_{ij}(\vec{r})$ be the wave function of the relative motion. Then

$$\Psi_{model} = \sum_{i,j} \phi_{pi} \phi_{tj} \psi_{ij}(\vec{r}). \quad (4.1)$$

The total Hamiltonian \mathcal{H} describing the interaction between the projectile and target can be written as a sum of the Hamiltonians describing the internal structure of the two interacting bodies, H_p and H_t , the kinetic energy for the relative motion, $\hbar^2/2\mu\nabla^2$ where μ is the reduced mass of the system, and the interaction potential, called the optical model potential (OMP), U ,

$$\mathcal{H} = H_p + H_t - \frac{\hbar^2}{2\mu} \nabla^2 + U \quad (4.2)$$

The OMP for neutrons (nOMP) used in all TALYS calculations in this work is the default local phenomenological potential of Koning and Delaroche [72]:

$$U(r, E) = -a_v(E)V_V(E, r) - ia_w(E)W_V(E, r) - ia_{wd}(E)W_D(E, r) + a_{vso}(E)V_{SO}(E, r) \cdot \mathbf{l} \cdot \mathbf{s} + a_{wso}(E)iW_{SO}(E, r) \cdot \mathbf{l} \cdot \mathbf{s} , \quad (4.3)$$

where E is the energy of the incident neutron in the laboratory frame, r is the relative distance between the two interacting bodies, \mathbf{l} is the orbital angular momentum operator, and \mathbf{s} is the spin angular momentum operator. The default values of the parameters a_i for ^{56}Fe are given in Figure 4.2. The dominant contribution is the first term, corresponding to the real volume-centered potential well. The imaginary surface-central, W_D , and the

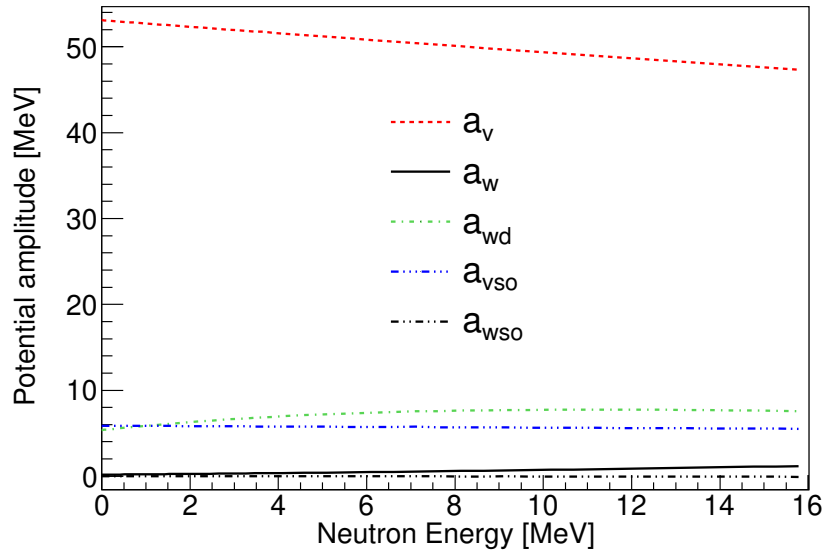


Figure 4.2: Parameters for the contributions of the various potential wells in the Koning-Delaroche neutron optical model potential for ^{56}Fe .

real spin-orbit, V_{SO} , terms contribute in roughly equal proportion across the energy range relevant for 14 MeV TTDB on Carbon. The contributions from the remaining terms, the imaginary volume-central, W_V , and imaginary spin-orbit, W_{SO} , potentials are minimal. The Schrödinger equation can be formally written as

$$(E - \mathcal{H})\Psi_{model} = 0 \quad (4.4)$$

where E is the total energy available.

The details of how this equation is solved can be found in e.g. [73] and the references therein. The main result of the calculation is a matrix whose elements are collision or scattering amplitudes that describe the probability, based on the specific optical potential

used and other assumptions about the coupling of the incident and outgoing wave, that a given incident projectile plus target configuration will result in a specific ejectile plus residual configuration. Let $f_{\alpha\beta} \sim \langle \beta | U | \alpha \rangle$ be the scattering amplitude for the reaction $A(a,b)B$ with incident configuration α and outgoing configuration β . The differential cross section for elastic or inelastic neutron scattering is

$$\frac{d\sigma_{\beta}}{d\Omega} \sim |f_{\alpha\beta}(\theta, \phi)|^2 \quad (4.5)$$

The total cross section can be found by factoring $f_{\alpha\beta} \sim \sum_{\ell} \eta_{\ell\alpha\beta} P_{\ell}(\cos \theta)$, where $\eta_{\ell\alpha\beta}$ is the angular momentum dependent scattering amplitude and P_{ℓ} 's are the Legendre polynomials, and taking advantage of the orthogonality of the Legendre polynomials. The energy spectrum of secondary particles can be calculated based on the excitation energy of the residual nucleus

$$E_{n'} = E_n - E_x \quad (4.6)$$

with $E_x = 0$ for elastic scattering.

The calculations outlined above can be used to determine σ_{total} , the total cross section (i.e. the probability for the neutron to undergo any reaction with the target nucleus) and the direct component σ_{direct} . The direct component is partitioned between the shape elastic cross section $\sigma_{shape\,elas}$ and the direct inelastic to level i , $\sigma_{inel\,i}^{dir}$

$$\sigma_{direct} = \sigma_{shape\,elas} + \sum_i \sigma_{inel\,i}^{dir} \quad (4.7)$$

The remaining cross section is partitioned between compound and pre-equilibrium reactions.

$$\sigma_{total} = \sigma_{direct} + \sigma_{compound} + \sigma_{preeq} \quad (4.8)$$

More exactly, the total cross section can be written as a sum over the different reaction channels α arising from the different reaction mechanisms

$$\sigma_{total} = \sum_{\alpha} \sigma_{\alpha}^{direct} + \sum_{\alpha} \sigma_{\alpha}^{compound} + \sum_{\alpha} \sigma_{\alpha}^{preeq} \quad (4.9)$$

The partitioning of the total direct cross section into the elastic and inelastic channels is taken from the scattering or collision matrix. The partitioning of the total compound cross section into the various available reaction channels is calculated in TALYS following the Hauser-Feshbach formalism.

Hauser-Feshbach theory is an extension of the theory of compound reactions to isolated resonances to a region of the excitation energy where the average space between individual levels is small and the amount of overlap between levels is large, i.e. where the nuclear level density becomes large, and the nucleus takes on statistical properties. Let the probability for given compound reaction $A + a \rightarrow C^*$ to occur be Γ_{α} . The probability for the decay of

that compound nucleus into a given open channel, $C^* \rightarrow B + b$ is Γ_β . The cross section for the reaction $A + a \rightarrow B + b$, ignoring spin-dependent factors, is [73]

$$\sigma_{\alpha\beta} = \frac{\pi}{k_\alpha^2} \frac{\Gamma_\alpha \Gamma_\beta}{(E - E_r)^2 + (1/2\Gamma)^2} \quad (4.10)$$

where E_r is the energy of the resonance and Γ describes the total probability for the decay of the compound system into any available open channel. The factor π/k_α^2 is a phase-space term that comes from a statistical argument about the probability to form the compound system based on the number of states $n(p_\alpha = \hbar k_\alpha)$ available in the momentum range dp_α .

The extension of the Hauser-Feshbach model from Eq 4.10 involves replacing the partial widths Γ_β with transmission coefficients $\tau_{\alpha\beta}$ calculated from the optical model described above, and the inclusion of a term dependent on the nuclear level density. A key difference between the various nuclear reactions is how the Hauser-Feshbach equations are solved; TALYS and Empire use deterministic approaches and YAHFC uses Monte Carlo. Deterministic solvers are faster but information on some complex observables is more difficult to obtain. The Monte Carlo method allows the code to be used as an event generator, at the cost of increased computation times.

TALYS nuclear level density model `ldmodel 1` was used in this work and is defined by two functions, joined at a transition or ‘‘matching’’ energy E_m

$$\rho(E_x, J, \Pi) = \begin{cases} \rho_{CT}(E_x, J, \Pi) & E_x \leq E_m \\ \rho_{Fermi}(E_x, J, \Pi) & E_x \geq E_m \end{cases}. \quad (4.11)$$

The level densities ρ , ρ_{CT} , and ρ_{Fermi} depend on the excitation energy, E_x , the total spin J , and the parity π of the compound system. ρ_{CT} uses the constant temperature (Gilbert and Cameron [74]) model with adjustable parameters T and E_0

$$\rho_{CT}(E_x, J, \Pi) = \frac{1}{2} \frac{2J+1}{2\sigma^2} \exp\left(-\frac{(J+1/2)^2}{2\sigma^2}\right) \frac{1}{T} \exp\left(\frac{E_x - E_0}{T}\right). \quad (4.12)$$

The term $1/2$ at the front describes the equal partition between positive and negative parity states. The terms as a function of J describe the distribution of spins, modeled as a Gaussian with an excitation energy dependent width of $\sigma(E_x)$. The final terms, as a function of $E_x = E_n + S_n$ describe the energy dependent distribution of levels. The Fermi Gas model [75] is used to describe the level density above the matching energy E_m , parameterized by the same spin parameter σ , an energy dependent level density parameter $a(U)$ and an energy shift parameter Δ

$$\rho_{Fermi}(E_x, J, \Pi) = \frac{1}{2} \frac{2J+1}{2\sqrt{2\pi}\sigma^3} \exp\left(-\frac{(J+1/2)^2}{2\sigma^2}\right) \frac{\sqrt{\pi} \exp(2\sqrt{aU})}{12 a^{1/4} U^{5/4}} \quad (4.13)$$

where $U = E_x - \Delta$.

The full expression for the compound nuclear reaction cross section can be found in [72], but to highlight some of the main features and relevant parameters, a compact form of the equation (Eq. 13.16) is reproduced below:

$$\sigma_{ab} = \frac{\pi}{k_a^2} \frac{\tau_a \tau_b}{\sum_c T_c} W_{ab} , \quad (4.14)$$

where τ_a is the transmission coefficient for the entrance channel, τ_b is the transmission coefficient for a given exit channel b , and W_{ab} is a width correction factor that is included for computations at incident neutron energies less than some adjustable energy $E_{widthfluc}$. The full expression for the angular distribution of secondary particles is given in Eq. 13.9 of [68] and depends on the angular momenta of the projectile, compound and residual nuclei and the ejectile. The angular distribution for particle type i at energy E from an incident neutron at energy E_n , $\phi(E_n, E_i, \theta_i)$ with θ defined relative to the incident neutron beam can be written as a sum of Legendre polynomials weighted by coefficients α dependent on the transmission coefficients and factors describing the coupling of the target, projectile, compound system, residual, and ejectile angular momenta. Compactly, for a γ transition between discrete levels with angular momenta $J_i \rightarrow J_f$ and a multipolarity L , the angular distribution is [76]

$$\phi(E_n, E_\gamma, \theta_\gamma) = \sum_{k=0}^{J_i} a_{2k}(E_n, L) P_{2k}(\cos \theta_\gamma) \quad (4.15)$$

For neutron emission where the residual nucleus is left in a discrete state (i.e. $E_{n'} = E_n - E_{ex}$), a similar equation is used with the coefficients α including a term dependent on the angular momentum carried by the emitted neutron rather than the multipolarity. For neutron emission where the residual nucleus is left in a state in the continuum, the angular distribution is isotropic in the center of mass frame. The energy spectrum follows a Maxwellian-like distribution based on the level density model used, see, e.g. [77, 78].

4.2 Reaction Modeling with TALYS

The design of TALYS is such that users have the ability to study the effect of modifying nuclear reaction model parameters on the resulting cross sections and secondary particle distributions. This is done through an input file that contains keywords and values for e.g. nOMP and level density parameters. The advantage of this approach is that experimental nuclear reaction physicists can adjust certain input parameters until the results of TALYS calculations match the experimental observations. The downsides are the vast number of parameters that can be adjusted and, depending on the amount and types of data TALYS is being compared against, the ability to make un-physical adjustments that push cross sections in a variety of other, non-observed, reaction channels into equally un-physical domains. Since TALYS is being used here as a generator of curves that can describe the gamma production and secondary neutron energy/angle distributions, pushing some parameters (e.g. the depth

of the imaginary part of the surface-central well, the width of the imaginary spin-orbit well, etc.) to unphysical values is allowed. However, the multichannel (discrete gamma production and elastic/inelastic secondary neutrons), multi-process (compound and direct) information from GENESIS being tested naturally imposes some constraints on the optimal parameter values.

In order to limit the number of TALYS keywords, p , used in the minimization, one-dimensional scans of all relevant keywords were done and χ^2 was calculated between experimental data products and those same data products calculated using the forward model and TALYS (see Chapter 5 for an explanation of the forward modeling). Relevant in this context means keywords that, based on the physics and the information present in the GENESIS data, will have an effect on χ^2 between experimental data products and those same data products calculated from TALYS. For example, level densities in fission fragments and parameters of the α -particle optical model potential are not relevant. The allowed range of values of each keyword was extracted from the TALYS manual and divided up into 50 equal spaced steps. For each of the keywords related to the neutron optical model and direct reactions, the χ^2 (Eq. 7.9) was computed for EJ-309 Detectors 8, 7, 6 (the locations of these detectors are listed in Appendix A), and the sum of detectors between 60° and 120° . The rest of the parameters were set to the default values using the keyword `best y`. The details of the construction of the experimental and simulated data products are given in Sec 7.1. If there was greater than 10% difference between the minimum and maximum values of the total χ^2 across the range scanned, the parameter was added to a set of mutable parameters in a corresponding JSON file for the full forward modeling 5.3. Figure 4.3 shows the χ^2 as a function of the TALYS keyword `avadjust n`, which modifies the diffuseness of the real volume-centered part of the nOMP, V_V . The list of parameters selected is given in Table 4.1. The percent difference is calculated between the minimum and maximum χ^2 across the keyword range.

Analyzing the results of the 1D scans with respect to the changes induced by the selected parameters in the cross sections and angular distributions is difficult, given the complicated nature of the problem. However, it is clear that the dominant contribution to the total nOMP, the real volume-centered term V_V , has a large effect on the direct cross sections and the χ^2 between the experimental and calculated data products. The primary effect of this is the increase of the elastic scattering channel. The 1D scans also show that the imaginary surface-central part of the total nOMP has a noticeable effect, as quantified by the changes in χ^2 , on the secondary neutron distributions. The imaginary potentials remove cross section from the direct cross sections and, given that the neutron data contains signal from both compound and direct, it follows that sensitivity to those parameters would be obtained.

A similar scan was performed for ratios of gamma ray yields using a different set of TALYS keywords. The details of the construction of the experimental and calculated yields, as well as the χ^2 used are given in Sec 8.1. The parameters that were included in the scan are those related to the level density model used (`ldmodel 1`, Gilbert and Cameron plus Fermi Gas), and those related to the gamma-strength function (`strength 9`, the Simplified Modified Lorentzian) [79]. The gamma-strength function describes the probability for an

Parameter	Initial Value	Range	Percent Difference	Description
avadjust n	1.0	[0.5,2.0]	80.6	multiplier to nOMP real volume-central well diffuseness
awdadjust n	1.0	[0.1,10.0]	15.4	multiplier to nOMP imaginary surface-central well diffuseness
d1adjust n	1.0	[0.2,5.0]	21.1	multiplier to parameter of energy-dependent imaginary surface-central well depth
d2adjust n	1.0	[0.2,5.0]	16.7	multiplier to parameter of energy-dependent imaginary surface-central well depth
d3adjust n	1.0	[0.2,5.0]	19.7	multiplier to parameter of energy-dependent imaginary surface-central well depth
elwidth	0.5	[1×10^{-6} 100.0]	80.1	width of elastic peak Gaussian smearing
rvadjust n	1.0	[0.5,2.0]	94.1	multiplier to width of nOMP real volume-central well
rvsoadjust n	1.0	[0.5,2.0]	14.1	multiplier to width of nOMP real spin-orbit well
rwdadjust n	1.0	[0.5,2.0]	94.2	multiplier to width of nOMP imaginary volume-central well
v1adjust	1.0	[0.2,5.0]	54.9	multiplier to parameter of energy-dependent real volume-central well depth
v2adjust	1.0	[0.2,5.0]	43.1	multiplier to parameter of energy-dependent real volume-central well depth
w2adjust	1.0	[0.2,5.0]	13.6	multiplier to parameter of energy-dependent imaginary volume-central well depth

Table 4.1: TALYS keywords used for secondary neutron energy/angle forward modeling

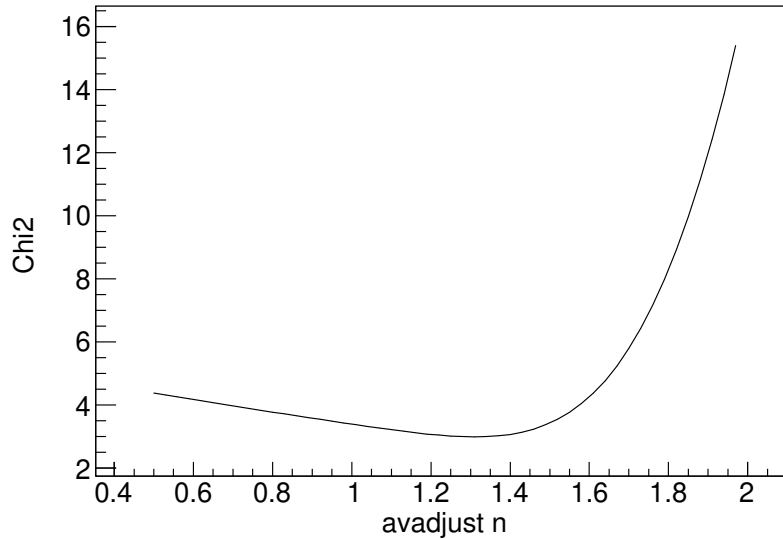


Figure 4.3: χ^2 between experimental and calculated Total-time-since-last-RF versus detector light yield for different values of the TALYS keyword `avadjust n`. The χ^2 is summed over detectors 8, 7, 6, and detector between $60^\circ - 120^\circ$.

excited nucleus to undergo specific gamma transitions, replacing the particle transmission coefficients $\tau_{\alpha\beta}$. The rest of the parameters were set to default values using the keyword `best y`. Figure 4.4 shows the change in the χ^2 as a function of the TALYS keyword `s2adjust 26 56` which multiplies the width of the spin distribution in the level density (Eqs. 4.12, 4.13) for the nucleus with $z = 26$ and $A = 56$. Table 4.2 lists the parameters that were selected for use in the full forward-model based extraction of gamma-ray production cross sections from GENESIS data.

This list can be refined by eliminating keywords that are dependent on the values of other keywords. The asymptotic value of the level density parameter \tilde{a} is obtained by excluding the shell-model based effects on the level density, and can be adjusted directly via `alimit 26 56` or by the keywords `alphald` and `betald`

$$\tilde{a} = \alpha_{ld}A + \beta_{ld}A^{2/3}, \quad (4.16)$$

where A is the mass number of the target nucleus.

The level density parameter a that can be adjusted by `aadjust 26 56` is a function of multiple keywords

$$a(E_x, \Delta, \gamma, \delta W, \tilde{a}) = \tilde{a} \left(1 + \delta W \frac{\exp(-\gamma U(E_x, \Delta))}{U(E_x, \Delta)} \right) \quad (4.17)$$

Parameter	Initial Value	Range	Percent Difference	Description
aadjust 26 56	1.0	[0.5,2.0]	0.51	multiplier to level density parameter
alimit 26 56	8.07484	[1.0,100.0]	80.9	asymptotic value of level density parameter
alphald	0.0693	[0.01,0.2]	41.4	constant in determination of global asymptotic level density parameter
betald	0.283	[-0.5,0.5]	30.7	constant in determination of global asymptotic level density parameter
deltaW 26 56	2.152	[-20.0,20.0]	41.9	correction of mass due to shell effects
Exmatchadjust 26 56	1.0	[0.1,10.0]	0.1	multiplier to matching energy
Kph	15	[1.0,100.]	14.9	value for single-particle level density in exciton model
pair 26 56	1.589	[0.0,10.0]	36.1	pairing energy correction
pairconstant	12.0	[0.0,30.0]	33.6	constant in determination of pairing energy
Pshiftadjust 26 56	0.0	[-10.0,10.0]	33.6	multiplier to pairing shift
s2adjust 26 56	1.0	[0.1,10.0]	64.1	multiplier to spin cutoff
Tadjust 26 56	1.0	[0.1,10.0]	34.9	multiplier to temperature energy to stop width fluctuation corrections
widthfluc	S_n^a	[0.0,20.0]	9.3	

^a $S_n(^{56}\text{Fe}) = 11.197$ MeV

Table 4.2: TALYS keywords for gamma ray production forward modeling

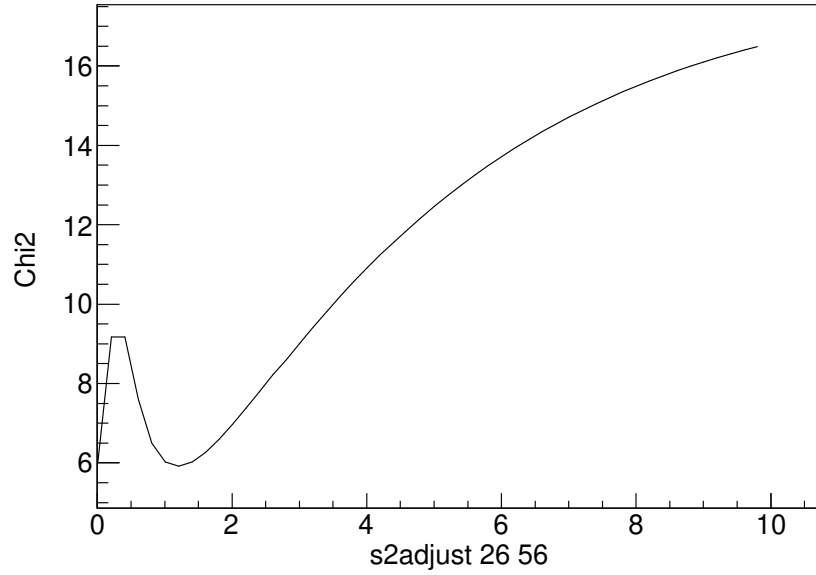


Figure 4.4: χ^2 between experimental and calculated Time-since-last-RF versus gamma yield for different values of the TALYS keyword `s2adjust 26 56`. The χ^2 is given in Eq. 8.7.

as is the width of the spin distribution for the Fermi Gas model

$$\sigma_F^2(E_x, \Delta, \tilde{a}, a, \text{s2adjust}) = \text{s2adjust} \left(0.01389 \frac{A^{5/3}}{\tilde{a}} \sqrt{aU(E_x, \Delta)} \right) \quad (4.18)$$

This means that doubling \tilde{a} will result in a factor of $\sqrt{2}$ reduction in the width of the spin distribution at S_n .

$$\sigma(S_n, 2\tilde{a}_0) = \frac{1}{2^{1/4}} \sigma(S_n, \tilde{a}_0) \quad (4.19)$$

However, if the keyword `s2adjust 26 56` is set at some point later in the input file, the width of the spin distribution at S_n will be

$$\sigma(S_n, 2\tilde{a}_0) = \text{s2adjust} \frac{1}{2^{1/4}} \sigma(S_n, \tilde{a}_0) \quad (4.20)$$

The pairing constant Δ , for an even-even nucleus like ^{56}Fe , can be adjusted using directly the keyword `pair 26 56` or indirectly using the keywords `pairconstant` and `Pshiftadjust 26 56`.

$$\Delta = \frac{2}{\sqrt{A}} \text{pairconstant} + \text{Pshitadjust} \times P_{\text{shift}} \quad (4.21)$$

The temperature T that enters into Eq. 4.12 is also dependent on other keywords through the equation

$$T = \text{Tadjust} \left(\frac{d \ln(\rho_{\text{Fermi}})}{dE_x}(E_m) \right)^{-1} \quad (4.22)$$

As a result of these dependencies and the multiple accessors to single parameters, the keywords ultimately used in the minimization are `s2adjust`, `alimit`, `Pshiftadjust` and `Tadjust`.

Chapter 5

Measuring Reaction Cross Sections with GENESIS

This chapter will outline the methods used to extract cross sections and secondary particle distributions from GENESIS data. Two methods are outlined, both containing certain strengths, degrees of complexity, and weaknesses, arising from certain challenges and limitations associated with the experimental setup and the nucleus under investigation. The end goal is to utilize both methods in the domains where they each are valid and for the domains where their applicability overlaps, to evaluate agreement.

5.1 Traditional Approach

The conventional method to experimentally determine the cross section of a nuclear reaction is to bombard a thin piece of material with a beam of projectiles, observe some product of the reaction of interest, and from the number of observed radiations, the number of projectiles that were incident on the target, and the number of target atoms in the area of the beam, calculate the cross section. If Y is the number of reactions that occurred, $\phi(E)$ is the incident particle flux, and $(\rho R)_{target}$ is the areal number density of the target, the cross section can be calculated as

$$\sigma(E) = \frac{Y}{\phi(E)(\rho R)_{target}} . \quad (5.1)$$

The number of reactions can be calculated from the number of observed reaction products $Y_{observed}$, the efficiency of the detector ϵ , and the amount of background signal in the observed yield $Y_{background}$. Taking these into consideration,

$$\sigma(E) = \frac{Y_{observed} - Y_{background}}{\epsilon\phi(E)(\rho R)_{target}} . \quad (5.2)$$

The uncertainty on the cross section is the quadrature sum of the relative uncertainties:

$$\sigma_{\sigma}^2(E) = \sigma(E) \sqrt{\left(\frac{\sigma_{Y_{obs}}}{Y_{obs}}\right)^2 + \left(\frac{\sigma_{Y_{bkg}}}{Y_{bkg}}\right)^2 + \left(\frac{\sigma_{\epsilon}}{\epsilon}\right)^2 + \left(\frac{\sigma_{\phi(E)}}{\phi(E)}\right)^2 + \left(\frac{\sigma_{\rho R}}{\rho R}\right)^2} \quad (5.3)$$

Limitations

In order to determine the cross section at a given incident neutron energy, the Time-since-last-RF of the neutron associated with the observed γ yields is used. The RF period for 14 MeV deuterons at the 88 Inch Cyclotron (5.907 MHz) and the flight path from the break-up target to the scattering target (7.365 m) is such that neutrons of different energies, from consecutive deuteron bunches, can induce reactions at the same time, a phenomenon known as frame overlap. The neutron TOF measured by taking the difference of the reaction time, deduced from the flight path and interaction time of a γ -ray in an HPGe detector, and a timing signal from the cyclotron RF will thus differ from the actual neutron TOF by n RF periods (T_{RF})

$$\text{Time since last RF} = \text{TOF} - nT_{RF}$$

Therefore, unless solutions giving rise to slower neutrons can be excluded due to the threshold of a given reaction, the neutron energy cannot be determined unambiguously and the conventional analysis technique cannot be used.

Figure 5.1 shows a partial level spin J versus level energy E_{ex} diagram for ^{56}Fe and the γ transitions connecting the levels. The transitions that were observed in sufficient quantity to be further analyzed are indicated with blue or red lines. Every γ -ray coming from the second excited state ($E_{ex} = 2085.1$ keV) and above has regions of Time-since-last-RF space that are uniquely associated with a single neutron energy, or have $\geq 95\%$ of the neutrons coming from a single beam pulse. The cross sections for these reactions in those energy ranges can be determined using the conventional technique.

5.2 Forward Modeling

In order to overcome the limitations of the conventional approach and determine the production cross section for the 846.7 keV γ and the secondary neutron energy/angle distributions, a forward modeling analysis framework was developed. This section will describe the general theory of the method and its implementation to analyze GENESIS data.

Let S be a function describing the distribution of particles emitted following a neutron interaction on a nucleus of interest, parameterized by a set of variables $\vec{\beta}$ (e.g. $\vec{\beta} = (E_n, E_{n'}, \Omega_{n'})$). Let Y be some experimentally observed data product, described by a set of parameters $\vec{\beta}'$ (e.g. $\vec{\beta}' = (\text{light yield}, \text{TOF}, \theta_{\text{detector}})$). If the response function \mathcal{R} , that maps the source parameters $\vec{\beta}$ into the observed parameters $\vec{\beta}'$, is known, the observed yield can

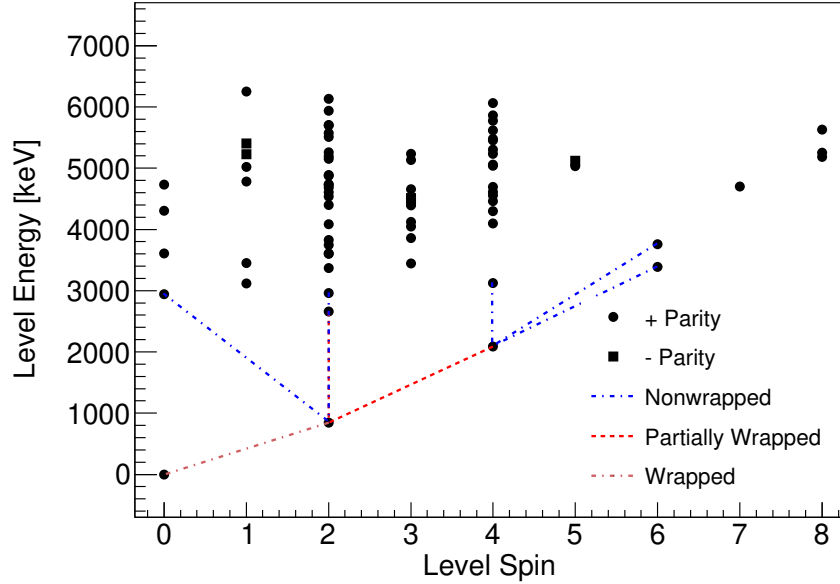


Figure 5.1: Level total spin J versus level excitation energy E_{ex} for ^{56}Fe based on RIPL3 [80]. The observed γ -transitions that do not suffer from neutron frame overlap are indicated by a blue dot-long-dashed line. The observed transitions that suffer partially from frame overlap (i.e. those that contain some regions of Time-since-last-RF that can be uniquely attributed to a single neutron energy) are indicated by a red dashed line. The 846.8 keV $2_0^+ \rightarrow 0_0^+$ is fully wrapped.

by calculated by

$$Y(\vec{\beta}') = \int \mathcal{R}(\vec{\beta} \rightarrow \vec{\beta}') S(\vec{\beta}) d\vec{\beta}. \quad (5.4)$$

This approach is a generalization of the traditional method outlined above, with S corresponding to the cross section σ and \mathcal{R} corresponding to the product of detector efficiency and flux, $\epsilon\phi(E)$. In GENESIS experiments, Y and \mathcal{R} are not defined continuously, so a discrete form of Eq. 5.4 is needed. Writing Y , \mathcal{R} and S as matrices, the experimental data product can be computed as a matrix multiplication,

$$\mathbf{Y}(\vec{\beta}') = \mathcal{R}(\vec{\beta} \rightarrow \vec{\beta}') \mathbf{S}(\vec{\beta}). \quad (5.5)$$

If the response matrix is invertible, the source distribution can be directly calculated from the experimental observation.

The response matrices relevant for GENESIS data are rank-deficient and therefore non-invertible. Instead, an objective function has been defined to describe the difference between the observed data product and one calculated using Eq. 5.5 and a minimization algorithm employed to find an optimal S such that calculated and experimental yields agree. The details of the objective function and the minimization routine will be detailed in Section 5.3.

The source term S is the reaction cross section. For γ -ray data, these are the neutron energy differential gamma ray production cross sections, $\sigma(E_n, E_\gamma)$. For neutrons, these are total incident neutron energy differential scattered neutron energy/angle cross sections, $\sigma(E_n, E_{n'}, \Omega_{n'})$. The response function \mathcal{R} can be broken down into two components, one that maps neutron energy into the experimental time domain and calculates the number of reactions occurring in the target and one that maps the reaction product yields into detector-derived quantities.

Flux Matrix

The first component of the response function \mathcal{R} is a mapping of neutron energy to Time-since-last-RF via a 2-dimensional matrix. For n Time-since-last-RF bins and m neutron energy bins, the flux matrix F can be written as

$$F = \begin{pmatrix} \phi(E_0, T_0) & \phi(E_1, T_0) & \dots & \phi(E_m, T_0) \\ \phi(E_0, T_1) & \phi(E_1, T_1) & & \vdots \\ & & \ddots & \\ \phi(E_0, T_n) & \dots & & \phi(E_m, T_n) \end{pmatrix} \quad (5.6)$$

where $\phi(E_i, T_j)$ is the number of neutrons at energy E_i and Time-since-last-RF T_j . The number of neutrons in each element of F is taken from the spectrum measured by the sToF detector (Fig. 2.1). To construct the matrix, the size of the Time-since-last-RF bin is selected based on the timing resolution of the detector for the data product under investigation and the resulting counting statistics. Then, the sToF spectrum is re-binned based on the desired time structure and the matrix is filled based on the known energy and calculated Time-since-last-RF. The time resolution of the system, from the gamma or neutron detectors and the width of the deuteron pulse, is then added to the flux matrix via a convolution. The time resolution of the detectors can be represented as a Gaussian with a width deduced from the $\gamma\gamma$ measurements (Sec. 3.1). The time spread of the deuteron beam, i.e. the uncertainty on the neutron creation time, can be represented as Gaussian with a width deduced from the γ flash, as seen by the sToF detector, or that γ flash time distribution can be used if the distribution is non-Gaussian. This is done by building a unit-normalized probability density function (PDF) of the γ flash, rebinning that PDF into the desired Time-since-last-RF space, and subtracting the average value of the background outside the peak. Figure 5.2 shows this PDF. The γ flash PDF and the Gaussian defined by the detector resolution are then convolved with the raw flux matrix to generate the final flux matrix for this experiment, shown in Figure 5.3. Each element corresponds to an 8.068 ns window in either Time-since-last-RF or actual neutron TOF space. A similar matrix V_F is constructed where each element corresponds to the uncertainty in the flux from sToF. The uncertainty on the original sToF measurement is also convolved with the detector timing resolution and the γ flash PDF.

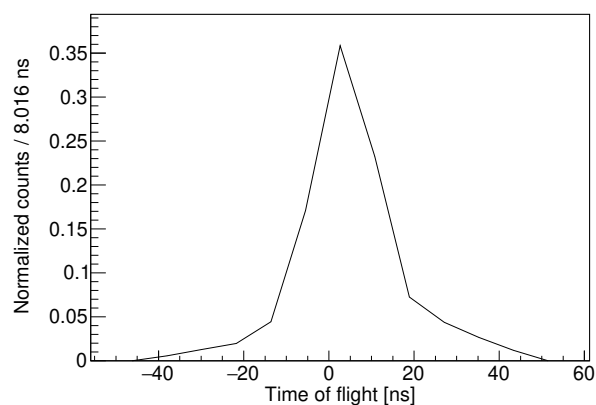


Figure 5.2: PDF of the γ flash seen by the reference EJ-309 Detector 4.

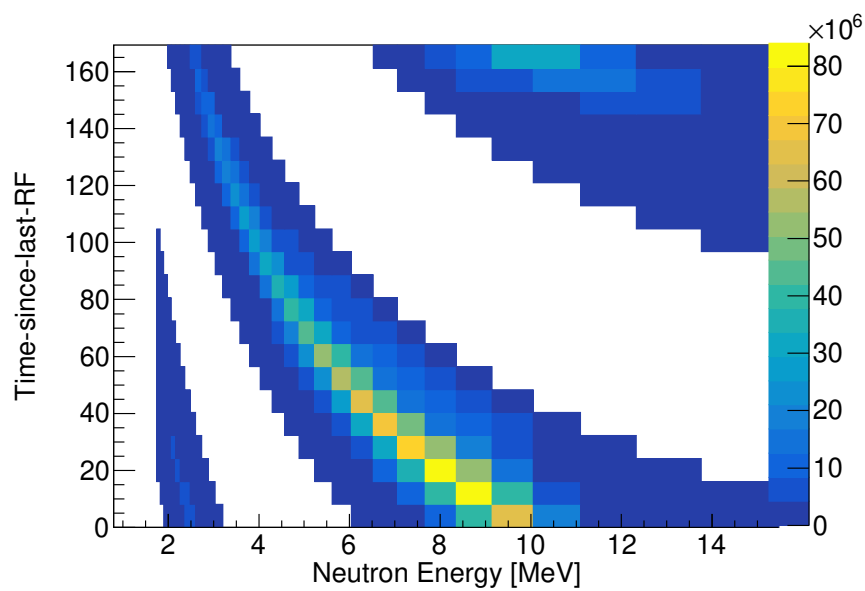


Figure 5.3: Visual representation of the neutron flux matrix for 14 MeV TTDB on Carbon over a flight path of 7.365 m, plotted as incident neutron energy versus Time-since-last-RF. Each bin is 8.068 ns wide.

The multiplication of F by the source term S yields the distribution of particles at the ^{56}Fe target, Y_0 .

$$Y_0(\text{TOF}) = FS \quad (5.7)$$

The variance on the calculated yield at a given Time-since-last-RF, $Y_0(TOF_t)$, is

$$Var(Y_0(TOF_t)) = \sum_{i=0}^m V_F(E_i, TOF_t) (S(E_i))^2 \quad (5.8)$$

Figure 5.4 shows an example of this multiplication with the production cross section for the 846.8 keV γ -ray ($E_{thresh} = 861.9$ keV) from a calculation with TALYS1.96 [68] using the keyword `best y` [72]. The total yield as a function of Time-since-last-RF is shown in

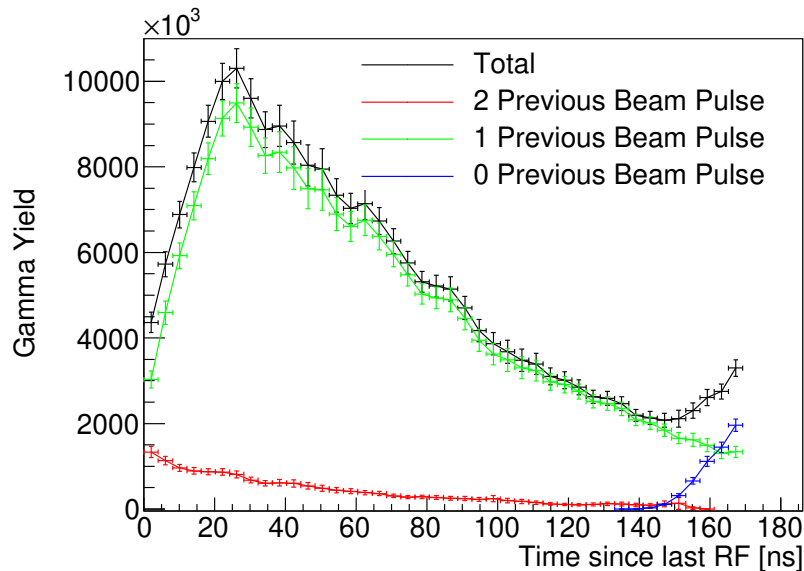


Figure 5.4: The yield of the 846.8 keV γ -ray versus Time-since-last-RF calculated using a cross section from TALYS1.96 and the flux matrix of Fig. 5.3. The black points are the total yield, the contributions from the different beam pulses are shown in color. The dominant contribution across most of the Time-since-last-RF domain is from the second most recent beam pulse.

addition to the yield contributed by the most recent and previous deuteron beam pulses. The dominant contribution to the yield comes from the first most recent beam pulse (i.e. neutrons with a TOF between 1 and 2 RF periods) but throughout the entire domain, neutrons from the other two wraps also contribute. The contribution from these other pulses makes a calculation of the cross section from this yield not possible with the traditional analysis approach. Figure 5.5 shows the yield for 1037.8 keV γ -ray ($E_{thresh} = 3178.8$ keV), with a production cross section taken from the same TALYS calculation as the cross section used for Figure 5.4. Unlike the 846.87 keV yield, the neutrons from the 2nd previous beam pulse are below the reaction threshold and do not contribute to the total yield. Additionally, the neutrons from the 1st previous beam pulse whose Time-since-last-RF is the same as the

fast neutrons from the most recent beam pulse, are also below threshold. In every single Time-since-last-RF bin, only a single deuteron pulse is contributing to the total yield and the neutron energy can therefore be unambiguously determined.

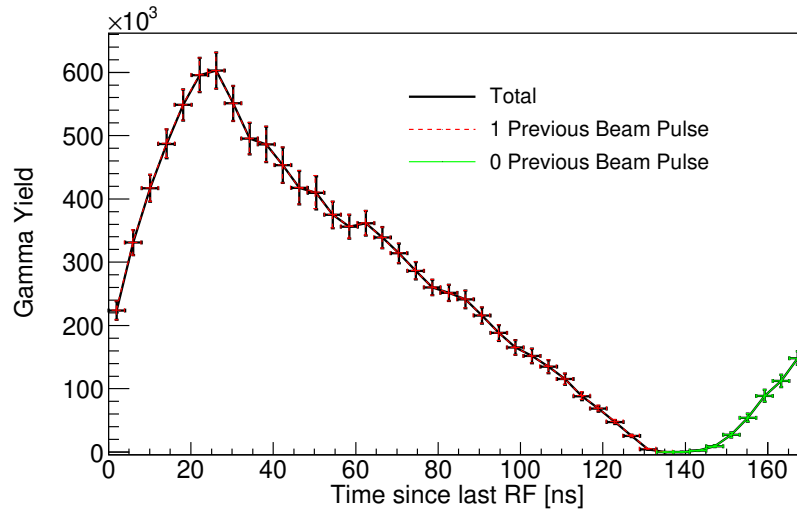


Figure 5.5: The yield of the 1037.8 keV γ versus time since last RF, calculated using the cross section from TALYS1.96 and the flux matrix of Fig. 5.3. The total yield is shown in black and the contributions from different beam pulses are shown in color. Across the entire Time-since-last-RF domain, only one beam pulse is constituting the entire yield.

Figure 5.6 shows the result of the convolution of the flux matrix with the $0^\circ - 2^\circ$ secondary neutron energy distribution calculated using TALYS1.96 with the keyword `best y`. The flux matrix used in this convolution has TOF bins equivalent to the resolution of the organic liquid scintillator detectors, 0.35 ns. The result of the convolution was rescaled to have 1 ns Time-since-last-RF bins. The calculation was run with the keyword `elwidth 0.1`, which broadens the energy distributions from elastic scattering and inelastic scattering to discrete levels by a Gaussian with $\sigma = 0.1$ MeV. The dominant feature is the wrapped, broadened elastic scattering and inelastic scattering to the first excited state ($E^* = 846.8$ keV).

Detector Response Functions

The second component of the response function \mathcal{R} maps the flux-matrix convolved source term to measured signals in the detectors. This map includes the transport and scattering of γ -rays or neutrons as they travel from the scattering target to the detector and the intrinsic detector efficiencies.

For gamma ray production, the efficiency is an energy dependent scalar, taken from the validated GEANT4 model (Sec. 3.3). The calculations were done with γ 's launched from the ^{56}Fe target, as it was hung during the experiment, and the processing was performed as

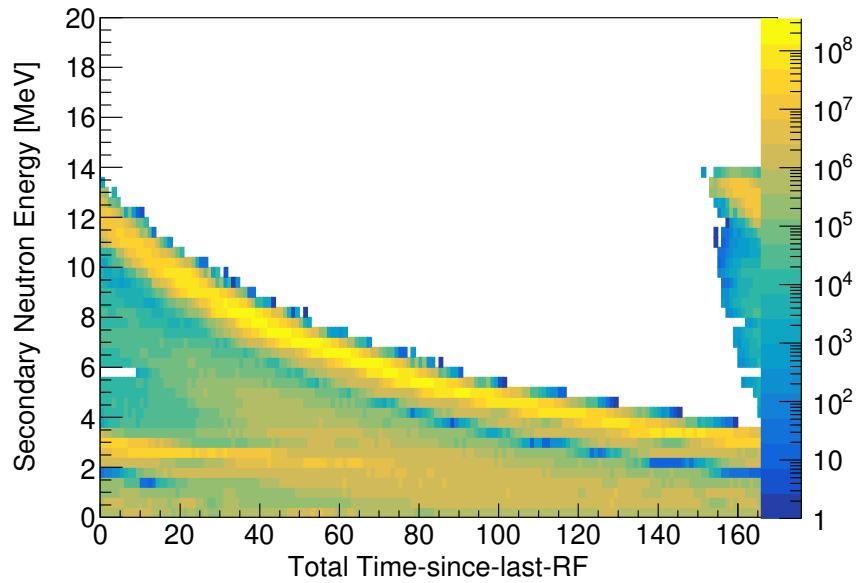


Figure 5.6: Secondary neutron energy distribution at $0^\circ - 2^\circ$ from a TALYS1.96 calculation convolved with the flux matrix.

Detector	A_0	A_1	A_2	A_3	A_4
Clover 0 Leaf 1	-3.987×10^{-4}	-2.679	0.9606	-0.03082	2.929×10^{-3}
Clover 0 Leaf 2	-1.195×10^{-4}	-1.494	0.5052	-0.01400	1.232×10^{-3}
Clover 0 Leaf 3	-1.035×10^{-4}	-1.517	0.5106	-0.01405	1.224×10^{-3}
Clover 0 Leaf 4	-1.891×10^{-4}	-1.848	0.6449	-0.01923	1.749×10^{-3}
Clover 0 Total	-1.942×10^{-4}	-1.548	0.5197	-0.01328	1.270×10^{-3}
Clover 1 Leaf 1	2.274×10^{-4}	0.4029	-0.1915	9.540×10^{-3}	-1.059×10^{-3}
Clover 1 Leaf 2	7.086×10^{-5}	-0.2574	0.05802	4.540×10^{-4}	-1.423×10^{-4}
Clover 1 Leaf 3	9.066×10^{-5}	-0.2678	0.05983	6.734×10^{-4}	-1.837×10^{-4}
Clover 1 Leaf 4	7.163×10^{-5}	-0.2547	0.05721	4.732×10^{-4}	-1.445×10^{-4}
Clover 1 Total	-1.054×10^{-4}	-1.225	0.3701	-8.110×10^{-3}	7.307×10^{-4}

Table 5.1: HPGe detector efficiencies, parameterized using the Debertin fit function.

described in Section 3.3. The calculated efficiencies for the individual CLOVER leafs and each CLOVER operating in total detector mode were fit to the Debertin function [62]. The fit parameters are reported in Table 5.1. The correlation matrix for the fit parameters for CLOVER 0, Leaf 1 is shown in Figure 5.7.

The response functions for the EJ-309 detectors were calculated using the benchmarked GEANT4 model of the array (see Section 3.3 for details on the model and benchmarking).

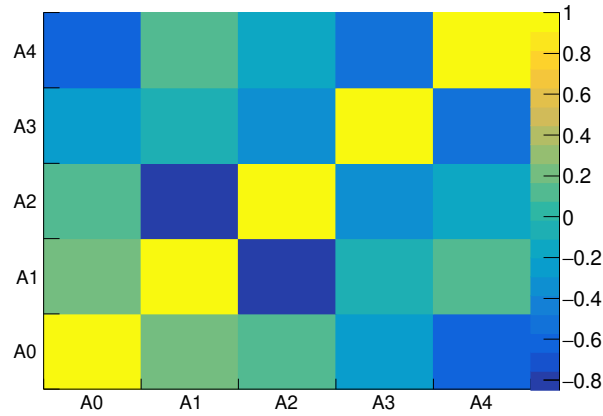


Figure 5.7: Correlation matrix for the parameters of the Debertin fit function from a fit to GEANT4 calculated efficiency for a single CLOVER leaf.

The response functions were calculated using an isotropic neutron source launched from a geometry equivalent to the ^{56}Fe scattering target and a uniform energy distribution from 0 to 20 MeV and processed as described in Sec. 3.2, including the convolution of the measured detector resolution and the propagation of the uncertainties from detector resolution and gain fitting procedure. For each organic scintillator, a 2D matrix R that maps the source neutron energy (discretized into n homoscedastic bins) and initial angle (relative to the neutron beam axis in m , 2° bins) into light yield in each detector (in l bins) was built.

$$R^T = \begin{pmatrix} R(E_0, \theta_0, L_0) & R(E_0, \theta_0, L_1) & \dots & R(E_0, \theta_0, L_l) \\ R(E_1, \theta_0, L_0) & R(E_1, \theta_0, L_1) & & \vdots \\ \vdots & & & \\ R(E_n, \theta_0, L_0) & & & \\ R(E_0, \theta_1, L_0) & & & \\ \vdots & & \ddots & \\ R(E_n, \theta_m, L_0) & \dots & & R(E_n, \theta_m, L_l) \end{pmatrix} \quad (5.9)$$

The matrix is scaled by the number of source neutrons in the GEANT4 calculation so that it represents the absolute efficiency of the detector. A visual representation of the non-scaled matrix R is shown in Figure 5.8 for EJ-309 detector 8, located at 13.1° relative to the neutron beam and 70.0 cm from the center of the ^{56}Fe target. Four projections are shown corresponding to different initial neutron angles. The uncertainty on the response function R includes TOF from detector location, light yield and threshold from the gain calibration procedure.

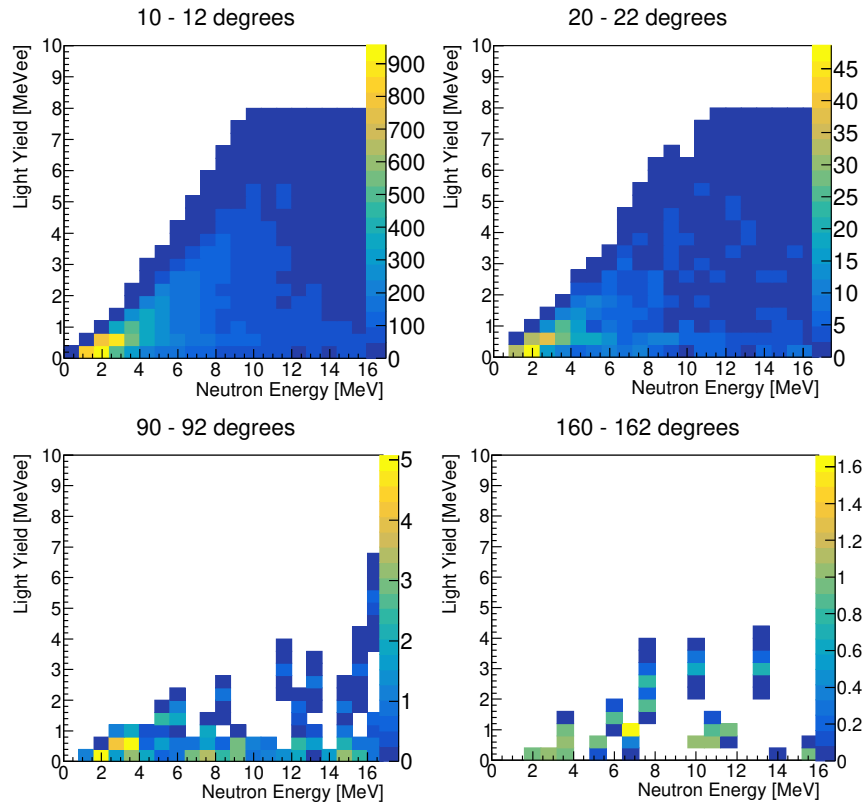


Figure 5.8: Slices of the neutron response function R showing neutron energy versus light yield at four different initial neutron angles for a single neutron detector (Detector 8, 13°). The scale represents the number of neutrons reaching the detector normalized by the number of source neutrons used in the calculation (2×10^9). The primary efficiency is from neutrons with initial angles in a narrow range around the detector angle.

5.3 Source Term Modeling with TALYS

Given the complicated nature of the energy dependent gamma-ray production cross sections and scattered neutron energy-angle distributions, no single function (e.g. a n^{th} order polynomial, a logistic function, a skewed Gaussian, etc.) can be used to parameterize the source term S . Additionally, the cross sections for the various possible reaction channels at a given neutron energy are not independent of each other and the values deduced from the observation of either secondary neutrons or gamma-rays must agree. To satisfy these constraints, the nuclear reaction code TALYS [68] has been used to generate cross sections that act as source terms for the forward model.

A C++/ROOT based class was developed so that TALYS outputs can be easily compared to GENESIS data and so that the minimization algorithms included with ROOT can write TALYS input decks, process TALYS outputs, and adjust parameters until an agree-

Parameter	Value	Output
<code>ejectiles</code>	<code>g n</code>	Distributions for only γ 's and neutrons
<code>outgamdis</code>	<code>y</code>	Discrete γ production
<code>ddxmode</code>	<code>3</code>	Secondary energy and angle
<code>outangle</code>	<code>y</code>	Angular distribution following scattering to discrete states
<code>outdiscrete</code>	<code>y</code>	Cross section for scattering to discrete states

Table 5.2: TALYS outputs used by default

ment between the data and the calculation is reached. ROOT is C++ framework for data processing and analysis, file input/output, efficient containers for organizing data, data visualization and statistical analyses that is widely used in physics research[81]. The class is oriented around a single isotope, the one from which the GENESIS data were derived, that constitutes the “target” for TALYS calculations and a set of neutron energies at which the cross sections are calculated. A set of “basic” parameters are passed to the class via a JSON file and stored with the class. These parameters are those which are immutable in the sense that any kind of minimization algorithm will not consider them in the search. Examples of basic parameters are the level density model, the number of discrete states in the target and residual nuclei, the maximum number of protons away from the target nuclei a residual nucleus can have in order to be considered, and whether the direct reaction code ECIS06 is called. A set of “advanced” parameters are also read in via a JSON and stored with the class. These are the parameters that are mutable and include optical model widths, depths, and coupling strengths, and parameters for the level density of the chosen model (e.g. spin cutoff, matching energy, temperature, etc.). Included in the JSON file are initial values and the limits for these parameters. Based on these immutable and mutable parameters, the class can generate new TALYS input decks and perform a calculation with that input deck. By default, the new input decks specify certain outputs which are given in Table 5.2. The output file containing the information requested by the parameters in Table 5.2 is processed and stored so that the results can be visualized or processed into matrices or vectors for further calculations in the forward modeling matrix convolutions.

The ROOT API to Minuit2 [82], a gradient descent algorithm, was used to minimize the objective functions between the TALYS calculated and experimental GENESIS data products. At each step, the minimization routine writes a new TALYS input deck based on the current values of the parameters specified in the JSON file and runs a TALYS calculation using that new input deck. The output of the calculation is processed and new calculated data products are generated. The specific objective functions will be given in the discussions of the analysis of the experimental data and the construction of the relevant data products (Section 7.1 for secondary neutron energy/angle distributions and Section 8.1 for gamma ray production). In general, the objective function is a χ^2 with model and experimental

uncertainties for a calculated data product Y^{calc} parameterized by p parameters β_0, \dots, β_p :

$$\chi^2 = \sum_i^n \frac{(Y_i^{calc}(\beta_0, \dots, \beta_p) - Y_i^{obs})^2}{(\sigma_i^{calc})^2 + (\sigma_i^{obs})^2} \quad (5.10)$$

The uncertainties on the values of the parameters at the minimum, $\hat{\beta}$, are derived from the matrix of second derivatives of the objective function and are proportional to the quadrature sum of the model experimental uncertainties [83]. The uncertainty for a given parameter β_i is defined as the distance from the minimum, along the trajectory $\hat{\beta}_{j \neq i}$, required for the relative χ^2 to change by 1 [83].

The full forward modeling analysis procedure is shown in Figure 5.9 There are three

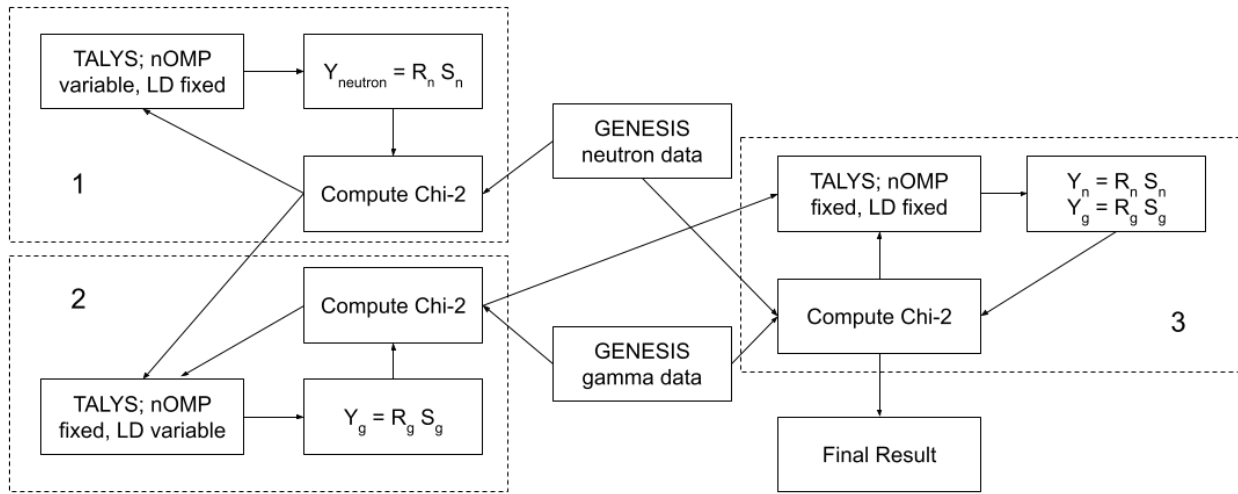


Figure 5.9: Flow chart showing the forward modeling analysis. First (Loop 1), the nOMP parameters (Table 4.1) are optimized on the neutron data with the rest of the parameters fixed at default values with keyword `best y`. The parameters in Table 4.2 are optimized in Loop 2 on the γ -ray data, with nOMP parameters from the neutron optimization. The final χ^2 (Loop 3) is calculated against the neutron and gamma data and the uncertainty on the optimal parameters is found.

different minimization loops. The first loop is centered around the neutron data to find the optimal values for nOMP keywords in Table 4.1. The rest of the parameters are fixed to their default values using the keyword `best y`. Once optimal parameters are found, the optimal values for the keywords in Table 4.2 are found by comparing against the γ -ray production data, with the nOMP values fixed at the results of the first loop. At the conclusion of this second loop, a third loop is entered, the purpose of which is to calculate the uncertainty on the optimal parameters from both loops by comparing the results of the TALYS calculations with the optimal parameters against the neutron and gamma data simultaneously. This

third loop consists of calculating the Hessian matrix from which the covariance matrix can be calculated. The end result is a set of γ -ray production cross sections and secondary neutron energy/angle distributions with uncertainties.

Chapter 6

^{56}Fe Experimental Campaign

The ^{56}Fe experimental campaign was conducted in late June / early July 2021. The neutron beam was produced via 14 MeV TTDB on a carbon target. The RF period for the 14 MeV deuteron beam was 169.2563 ns. The ^{56}Fe target described below was placed 736.5 cm from the break-up target and was hung 50.3° relative to the neutron beam. The solid angle subtended by the target was 3.67×10^{-5} sr and the areal density was 5.283×10^{21} g cm^{-2} . In addition to the ^{56}Fe measurements, three other kinds of target were hung in the middle of the frame. A 0.723 ± 0.009 cm thick, 5.03×6.36 cm Be target was used to investigate the amount of γ contamination from the 847.15 keV transition in ^{76}Ge , and inelastic scattering from the 1039.506 keV level in ^{70}Ge . Data were collected with no target present, “Blank”, to determine the neutron background from the beam scattering on air. A collection of activation foils was also fielded to find the absolute number of neutrons for the normalization of the spectrum measured by sToF. The total charge for the four different target configurations are reported in Table 6.1. The following sections detail the characterization of the ^{56}Fe scattering

Target	Total Charge [μC]	Average Current [μA]
^{56}Fe	2148480	8.816
Be	216802	9.014
Blank	155440	9.54
Activation	66427	9.14

Table 6.1: Total deuteron beam charge and average beam current for the three different target configurations.

target, issues with the data acquisition system encountered during the experiment, and the extraction of an absolute normalization of the sToF-measured TTDB neutron flux from the activation foil data.

6.1 Target Characterization

The target used in the measurement of the $^{56}\text{Fe}(n, n'\gamma)$ reaction was purchased from the National Isotope Development Center at Oak Ridge National Laboratory [84]. It was enriched to $99.98 \pm 0.02\%$ in ^{56}Fe and originally 10.0 g in the form of iron oxide. The iron oxide powder was processed into an elliptical disk of iron metal with a major radius of 3.6 cm and minor radius of 1.75 cm and a mass of $9.7653 \pm 1 \times 10^{-4}$ g. The thickness of the target was measured using a calibrated HPGe detector and an ^{241}Am point source. The source was moved around the area of the target in 1 cm steps and counted for five minutes at each location. Data were also taken with the Fe target removed. The observed count rate for the no-target measurement is

$$R_0 = \epsilon_\gamma A_0 \quad (6.1)$$

where ϵ_γ is the efficiency of the detector at 59.5409 keV and A_0 is the activity of the source. The observed count rate for some position with the Fe target in place is

$$R_i = \epsilon_\gamma A_0 e^{-(\mu/\rho)\rho\Delta X} = R_0 e^{-(\mu/\rho)\rho\Delta X_i} \quad (6.2)$$

where $\mu/\rho = 1.2396 \text{ cm}^2/\text{g}$ is the mass attenuation coefficient for iron at 59.5409 keV [85], $\rho = 7.874 \text{ g/cm}^3$ is the density of iron, and ΔX_i is the thickness of the target at location i . The thickness can be calculated by solving the above equation.

$$\Delta X_i = \frac{-\log(R_i/R_0)}{(\mu/\rho)\rho} \quad (6.3)$$

Taking the the attenuation coefficient and density as absolutely known, the uncertainty in the thickness is

$$\sigma_{\Delta X_i}^2 = ((\mu/\rho)\rho)^{-2} \left(\frac{\sigma_{R_i}^2}{R_i^2} + \frac{\sigma_{R_0}^2}{R_0^2} \right). \quad (6.4)$$

Figure 6.1 shows the thickness versus the $X - Y$ coordinates used in the measurement, which correspond to a distance of 0.5 cm. The average thickness is 0.603 ± 0.042 mm.

The thickness of the target was chosen to minimize the probability for multiple reactions to occur. The multiple scatter probability was calculated using forced collision Monte Carlo with the ENDF/B-VIII.0 ACE library [86]. The initial neutron energy E_0 was sampled from a uniform distribution between 0.5 and 20 MeV. The initial location (x_0, y_0) of the neutron relative to the center of the target was randomly sampled. Included in this selection of initial position is the assumption that the neutron beam fills or overfills the target and is uniform in intensity across the target. The initial z location of the target was sampled according to the macroscopic cross section $\Sigma(E_0)$ [87]

$$z_0 = \begin{cases} -\Sigma^{-1} \log(\xi), & \Sigma^{-1} \leq \Delta X \\ -\Sigma^{-1} \log(1 - \xi(1 - e^{-\Sigma\Delta X})), & \Sigma^{-1} > \Delta X \end{cases} \quad (6.5)$$

where $\xi \sim \text{U}(0, 1)$ and ΔX is the average thickness of the target determined above. The reaction channel was then sampled and all neutron producing reactions were considered. The

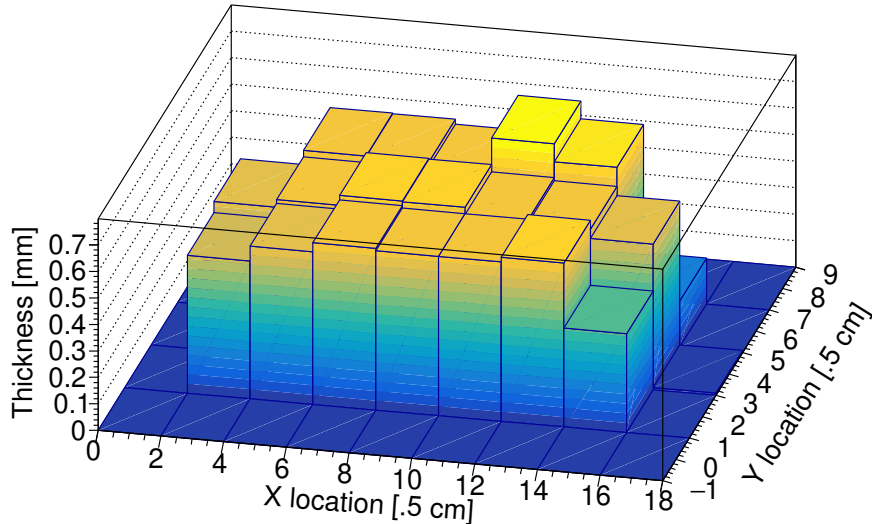


Figure 6.1: Map of the thickness of the ^{56}Fe target determined using an ^{241}Am point source. The x and y axes represent the 0.5 cm grid the target and source were placed on. The average thickness is 0.603 ± 0.042 mm.

macroscopic cross section at the energy of the secondary neutron, $\Sigma(E_{n'})$, was then computed. To account for the angle of the target relative to the neutron beam in the GENESIS frame, the outgoing polar angle of the particle was rotated 50.3° . The azimuthal angle of each outgoing neutron was assumed to be isotropically distributed. For each azimuthal angle from $0^\circ - 360^\circ$ in 2° steps, the distance from the interaction location (x_0, y_0, z_0) to the surface of the iron target D was compared to the mean free path $\lambda = \Sigma^{-1}$ of the secondary neutron. If $D > \lambda$, the particle was classified as a multiple scatter event with a weight of $1/180$. The calculation was done for 10^7 source neutrons. The multiple scatter events were histogrammed and then weighted by the number of source neutrons in each energy bin. Figure 6.2 shows the multiple scatter probability versus neutron energy for neutrons with energies between 0.5 and 20.0 MeV. The flux-weighted multiple scatter probability for a 14 MeV TTDB neutron beam on the ^{56}Fe target described above is $2.235 \pm 0.007\%$.

6.2 Data Acquisition Issues

The data acquisition (DAQ) was stopped and started every hour to keep the raw data files around 20 GB. It was observed that every time the DAQ was restarted, the ADC spectrum from the detectors on the second Mesytec board configured with the QDC firmware changed. Figure 6.3 shows the raw ADC spectrum as a function of experiment time for one of the detectors on the defective board. The exact cause of the issue is unknown, but the firmware

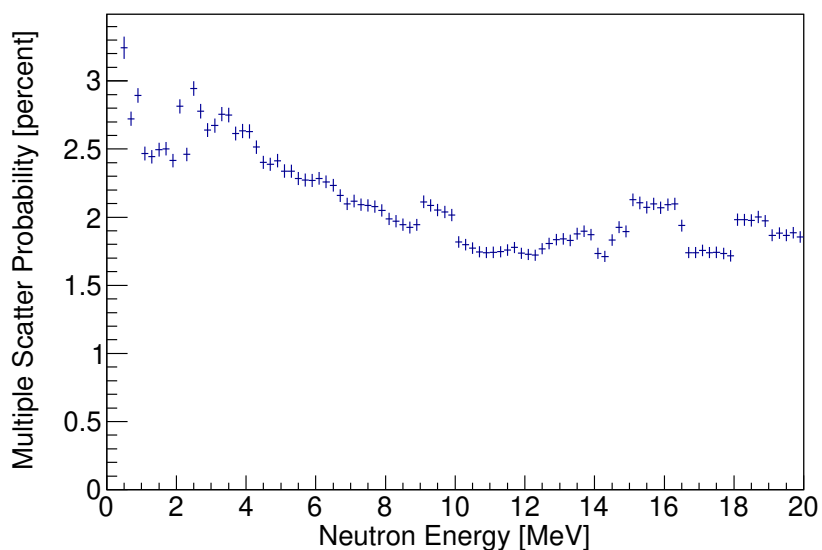


Figure 6.2: The probability for a neutron to undergo more than one reaction within the ^{56}Fe target as a function of the initial neutron energy. The probabilities were calculated using forced collision Monte Carlo.

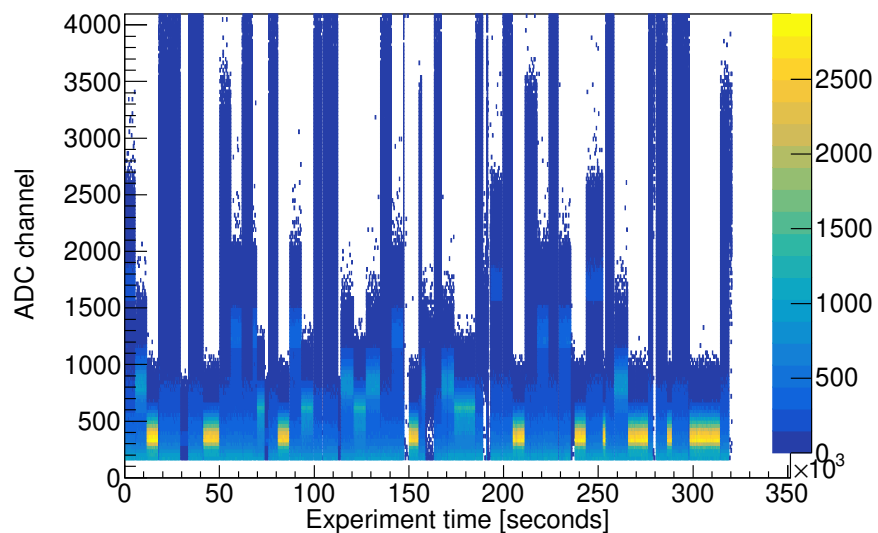


Figure 6.3: ADC spectra versus experiment time for a single EJ-309 detector (Detector 22) on the second Mesytex MDPP16 board with the QDC firmware. All the detectors on this board had similar distortions of the ADC spectrum each time the DAQ was stopped and started for a new file.

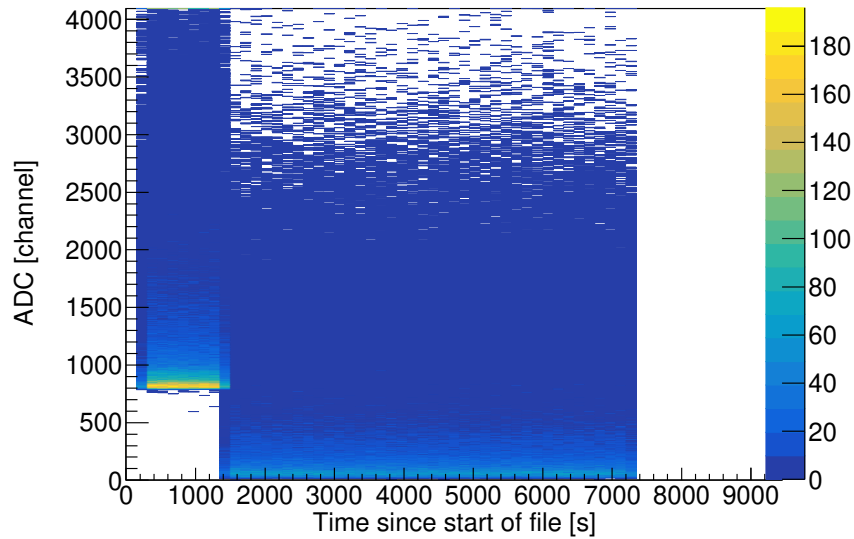


Figure 6.4: ADC spectra versus the time since the start of a single file for EJ-309 Detector 7. For every file where a gain offset like the one between 0-1500 seconds above, the offset data was discarded.

loaded onto the board did not match the firmware expected by the computer processing the output of the DAQ. As a result, all the data from the 9 organic scintillators and the LaBr on this board were discarded. Additionally, it was observed that a single detector on the other QDC board experienced discrete gain jumps at the beginning of each file, as seen in Figure 6.4, which shows the time since the start of the file versus the ADC value. The data at the beginning of the file where the gain had jumped was discarded (e.g. events earlier than 1500 seconds for the file shown in Figure 6.4 were not considered) and the integrated current for that detector was corrected for the fraction of the file that was discarded.

6.3 Activation Foil Analysis

Foil activation is a well established method to determine the absolute neutron fluence, either energy-differential via unfolding techniques [23] or energy integrated [18]. To normalize the neutron flux for the ^{56}Fe experiment, three thin foils of normal density, each cylindrical with a diameter of 2", were placed in the neutron beam for a certain amount of time. Assuming the neutron flux is constant over the irradiation time T_{irrad} , the activity of the radioactive products created in each foil from certain benchmarked reactions is

$$A_0 = N_T \langle \sigma_i \rangle \kappa I (1 - e^{-\lambda_i T_{irrad}}) T_{irrad} \quad (6.6)$$

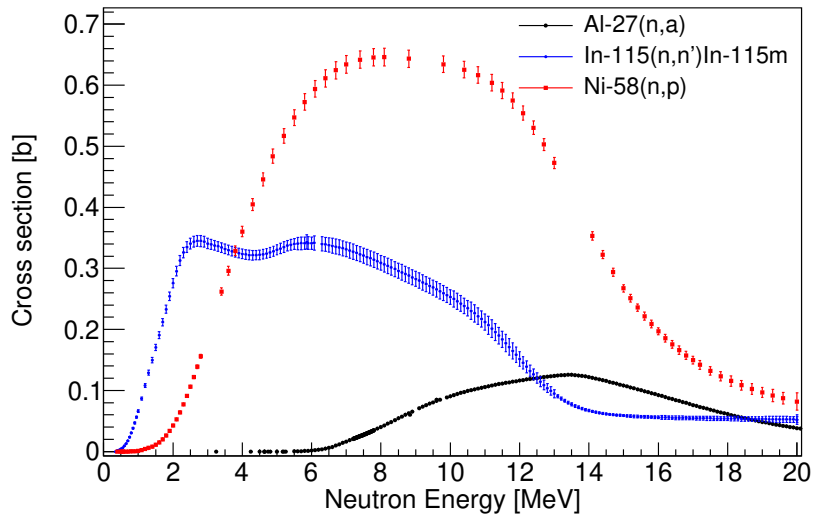


Figure 6.5: Activation foil cross sections with uncertainties from IRDFF-II [88]

where for reaction i , the sToF-measured flux-weighted cross section is

$$\langle \sigma_i \rangle = \frac{\int \phi(E_n) \sigma_i(E_n) dE_n}{\int \phi(E_n) dE_n} \quad (6.7)$$

N_T is the number of target nuclei, and λ_i is the decay constant for the product of reaction i . The factor κ is the total number of neutrons per μC per cm^2 and I is the average beam current. Following irradiation, the foils were taken to a calibrated HPGe and counted for some time $\Delta T = t_s - t_c$, where t_c is the time start time for the counting and t_s is the stop time, both relative to the end of the irradiation. The number of counts observed in the detector is

$$C_i = \frac{A_0}{\lambda_i} \epsilon(E_\gamma) BR (e^{-\lambda_i t_c} - e^{-\lambda_i (t_c + t_s)}) \quad (6.8)$$

where $\epsilon(E_\gamma)$ is the efficiency of the detector and BR is the intensity of the observed γ per decay. The efficiency of this detector was determined using a ^{152}Eu point source and interpolated using the Debertain fit function [63]. The above equations can be solved for κ .

The foils and reactions used to normalize the neutron flux measured by the sToF detector are listed in Table 6.2. The cross sections for the reactions were taken from IRDFF-II, which contains evaluated cross sections and uncertainties [88] and are plotted in Figure 6.5. The flux-weighted cross sections were computed numerically by averaging the IRDFF-II cross section over each sToF (Fig. 2.1) energy bin. These are reported in Table 6.2 with uncertainties computed from the IRDFF-II file and the statistical uncertainties on the sToF spectrum. The agreement between the indium and nickel activation follows from the fact that both reactions sample the energy region where most of the 14 MeV TTDB neutrons are.

	$^{115}\text{In}(n, n'\gamma)^{115}\text{In}^m$	$^{27}\text{Al}(n, \alpha)^{24}\text{Mg}$	$^{58}\text{Ni}(n, p)^{58}\text{Co}$
Foil Mass [$\pm 0.0001\text{g}$]	14.369	5.318	17.2187
E_γ [keV]	336	1369	810
$\langle\sigma\rangle$ [b]	0.313 ± 0.055	0.0237 ± 0.0071	0.503 ± 0.102
Total Fluence (10^8 n/cm 2)	3.66 ± 0.64	3.83 ± 1.15	3.55 ± 0.72
Differential Fluence (10^9 n/sr/ μC)	2.99 ± 0.52	3.13 ± 0.94	2.90 ± 0.59

Table 6.2: Experimental parameters and results of the activation foil neutron flux normalization.

The 3% difference indicates that the number of neutrons between the thresholds of the two reactions is small. The uncertainty-weighted average differential fluence of 2.97×10^9 n/sr/ μC was used to normalize the sToF spectrum.

Chapter 7

Secondary Neutron Distributions

7.1 Data Analysis

The extraction of secondary neutron energy/angle distributions from data gathered by only the sixteen operational organic liquid scintillators relies on the use of the forward modeling approach. After applying the light yield calibrations, the timing calibrations, and PSD shape and light yield constraints to select neutron events, the Total-time-since-last-RF for each event was calculated (TTOF). The total TTOF is the sum of the TOFs of the incident and outgoing neutrons minus n cyclotron RF periods:

$$\text{Total Time since last RF} = (TOF_{incoming} + TOF_{scattered}) - nT_{RF} \quad (7.1)$$

If it was possible to know, based on the neutron data only, what reaction occurred in the target (i.e. elastic scattering, inelastic scattering to the first excited state, inelastic scattering to the 30th excited state, etc.), then $TOF_{scattered}$ could be expressed in terms of the energy lost in the reaction, ΔE and $TOF_{incoming}$

$$TOF_{scatter} = \frac{D_{scatter}}{c} \left(1 - \left(\left(1 - \left(\frac{D_{inc}}{TOF_{inc}c} \right)^2 \right)^{-1/2} - \frac{\Delta E}{m_n c^2} \right)^{-2} \right)^{-1/2} \quad (7.2)$$

where $D_{scatter}$ is the distance from the ⁵⁶Fe target to the detector, and D_{inc} is the distance from the break-up target to the ⁵⁶Fe. For the ⁵⁶Fe experiments, it is impossible to infer what reaction occurred in the target based on the data from the neutron detectors alone. Nevertheless, the information obtained by the organic scintillators can be used to construct data products that can be used in a forward modeling approach to extract the secondary energy/angle distributions.

The data product used was a 2-D histogram of TTOF versus light yield for each detector. These 2-D histograms are generated for data with the ⁵⁶Fe target in place and data with the “Blank” for use as a background subtraction. The background data was scaled by the ratio

of the integrated current for the ^{56}Fe data to the “Blank” data

$$B = \frac{\text{Total Charge } ^{56}\text{Fe}}{\text{Total Charge Blank}} = 13.82 \quad (7.3)$$

Figure 7.1 shows the background subtracted Total Time-since-last-RF versus light yield spectrum for Detector 8, at 70.0 cm from the center of the array and 13.1° relative to the incident neutron beam. The main feature of the spectrum is the np edge from neutrons that underwent elastic scattering in the ^{56}Fe target. Two distinct edges can be seen, corresponding to neutrons from various beam pulses. Figure 7.2 shows the background subtracted Total

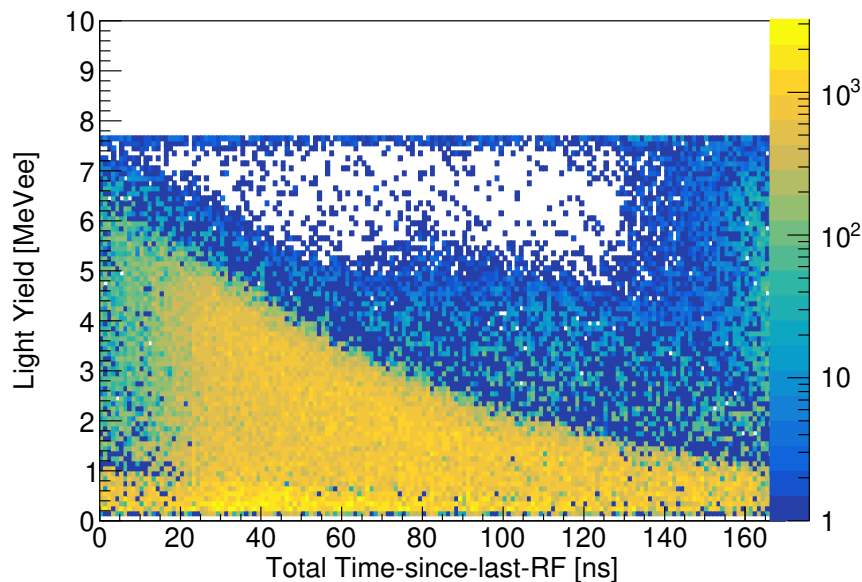


Figure 7.1: Experimental TTOF versus light yield for scintillator 8 at 13.1° relative to the neutron beam.

Time-since-last-RF spectrum for the subset of operational EJ-309 detectors at angles of $90^\circ \pm 30^\circ$ relative to the incident neutron beam. Again the dominant feature is the np edge from neutrons that elastically scattered in the ^{56}Fe target but the variations in detector distance from the target, variations in detector light yield resolution and gain blurs the feature. Additionally, the reduction in the elastic scattering cross section at these angles reduces the overall amount of signal.

The TALYS keyword `ddxmode 3` outputs the secondary neutron energy/angle distributions, $\phi(E_n, E_{n'}, \theta_{n'})$, normalized to the sum of the cross sections contributing to the distribution at each incident neutron energy. These distributions were used to construct the Total Time-since-last-RF versus light yield data products for the forward model. A 2D matrix \mathbf{Y}_d was built for each detector with t columns representing the Total-time-since-last-RF and

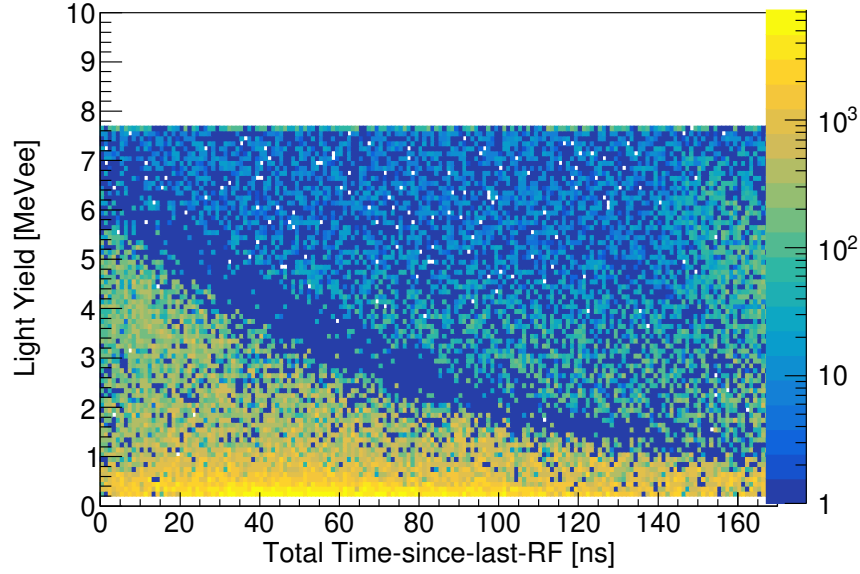


Figure 7.2: Experimental TTOF versus light yield for scintillators with angles between 60° and 120° .

$n \times m$ rows for the n secondary neutron energy bins and m secondary neutron angle bins.

$$\mathbf{Y}_d = \begin{pmatrix} Y(TTOF_0, E_0, \theta_0) & Y(TTOF_1, E_0, \theta_0) & \dots & Y(TTOF_t, E_0, \theta_0) \\ Y(TTOF_0, E_1, \theta_0) & Y(TTOF_1, E_1, \theta_0) & \dots & Y(TTOF_t, E_1, \theta_0) \\ \vdots & \vdots & \dots & \vdots \\ Y(TTOF_0, E_0, \theta_1) & Y(TTOF_1, E_0, \theta_1) & \dots & Y(TTOF_t, E_0, \theta_1) \\ Y(TTOF_0, E_1, \theta_1) & Y(TTOF_1, E_1, \theta_1) & \dots & Y(TTOF_t, E_1, \theta_1) \\ \vdots & \vdots & \dots & \vdots \\ Y(TTOF_0, E_n, \theta_m) & Y(TTOF_1, E_n, \theta_m) & \dots & Y(TTOF_t, E_n, \theta_m) \end{pmatrix} \quad (7.4)$$

To fill this matrix, the yield was calculated by multiplying the secondary energy/angle distribution by the 1D dimensional, raw neutron flux $\Phi(E_n)$, the ^{56}Fe target areal density, $(\rho R)_{target}$, the target solid angle, Ω_{target} , and the total integrated current, C_{total} :

$$Y(E_{n'}, \theta_{n'}, E_n) = \Phi(E_n) \phi(E_n, E_{n'}, \theta_{n'}) (\rho R)_{target} \Omega_{target} C_{total} . \quad (7.5)$$

The uncertainty on this yield is

$$\text{Var}(Y(E_{n'}, \theta_{n'}, E_n)) = Y(E_{n'}, \theta_{n'}, E_n)^2 \left(\left(\frac{\sigma_\Phi}{\Phi} \right)^2 + \left(\frac{\sigma_{\rho R}}{\rho R} \right)^2 + \left(\frac{\sigma_\Omega}{\Omega} \right)^2 \right) . \quad (7.6)$$

The known incident and outgoing energies were used to calculate the incident and outgoing neutron TOF, giving the yield $Y(TOF_n, TOF_{n'}, \theta_{n'})$. The Total-time-since-last-RF was calculated for each yield, giving $Y(TTOF, E_{n'}, \theta_{n'})$. A Gaussian distribution with $\sigma = 8.5$ ns,

corresponding to the timing structure of the deuteron beam pulse inferred from the γ -flash, was used to convolve the yields in TTOF. Multiplying the smeared matrix by the response matrix R_d for a given detector (see Sec. 5.2) gives the calculated Total-time-since-last-RF versus light yield $Y_d(TTOF, L)$:

$$\mathbf{Y}_d(L, TTOF) = R(L, E_{n'}, \theta_{n'}) \mathbf{Y}(E_{n'}, \theta_{n'}, TTOF). \quad (7.7)$$

The uncertainty for a given element of the matrix is

$$\begin{aligned} Var(Y_d(L_j, TTOF_i)) = & \sum_k^n \sum_s^m R_d(L_j, E'_k, \theta'_s)^2 Var(Y(E'_k, \theta'_s, TTOF_i)) \\ & + Var(R_d(L, E'_k, \theta'_s)) Y(E'_k, \theta'_s, TTOF_i)^2. \end{aligned} \quad (7.8)$$

Figure 7.3 shows this distribution for Detector 8, based on a TALYS1.96 calculation using keywords `best y` and `elwidth 0.1`. Figure 7.4 shows this distribution for detectors between 60° and 120° .

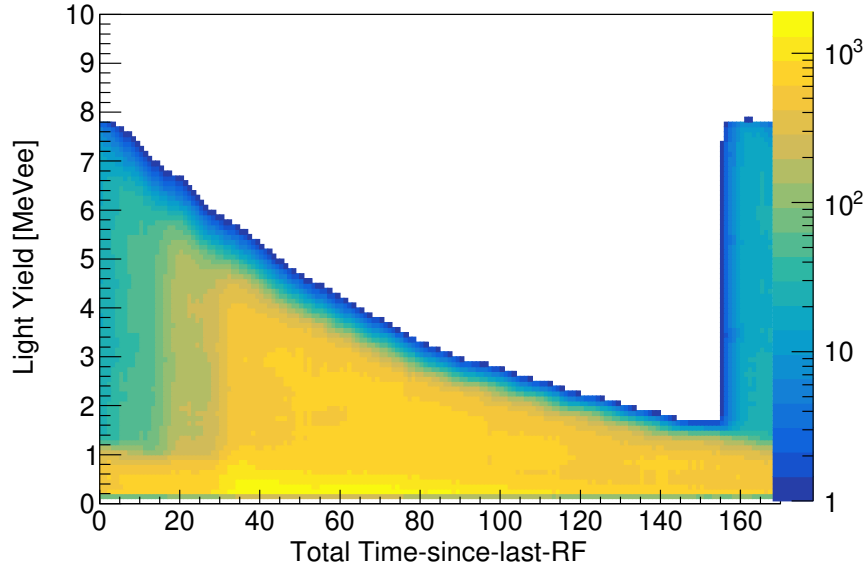


Figure 7.3: Calculated TTOF versus light yield for EJ-309 Detector 8 at 13.1° .

To more clearly scrutinize the qualitative and quantitative differences between the experimental and calculated distributions, projections onto the light yield axis for 1 ns TTOF intervals were taken. Figure 7.5 shows the comparison of the experimental and calculated light yield spectrum for two TTOF slices from Detector 8. A common feature of these projections, across all TTOF's and all detectors is the presence of strong statistical fluctuations arising mainly due to the fact that $B \gg 1$, meaning the amount of target-out

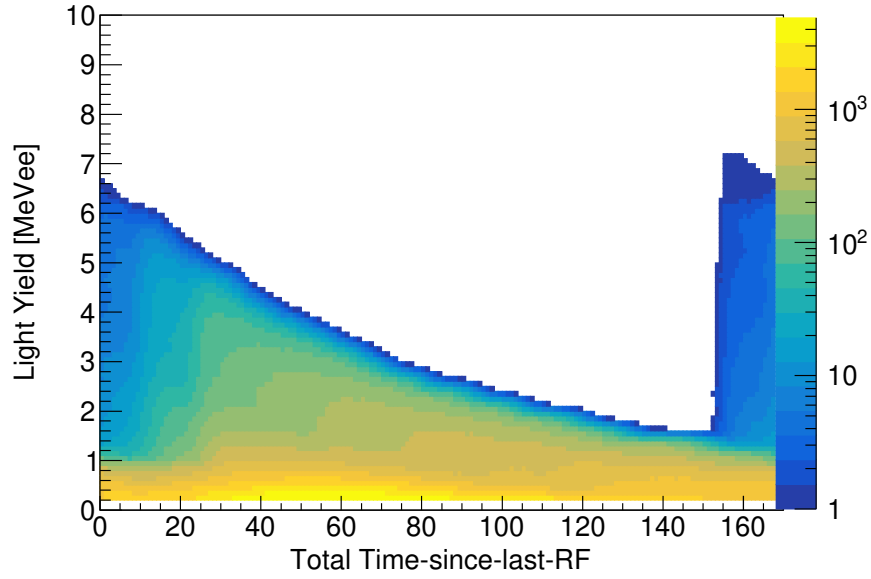


Figure 7.4: Calculated TTOF versus light yield for EJ-309 detectors between 60° and 120° .

data is much less than the amount of target-in data. Detector 8 is both the most forward angle detector, and therefore has the strongest signal, and is also closest to the unreacted neutron beam, meaning small angle neutron scatters on air are strongly contributing to the background signal. The statistical fluctuations in this detector are therefore less than every other detector.

For secondary neutron energy/angle distributions, the objective function for the forward model is a χ^2 between the experimental and calculated Total-time-since-last-RF versus light yield distributions:

$$\chi^2 = \sum_i^t \sum_j^l \frac{(Y_{obs}(L_j, TTOF_i) - Y_{calc}(L_j, TTOF_i))^2}{Var_{obs}(L_j, TTOF_i) + Var_{calc}(L_j, TTOF_i)} \quad (7.9)$$

where $Y(TTOF_i, L_j)$ is the number of neutrons at TTOF i that produced an event with light yield L_j , t is the total number of TTOF bins, and l is the total number of light yield bins. The uncertainty on the observed yield is the statistical uncertainty from the target in and blank data:

$$Var_{obs}(L_j, TTOF_i) = Y_{target\ in}(L_j, TTOF_i) + B^2 Y_{target\ out}(L_j, TTOF_i) \quad (7.10)$$

with B defined in Eq 7.3. The uncertainty on the calculated yield is given by Eq. 7.8. The TALYS keywords included in the minimization are listed in Table 4.1. The starting values for the twelve parameters are the default values listed in the table.

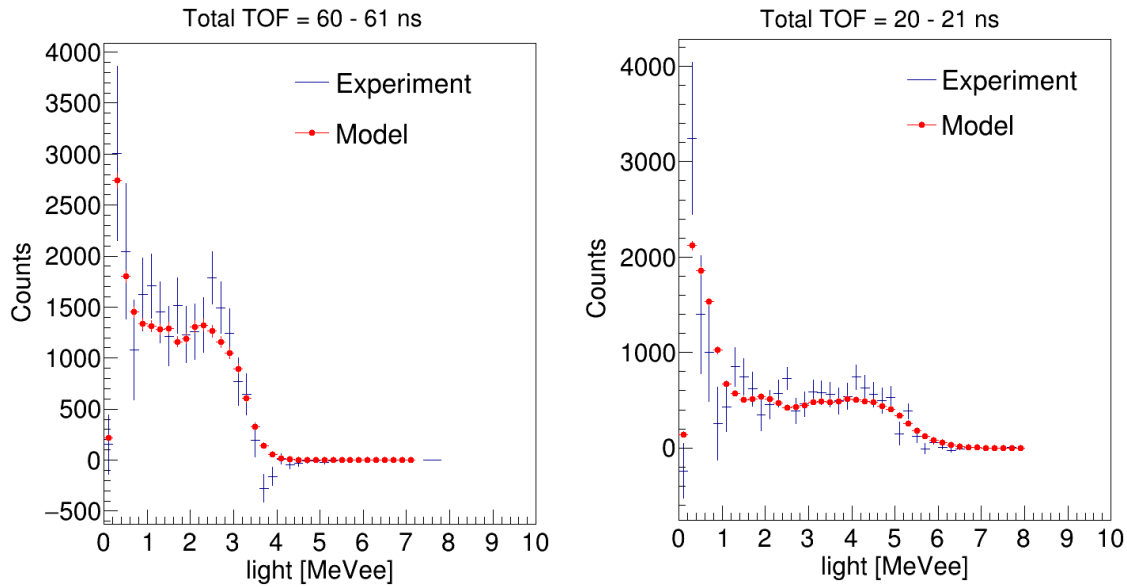


Figure 7.5: Experimental and calculated light yield spectra in EJ-309 Detector 8 for two TTOF slices at 60-61 ns and 20-21 ns. The first edge in both spectra is from elastic scattering in the ^{56}Fe target by neutrons from the dominant wrap. The elastic scattering edge from neutrons in the wrap before are visible at ≈ 0.6 MeVee for the slice on right left and ≈ 0.8 MeVee for the slice on the right.

7.2 Results

The results of the forward modeling minimization are presented in Table 7.1. At the end of the minimization, $\chi^2/\nu = 2.24$ for the 12 parameters and using detectors 8, 7, 6, and the group of detector between 60° and 120° . As expected, not much adjustment was needed to the well established optical model parameters, the largest changes being a roughly 5% increase in the diffuseness of the real, volume-central neutron optical model well and a roughly 8.5% increase one of the parameters defining the shape of the imaginary surface-central neutron optical model well. The full covariance matrix, including the covariances with the level density parameters, is shown in Chapter 10.

The mean parameters and covariances can be used to calculate secondary neutron distributions and cross sections and uncertainties with TALYS. Figure 7.6 shows the elastic scattering cross section along with the elastic scattering cross section from ENDF/B-VIII.0 (MT=2) [3]. There is good agreement from 2.5 to 9 MeV. Below 2 MeV and from 9-11.5 MeV, the two cross sections agree with error. Above 11.5 MeV, the two cross sections do not agree, which could indicate that the high energy part of the sToF spectrum is too small, leading the forward model to compensate by increasing the cross section in this range, or that the efficiency of the neutron detectors in this range is too low. Figure 7.7 shows the partial

Keyword	Value
avadjust n	$1.05642 \pm 4.6 \times 10^{-5}$
awdadjust n	$1.00024 \pm \times 10^{-5}$
d1adjust n	$1.04381 \pm 1.5 \times 10^{-4}$
d2adjust n	$1.08445 \pm 1.5 \times 10^{-4}$
d3adjust n	$0.998634 \pm 3.6 \times 10^{-5}$
elwidth	$0.0306683 \pm 6.8 \times 10^{-6}$
rvadjust n	$1.00058 \pm 1.7 \times 10^{-4}$
rvsoadjust n	$0.999785 \pm 2.6 \times 10^{-4}$
rwdadjust n	$1.00129 \pm 7.0 \times 10^{-5}$
v1adjust n	1.00236 ± 1.303
v2adjust n	$0.999366 \pm 1.7 \times 10^{-4}$
w2adjust n	$0.999723 \pm 1.7 \times 10^{-4}$

Table 7.1: Optimal values for TALYS keywords when compared against GENESIS secondary neutron energy/angle data.

inelastic scattering cross section to the first excited state in ^{56}Fe along with the ENDF/B-VIII.0 cross section (MT=51). The cross sections agree over the whole energy range, but the mean of the TALYS cross section is quite a bit higher than the evaluated cross section at higher neutron energies, as was the case with the elastic scattering. Figure 7.8 shows the relative contributions to the total elastic scattering for three different angles, corresponding to EJ-309 detectors 6, 7, and 8. The uncertainties on these calculated cross sections are large and more work could be done to reduce the number of parameters to better constrain the minimization or a different minimization algorithm that is guaranteed to find a global minimum could be employed.

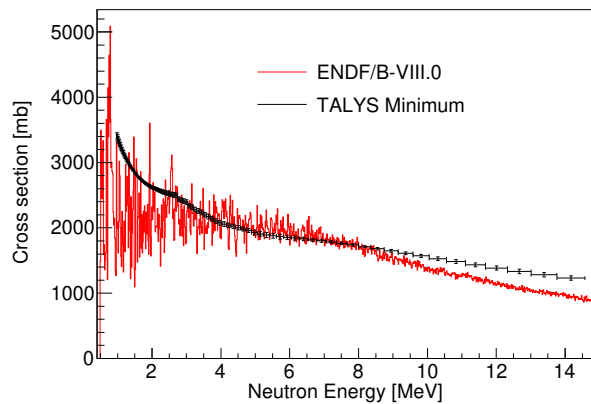


Figure 7.6: ^{56}Fe elastic scattering cross section calculated using TALYS parameters obtained from the forward model minimization against GENESIS neutron singles data. The y-errors are computed from the covariance obtained at the end of the minimization. Also plotted is the cross section from the ENDF/B-VIII.0 library.

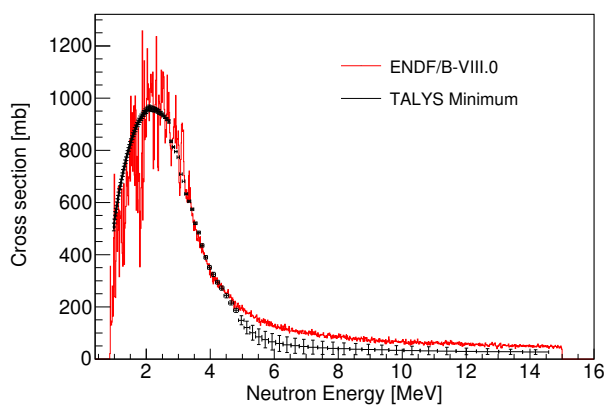


Figure 7.7: $^{56}\text{Fe}(n, n_1\gamma)$ partial inelastic scattering cross section calculated using TALYS parameters obtained from the forward model minimization against GENESIS neutron singles data. The y-errors are computed from the covariance obtained at the end of the minimization. Also plotted is the cross section from the ENDF/B-VIII.0 library.

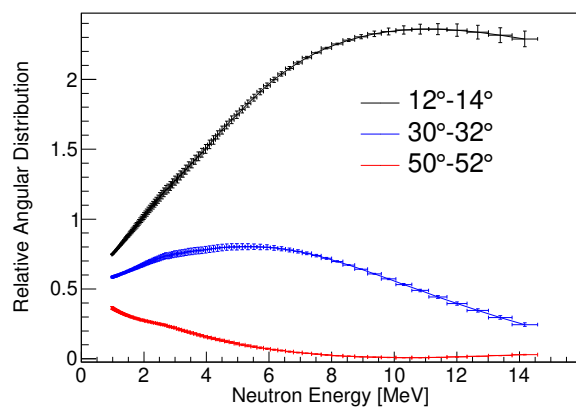


Figure 7.8: ^{56}Fe elastic scattering relative angular distributions for 3 EJ-309 detectors (6, 7, 8) calculated using TALYS parameters obtained from the forward model minimization against GENESIS neutron singles data. The y-errors are computed from the covariance obtained at the end of the minimization.

Chapter 8

Gamma-ray Production

8.1 Data Analysis

The determination of gamma-ray production cross sections from the data gathered with GENESIS can be accomplished via application of the traditional or forward modeling analysis approaches. Both start with the same data product, the yield of a discrete gamma-ray one of the HPGe CLOVER detectors as a function of Time-since-last-RF.

After the raw data from the DAQ has been processed and events associated with their correct detectors, γ energy and time calibrations are applied. The data are then accumulated into spectra for each CLOVER leaf as a function of Time-since-last-RF. Total detection mode spectra are also generated, taking as the Time-since-last-RF for the summed event the first gamma detection in the CLOVER. A background subtraction was done using the data with the Be target in place. Figure 8.1 shows the 2D spectrum for CLOVER 1 (49.2°) in total detection mode. Figure 8.2 shows the spectrum for CLOVER 1 in total detection mode, for Time-since-last-RF between 0 and 169.29 ns. The peaks labeled are the discrete transitions from $^{56}\text{Fe}(n, n'\gamma)$ that were observed in sufficient quantity to perform further analysis. The yield as a function of Time-since-last-RF was found by dividing the time domain into bins of $\Delta T = 169.29/14$ ns.

To extract the yield under each photo-peak in a given Time-since-last-RF bin, a χ^2 fit of

$$Y(E_\gamma, TOF_j) = A_0 \exp\left(-\frac{(E_\gamma - E_0)^2}{\sqrt{2}\sigma^2}\right) + C \quad (8.1)$$

was performed. The parameter σ was fixed based on the measured detector resolution (Sec 3.2). The centroid of each peak, E_0 , was also fixed based on the expected γ energy from ENSDF [89]. To better constrain the constant background term, some transitions were fit simultaneously. The 1238.3 keV $4_1^+ \rightarrow 2_1^+$ and the 1303 keV $6_1^+ \rightarrow 4_1^+$ yrast transitions were fit simultaneously. The 2094.0 keV $0_1^+ \rightarrow 2_1^+$ and the 2113.1 keV $2_3^+ \rightarrow 2_1^+$ transitions were also fit simultaneously. The area was computed using

$$A = \frac{A_0 \sqrt{2\pi}\sigma}{BW} \quad (8.2)$$

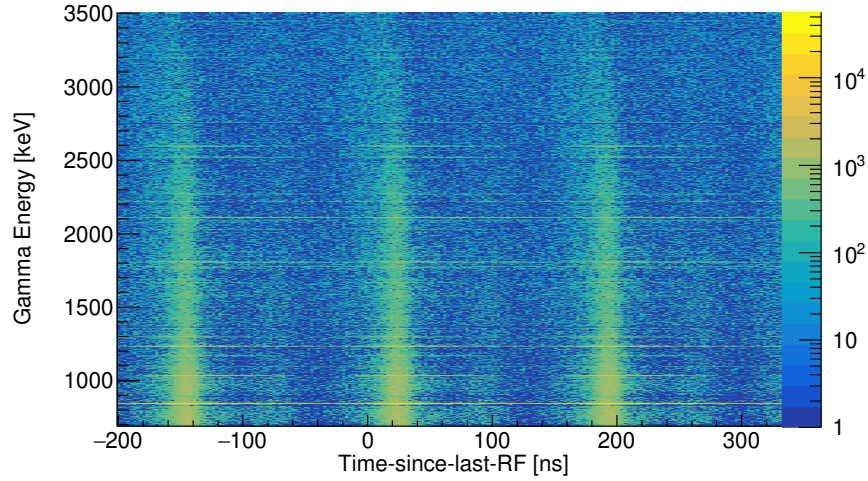


Figure 8.1: Background subtracted Time-since-last-RF relative to the 3 RF signals nearest the event time versus gamma energy for Clover 1 in total detection mode. The 846.8 keV, 1037.8 keV, 1238.3 keVs and 1810.8 keV transitions can be clearly seen.

where BW is the bin width of the spectrum. The uncertainty on the fitted peak area is

$$\sigma_A = A \sqrt{\left(\frac{\sigma_{A_0}}{A_0}\right)^2 + \left(\frac{\sigma_\sigma}{\sigma}\right)^2} \approx A \frac{\sigma_{A_0}}{A_0} \quad (8.3)$$

because the uncertainty on the fitted resolution from Table 3.1 is much smaller than the uncertainty on the fitted peak amplitude.

In order to compare $Y(E_\gamma, TOF_j)$ to forward model calculations based on angle-integrated gamma production cross sections or to extract angle-integrated cross sections from the yields in Time-since-last-RF regions that do not suffer from frame overlap, the angular distribution (Eq. 4.15) needs to be known. This can be calculated from the data for certain transitions that are known to possess a large degree of anisotropy and where the single-leaf statistics are sufficient. The $Y(E_\gamma, TOF_j, \cos \theta_{leaf})$ can be calculated and after correcting for the efficiency of each leaf a modified form of Eq. 4.15,

$$Y(E_\gamma, TOF_j, \cos \theta_{leaf}) = \alpha(E_\gamma, TOF_j) \left(1 + a_2(E_\gamma, TOF_j) P_2(\cos \theta_{leaf}) + a_4(E_\gamma, TOF_j) P_4(\cos \theta_{leaf}) \right), \quad (8.4)$$

can be fit to the data. The eight CLOVER crystals were grouped into four angles with two crystals at each angle. For the ^{56}Fe experiment, the CLOVER crystals were at $97.3^\circ \pm 5.8^\circ$, $85.7^\circ \pm 5.8^\circ$, $53.5^\circ \pm 4.4^\circ$, and $44.8^\circ \pm 4.4^\circ$. Figure 8.3 shows the angular distribution for the 846.8 keV $2_1^+ \rightarrow \text{G.S.}$ transition for Time-since-last-RF between 0 and 12.09 ns with $\alpha = 1.432 \times 10^8 \pm 23534.8$, $a_2 = -0.0866 \pm 7 \times 10^{-4}$ and $a_4 = -0.4054 \pm 7 \times 10^{-4}$. The band represents the uncertainty in the fitted curve from the covariance matrix. The correction

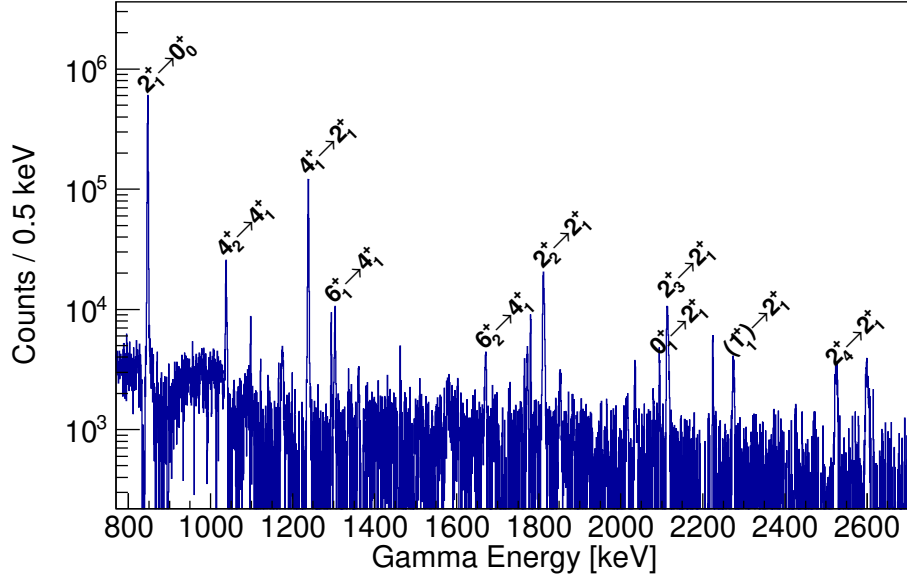


Figure 8.2: Gamma spectrum for Clover 1 showing the inelastic scattering gamma transitions

factor for the CLOVER total detection mode yields can be found from

$$C(E_\gamma, TOF_j, \theta_{CLOVER}) = \frac{\alpha(E_\gamma, TOF_j)}{Y(E_\gamma, TOF_k, \cos \theta_{CLOVER})} \quad (8.5)$$

The angular spread of the crystals means that the fit is not well constrained, especially the parameter a_4 , and the correction factors from the CLOVER crystals cannot be used for this data set. It can be shown that the correction factor for a detector at 55° is 1 [90]. For the rest of the analysis, the correction factor for Clover 1 at 49.2° is assumed to be $C(E_\gamma, TOF_j, 49.2^\circ) = 1$ and the data from Clover 0 at 91.5° was scaled to match. The expected uncertainty introduced by this assumption can be estimated by convolving Eq. 4.15 evaluated at 49.2° , using the a_2 and a_4 parameters from [91], with the neutron flux (Fig. 2.1) and then mapping into Time-since-last-RF. The ratio of this yield to the yield calculated without the angular distribution gives the average deviation of the expected yield in Clover 1 under the assumption that $C(E_\gamma, TOF_j, 49.2^\circ) = 1$. The expected uncertainty introduced in the 846.8 keV gamma production cross section is 2.1%. The expected uncertainty introduced in the 1238.3 keV gamma production cross section is 3.6%. The expected uncertainty introduced in the 1810.8 keV gamma production cross section is 2.8%.

Figure 8.4 shows the yield in Clover 1 of the 846.8 keV γ as a function of Time-since-last-RF. For comparison, the angle-integrated production cross section measured by Negret *et al.* [9] convolved with the sToF spectrum and mapped into the Time-since-last-RF domain is also plotted. The upper x-axis in Figure 8.4 shows the neutron energies contributing to the yield at each Time-since-last-RF.

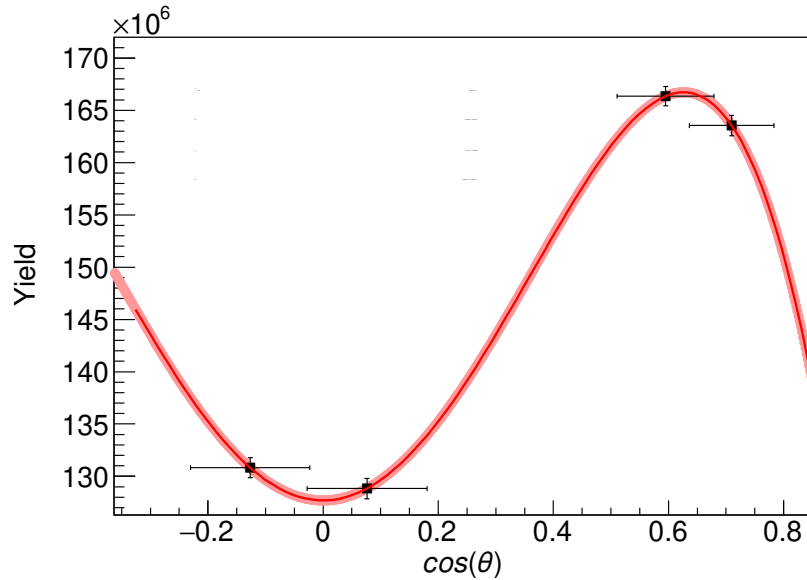


Figure 8.3: Angular distribution for the 846.8 keV $2_1^+ \rightarrow \text{G.S.}$ transition for Time-since-last-RF between 0 and 12.09 ns. The curve is a fit to Eq 8.4, with $\alpha = 1.432 \times 10^8 \pm 23534.8$, $a_2 = -0.0866 \pm 7 \times 10^{-4}$ and $a_4 = -0.4054 \pm 7 \times 10^{-4}$.

To calculate the gamma production cross section for Time-since-last-RF bins that do not suffer from frame overlap, the flux matrix (Fig. 5.3) was used. The neutron yield corresponding to each beam pulse in a given Time-since-last-RF bin was calculated by looping over each column in the flux matrix corresponding to that TOF row. If the neutron energy for that column was above the threshold for a given gamma production reaction, the neutron yield was added to the total neutron yield from the nearest beam pulse. The total neutron yield in each row was also calculated. If the neutron yield from any given beam pulse in a Time-since-last-RF bin constituted $\geq 95\%$ of the total neutron yield, the bin was considered non-wrapped. The mean neutron energy was calculated as the 50th percentile of the neutron yield for the corresponding beam pulse. The reported energy uncertainty was calculated from a cumulative density function (CDF) of the neutron yield for the beam pulse and corresponds to the energy range from which 68% of the total neutron yield came.

The gamma-ray yield is not directly calculated from the nuclear models outlined in Sec. 4.1. Rather, the yield can be calculated from partial inelastic scattering cross sections (i.e. the scattering to each discrete level or the continuum) and the known level scheme and branching ratios. TALYS uses the RIPL-03 [80] library for the branching ratios of ^{56}Fe transitions and accumulates the yields for each discrete transition into angle-integrated γ -production cross sections at each incident neutron energy.

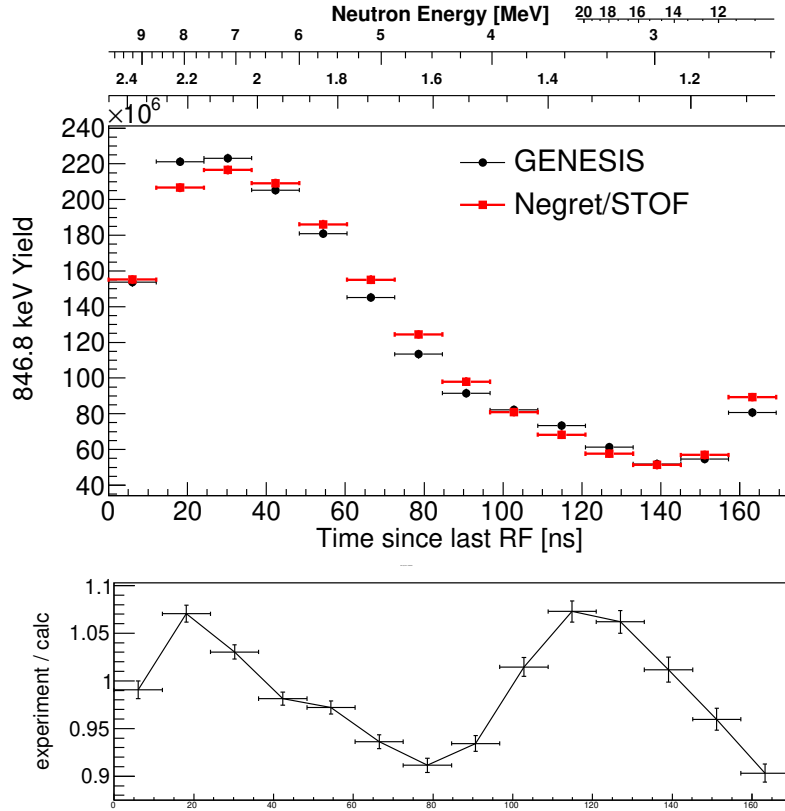


Figure 8.4: Yield of the 846.8 keV gamma-ray versus Time-since-last-RF for CLOVER 1 (49.2°). The red data points are calculated using the flux matrix and the measurement by Negret [9]. The ratio of the experimental yield to the calculated yield is also shown. The upper x-axis shows the energies of the neutrons contributing to the yield in each TOF bin.

The objective function for an individual γ production yield is

$$\chi^2(E_\gamma) = \sum_i \frac{(Y_{obs}(TOF_i, E_\gamma) - Y_{calc}(TOF_i, E_\gamma))^2}{\sigma_{obs}^2(TOF_i, E_\gamma) + \sigma_{calc}^2(TOF_i, E_\gamma)} \quad (8.6)$$

where $Y(TOF_i, E_\gamma)$ is the yield for a discrete gamma of energy E_γ at Time-since-last-RF TOF_i . The uncertainty on the observed yield is the statistical uncertainty and the uncertainty on the calculated yield is a quadrature sum of the uncertainty on the efficiency and the uncertainty from the flux. For a ratio of yields, the objective function is

$$\chi_R^2(E_{\gamma,1}, E_{\gamma,2}) = \sum_i \frac{(R_{obs}(TOF_i, E_{\gamma,1}, E_{\gamma,2}) - R_{calc}(TOF_i, E_{\gamma,1}, E_{\gamma,2}))^2}{\sigma_{obs}^2(TOF_i, E_{\gamma,1}, E_{\gamma,2}) + \sigma_{calc}^2(TOF_i, E_{\gamma,1}, E_{\gamma,2})} \quad (8.7)$$

where

$$R(TOF_i, E_{\gamma,1}, E_{\gamma,2}) = Y(TOF_i, E_{\gamma,1})/Y(TOF_i, E_{\gamma,2}) \quad (8.8)$$

and

$$\sigma^2(TOF_i, E_{\gamma,1}, E_{\gamma,2}) = Y(TOF_i, E_{\gamma,1}, E_{\gamma,2}) \left(\left(\frac{\sigma(TOF_i, E_{\gamma,1})}{Y(TOF_i, E_{\gamma,1})} \right)^2 + \left(\frac{\sigma(TOF_i, E_{\gamma,2})}{Y(TOF_i, E_{\gamma,2})} \right)^2 \right) \quad (8.9)$$

The ratio between the 846.8 keV and 1238.3 keV yields observed in Clover 1 as a function of Time-since-last-RF is shown in Figure 8.5. Two different calculated yields are also plotted. One TALYS calculation had `s2adjust 26 56` set to 3.0 and the other TALYS calculation had that keyword set to its default value of 1.0. The χ^2 (Eq. 8.7) for the calculation with default parameters was 7.89 and for the calculation with the increased width of the spin-distribution component of the nuclear level density $\chi^2 = 24.48$.

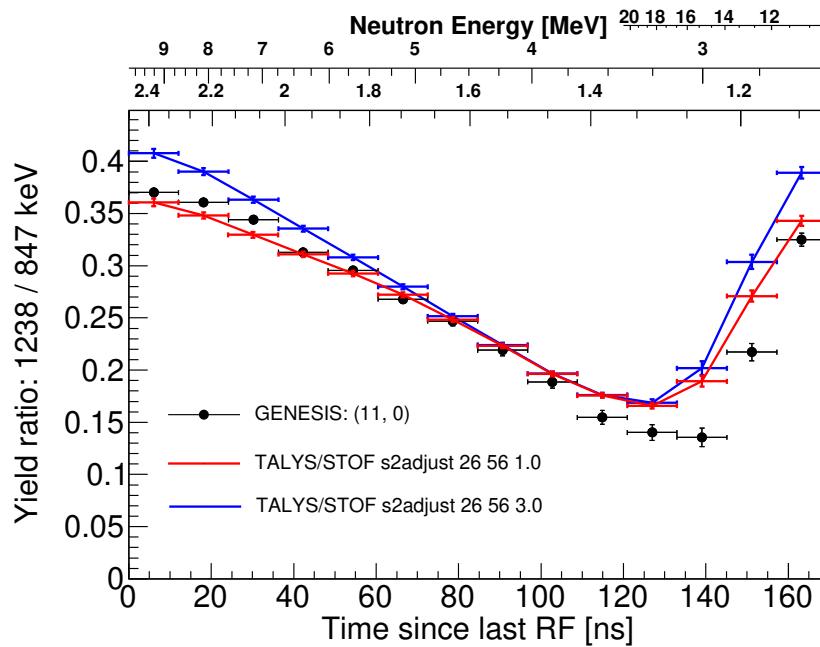


Figure 8.5: Yield ratio for the 846.8 keV and 1238.3 keV γ transitions in ^{56}Fe . Two forward-modeled yields are also plotted based on two TALYS calculations with different values for the keyword `s2adjust 26 56`. The χ^2 when this keyword set to 1.0 (red curve) was 7.89. When the keyword set to 3.0 (blue curve) the χ^2 was 24.48.

8.2 Results

The transitions that have Time-since-last-RF bins that do not suffer from wrap-around are indicated in Figure 5.1. The results of the traditional approach are presented in Figures 8.6-8.15. The GENESIS results presented are from Clover 1 at 49.2° and are compared to

measurements from the measurements by Negret [9], Dickens [11], and Beyer [10]. The cross sections from these measurements have been averaged over the energy bin widths obtained from the flux matrix. Overall, good agreement with the previous measurements is obtained.

Also plotted in Figures 8.6-8.15 are the results of the forward model calculation and the cross sections from a default TALYS calculation with keyword `best`. The minimum parameters from the forward model are presented in Table 8.1 along with the uncertainties on the parameters. The correlation matrix for these parameters is presented in the following chapter. As with the nOMP parameters found in the previous chapter, it is expected that the parameters included in the minimization against the gamma ray yield data would be close to default values. The major differences between the cross section obtained with the traditional method and those obtained with the forward model occur at high neutron energy where the flux measured by the sToF detector is most uncertain which is reflected in the error-bars. The measured 1037.8 keV production cross section (Fig. 8.8) shows a significant disagreement. The first excited state in ^{70}Ge is at 1039.506 keV giving rise to a triangular feature in the spectrum, and a peak that overlaps with the 1037.8 keV peak from ^{56}Fe . This contaminating peak is removed when the Be-target background subtraction is performed, but given the relative lack of background data, the resulting spectrum may still contain some residual contamination. The 1810.8 keV cross sections also disagrees between 5 MeV and 9 MeV. Negret [9] report similar disagreement between their measurement and TALYS1.6 calculations. The 2523.1 keV cross section also disagrees from 5-7 MeV. This is due to a 2523.09 keV transition from the $E_x = 4608.56$ keV, $J^\pi = 2^+$ level in ^{56}Fe which has a production cross section in this energy range of about 10 mb according to the TALYS calculations. The existence of this contaminating gamma ray is not noted in the previous measurements and all of the cross section was attributed to the $2_4^+ \rightarrow 2_1^+$ transition. Figure 8.14 shows the total production cross section for gamma rays with $E_\gamma = 2523.1$ keV compared to the TALYS cross section for the $2_4^+ \rightarrow 2_1^+$ transition. Figures 8.9 and 8.13 also show disagreement at higher neutron energies. These gamma rays come from levels with $J^\pi = 6^+$ and agreement could be possibly be obtained by further increasing the width of the spin distribution (Eg 4.18) with an energy-dependent `s2adjust` which is not currently an option.

Figure 8.16 shows the wrapped gamma-ray yield for the 846.8 keV ($2_1^+ \rightarrow G.S.$) transition in ^{56}Fe . This gamma-ray is completely wrapped. The GENESIS data is compared to the results of the forward model minimization. As with the non-wrapped cross sections, the largest disagreement is in the Time-since-last-RF bins where the high-energy portion of the neutron spectrum contributes most.

Figures 8.17a-8.18d show the ratio of the gamma-ray production cross section measured by Clover 0 at 91.5° and Clover 1 at 49.2° . The gain on Clover 0 was such that the highest energy gamma observed was the 2113.1 keV transition. When available, the ratio from the GENESIS data is compared to the measurement by Savin [92] at 90° and 125° . Given the uncertainties on the GENESIS and Savin data, the agreement for the three ratios (Figures 8.17a, 8.17b, and 8.18d) is good.

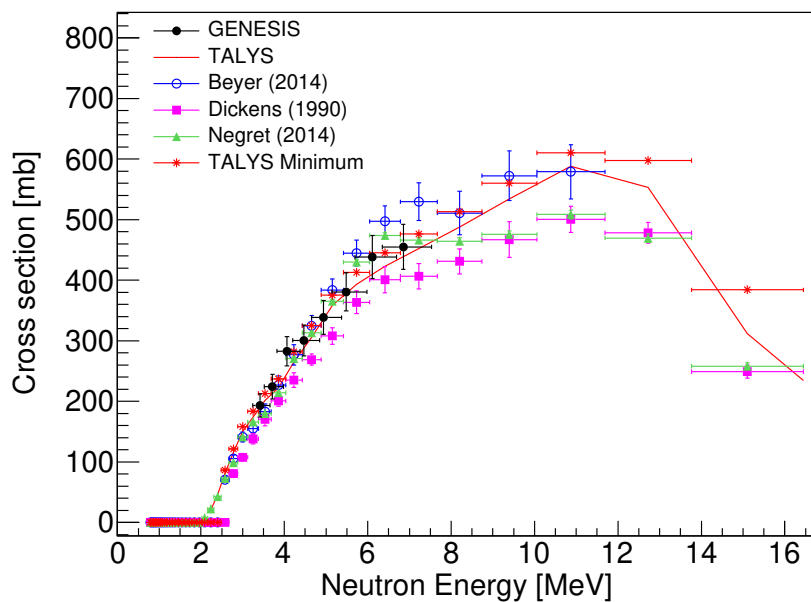


Figure 8.6: 1238.3 keV production at 49.2 degrees

Keyword	Value
Pshiftadjust 26 56	$-0.0999665 \pm 1.58 \times 10^{-5}$
Tadjust 26 56	$1.21739 \pm 1.72 \times 10^{-5}$
alimit 26 56	$7.99715 \pm 9.30 \times 10^{-5}$
s2adjust 26 56	$1.20145 \pm 1.34 \times 10^{-5}$

Table 8.1: Optimal values for TALYS keywords when compared against GENESIS gamma ray production data.

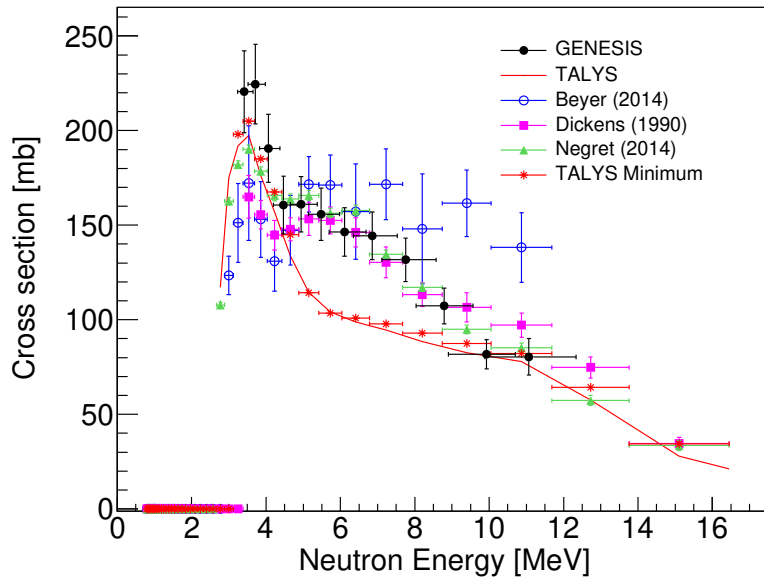


Figure 8.7: 1810.8 keV production at 49.2 degrees

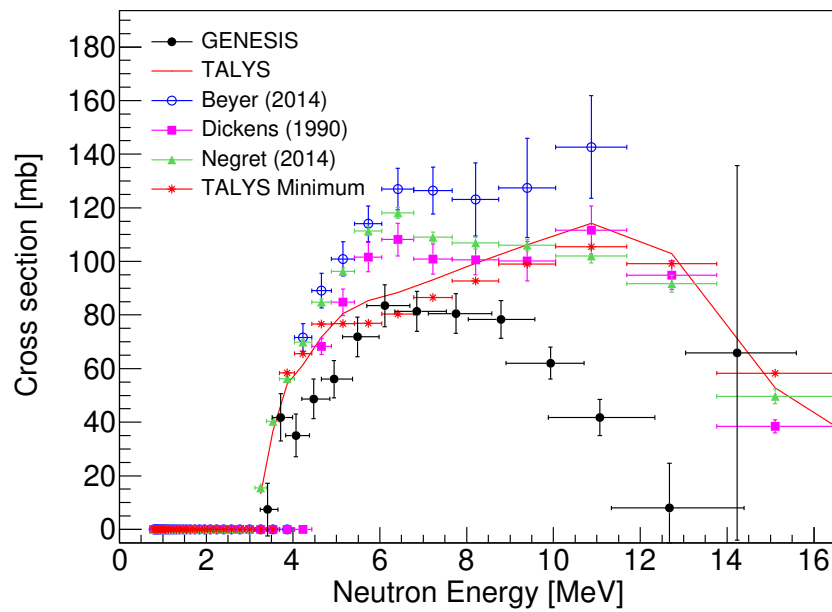


Figure 8.8: 1037.8 keV production at 49.2 degrees

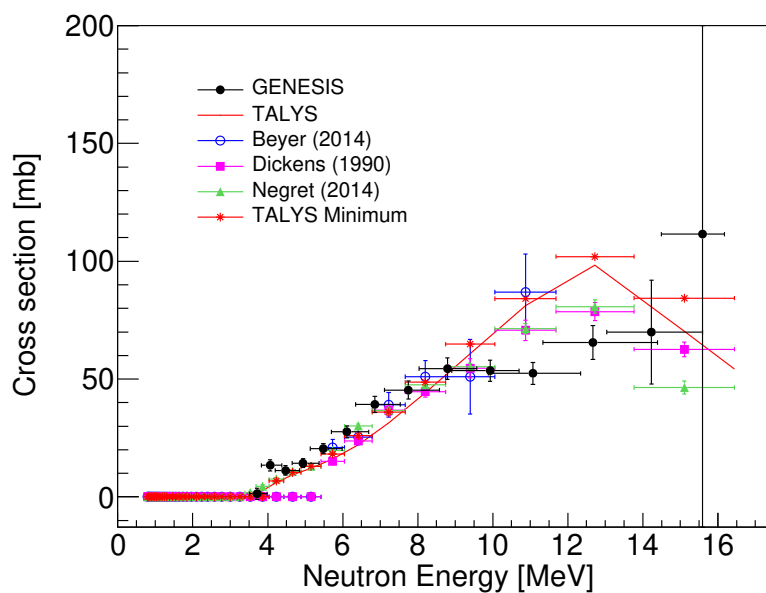


Figure 8.9: 1303.4 keV production at 49.2 degrees

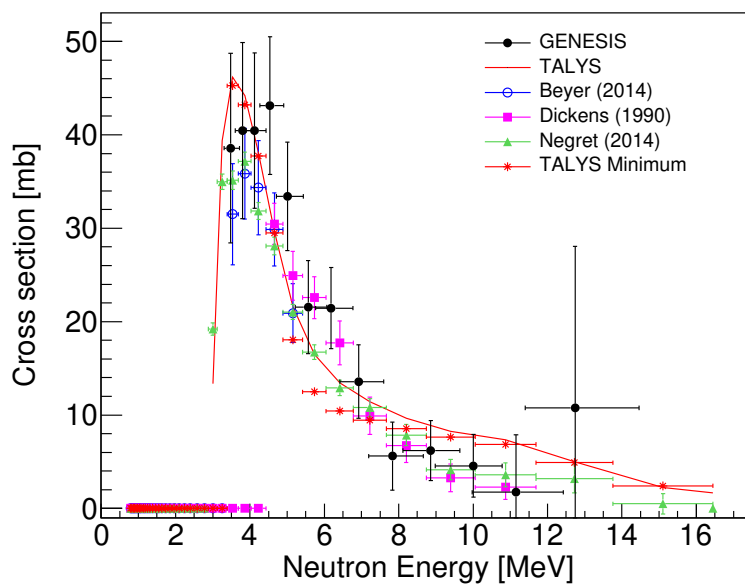


Figure 8.10: 2094.9 keV production at 49.2 degrees

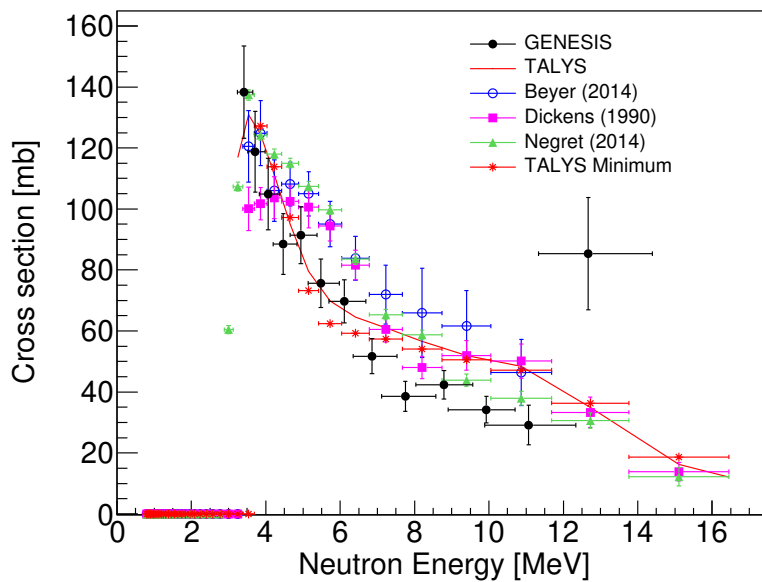


Figure 8.11: 2113.1 keV production at 49.2 degrees

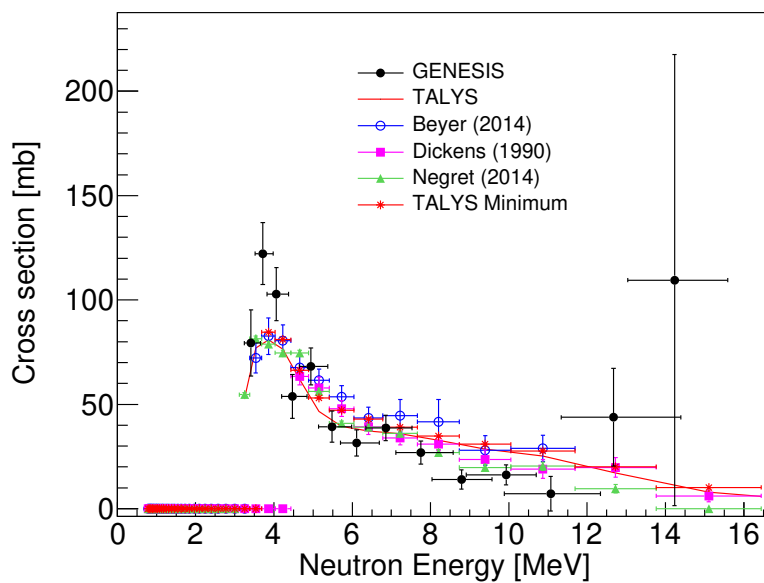


Figure 8.12: 2273.2 keV production at 49.2 degrees

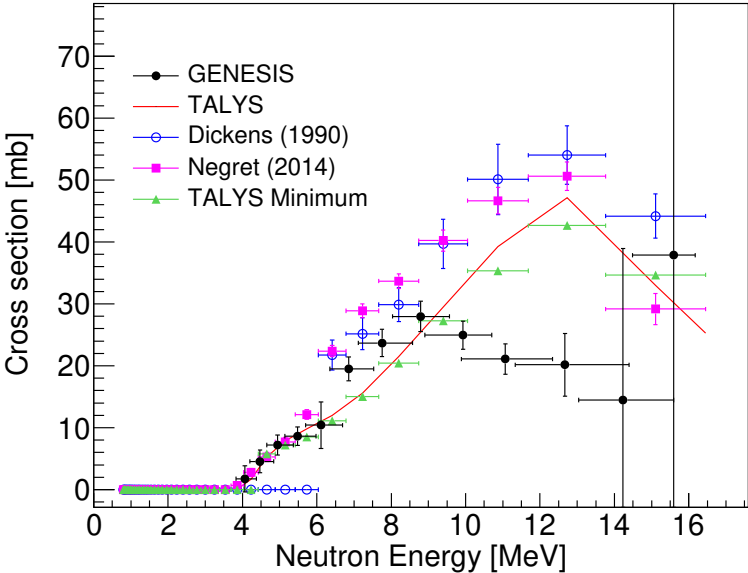


Figure 8.13: 1670.8 keV production at 49.2 degrees

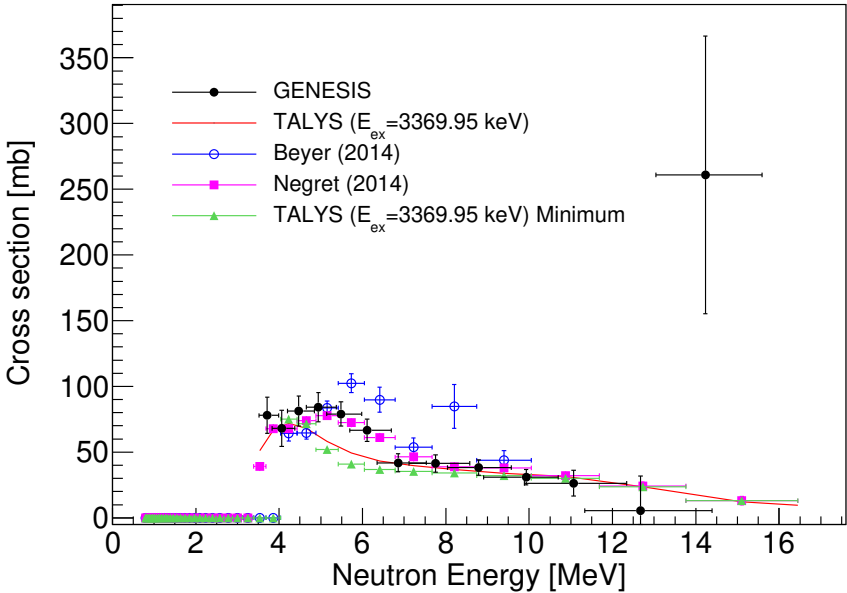


Figure 8.14: 2523.1 keV production at 49.2 degrees

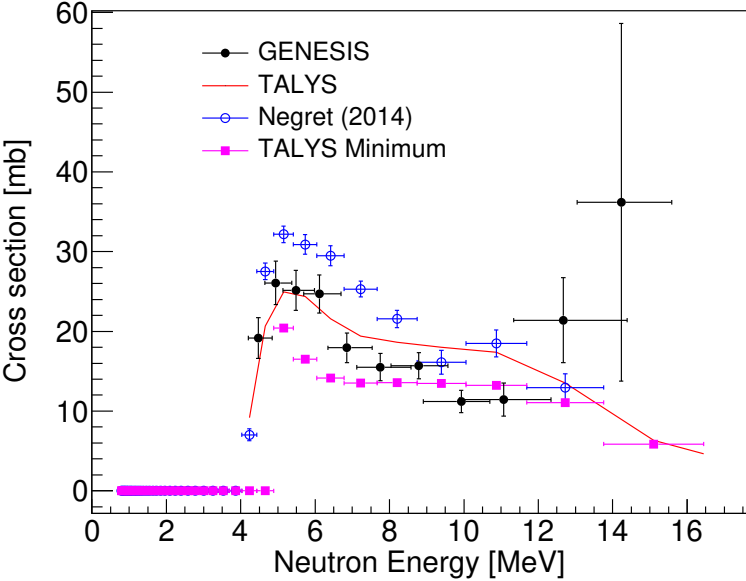


Figure 8.15: 2034.8 keV production at 49.2 degrees

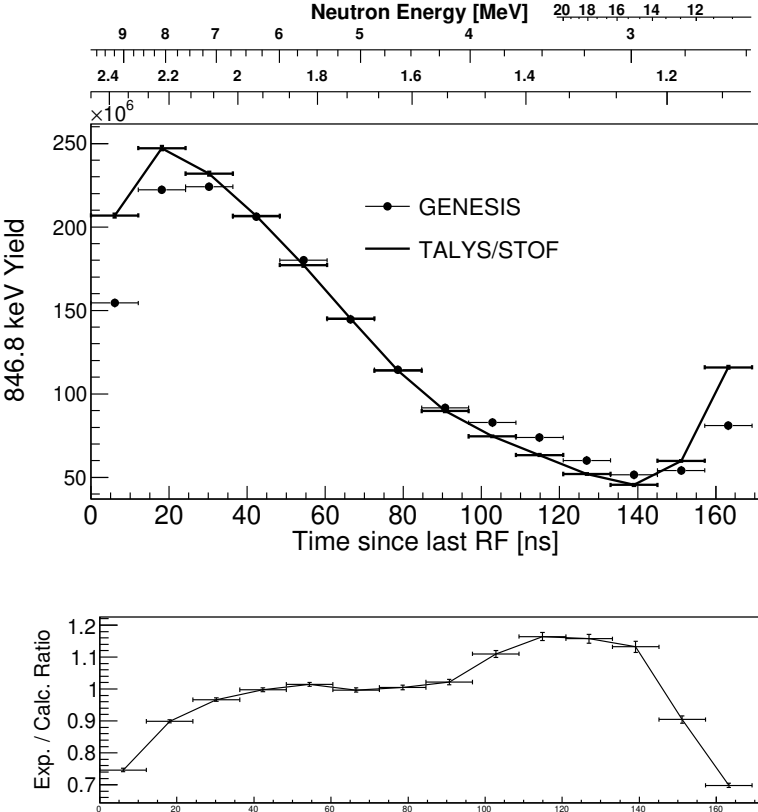
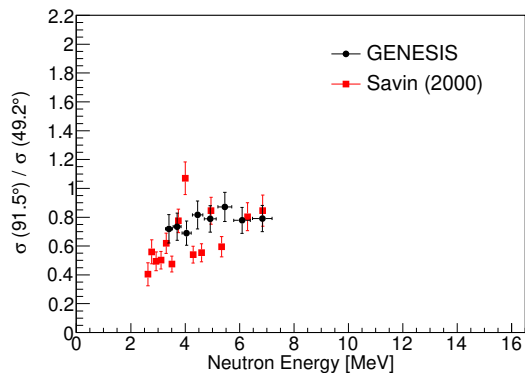
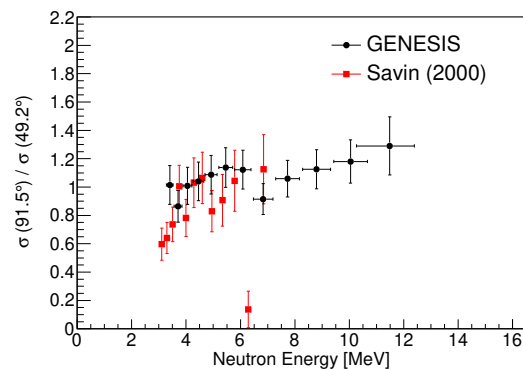


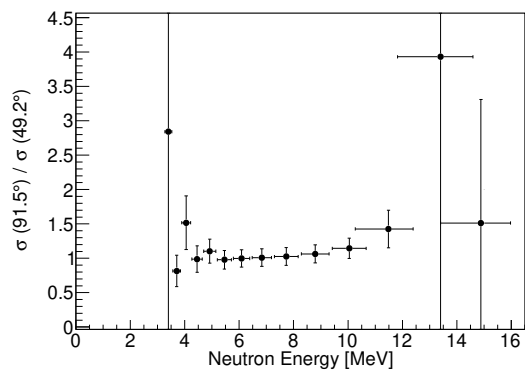
Figure 8.16: Experimental and calculated 846.8 keV gamma yield versus Time-since-last-RF. The TALYS calculation used the minimum parameters.



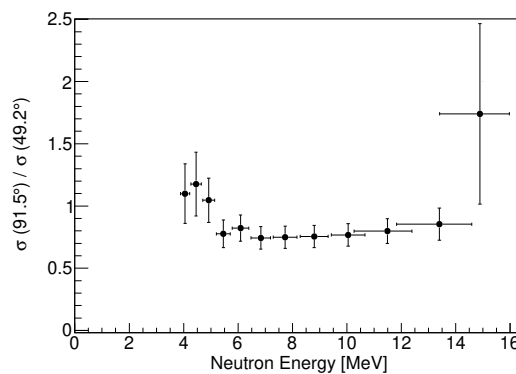
(a) Ratio of the 1238 keV gamma production at the two GENESIS angles



(b) Ratio of the 1811 keV gamma production at the two GENESIS angles

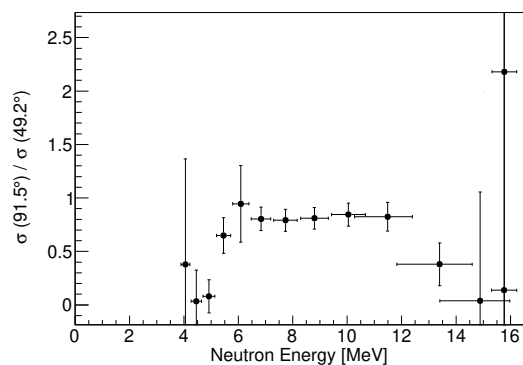


(c) Ratio of the 1038 keV gamma production at the two GENESIS angles

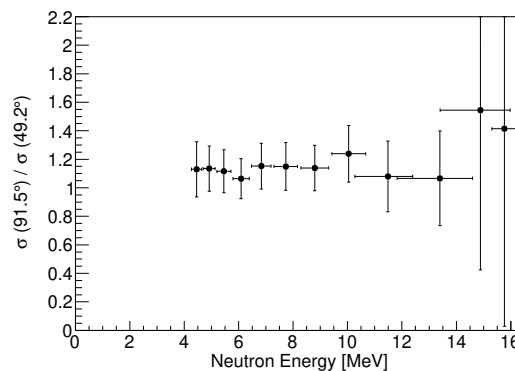


(d) Ratio of the 1303 keV gamma production at the two GENESIS angles

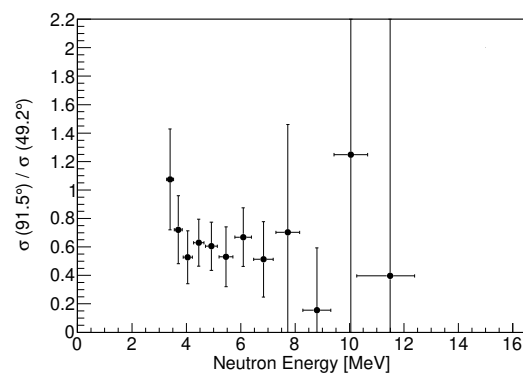
Figure 8.17: Ratio of gamma-ray yields measured at the two GENESIS CLOVER angles. Where available, the GENESIS data is compared to the measurement by Savin [92].



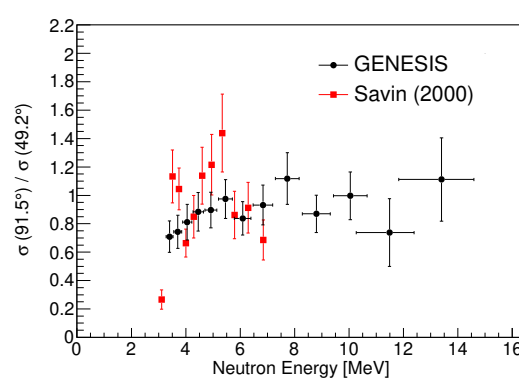
(a) Ratio of the 1670 keV gamma production at the two GENESIS angles



(b) Ratio of the 2035 keV gamma production at the two GENESIS angles



(c) Ratio of the 2095 keV gamma production at the two GENESIS angles



(d) Ratio of the 2113 keV gamma production at the two GENESIS angles

Figure 8.18: Ratio of gamma-ray yields measured at the two GENESIS CLOVER angles. Where available, the GENESIS data is compared to the measurement by Savin [92].

Chapter 9

Towards $n - \gamma$ Coincidence Measurements

The ability to perform simultaneous measurements of gamma-ray production cross sections and secondary neutron energy/angle distributions is a novel contribution to the nuclear data field. However, the simultaneous measurement is not the only novel contribution GENESIS can offer; the coupling of high-resolution gamma spectroscopy to the array of neutron detectors also allows for the measurement of coincident secondary gamma-ray and neutron energy/angle distributions:

$$\frac{d\sigma}{dE_n dE_{n'} d\Omega_{n'} dE_\gamma d\Omega_\gamma} \quad (9.1)$$

Properly measuring this quintuple differential cross section requires careful experimental planning due to the low coincident event efficiency, but would eliminate significantly the amount of background in the measurement. The integration of this differential cross section would require developments in the theoretical understanding of the angular correlations between the emitted neutron and cascade gamma rays following inelastic scattering. These correlations are not currently predicted by the nuclear reaction codes commonly used for evaluation TALYS [68] and Empire [69]).

The data taken on ^{56}Fe is not sufficient to determine the quintuple differential cross section. The reason the ^{56}Fe measurement cannot be used is because of the loss of 10 of the EJ-309 detectors and the 14 MeV TTDB on Carbon neutron yield was less than for other GENESIS experiments with the same beam. Nevertheless, ^{56}Fe is an ideal nucleus for the measurement of this cross section because the 2_1^+ excited state is populated in almost every gamma cascade meaning almost every inelastically scattered neutron will be in coincidence with the 846.8 keV gamma-ray. The ^{56}Fe data can therefore be analyzed to determine what experimental conditions, besides the addition of more HPGe detectors, a higher deuteron beam current, and better neutron transmission from the break-up to scattering target, could change in order to enable such a measurement.

Figure 9.1 shows the signal-to-noise ratio (SNR) in the neutron detectors, with PSD constraints applied to select neutron events, for two data sets, one with a tag on the 846.8 keV

gamma-ray and one without. The SNR improves by as much as an order of magnitude with

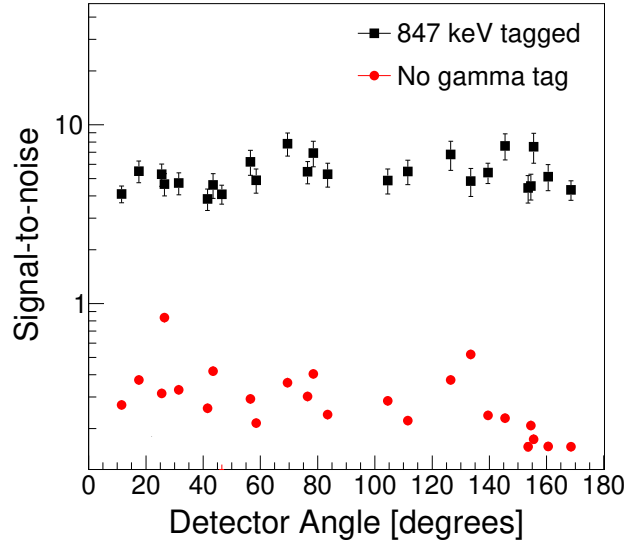


Figure 9.1: Signal-to-noise ratio for the neutron detectors with and without a coincident 846.8 keV gamma-ray detection in any of the CLOVER leaves.

the gamma tag by eliminating a large portion of the neutron beam that scattered off air as it travels from the break-up target, making a measurement of the secondary neutron distribution from inelastic scattering cleaner. Additionally, the gamma-tag removes the elastic scattering contributions to the secondary neutron distribution, a common source of uncertainty in other measurements [14] [17].

Each data point in Figure 9.1 can be expanded into a two-dimensional Time-since-last-RF versus secondary neutron energy space. The secondary neutron energy is calculated using the arrival time of the 846.8 keV gamma and so the timing resolution of the CLOVER detectors determines the energy resolution. Figure 9.2 shows the yield of neutrons in coincidence with the 846.8 keV gamma for Detector 8 as a function of Time-since-last-RF. Also shown are the neutrons in coincidences with regions to the left and right of the 846.8 keV peak to be used a random-coincidence background subtraction.

The background-subtracted distribution from Figure 9.2 can be expanded further into outgoing neutron energy, shown in Figure 9.3 for Detector 8 at Time-since-last-RF between 16-24 ns. The problem with this measurement becomes clear in this figure; the number of events is too small and the energy resolution is too low to perform meaningful spectroscopy. The neutron detectors can be grouped into angular bins of approximately 20° to improve the statistics, with at least two detectors present in each angular bin. Table 9.1 gives a potential grouping scheme to maximize the count rate at the neutron detector angles based on the ^{56}Fe run locations. This grouping was not possible with the ^{56}Fe experiment, especially at forward angles where the direct contributions to the inelastically scattered neutron distribution is

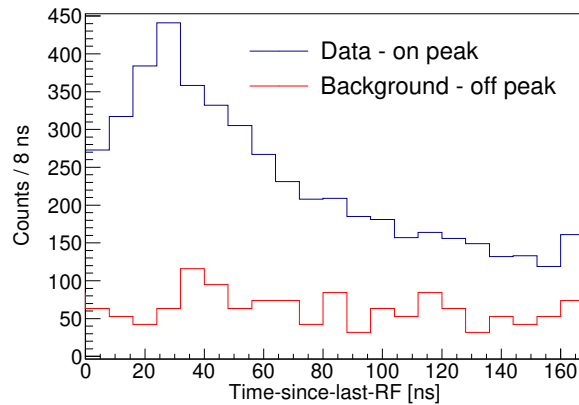


Figure 9.2: Neutron/846.8 keV gamma coincidence yield for EJ-309 detector 8 and both CLOVER detectors as a function of Time-since-last-RF. The red line is the yield in coincidence with portions of the gamma-ray spectrum to the left and right of the 846.8 keV peak and represents the random-coincidence background rate.

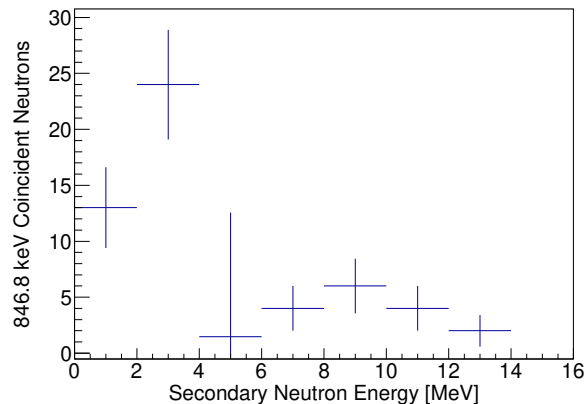


Figure 9.3: Outgoing neutron energy spectrum for neutrons in coincidence with the $E_\gamma = 846.8$ keV transition in ^{56}Fe for EJ-309 Detector 8.

greatest. Future experiments could adjust the locations of some detectors to narrow the range of angles covered by each group while maintaining a negligible inter-element scattering fraction (Sec 2.2).

Figure 9.4 shows this same distribution for neutrons in coincidence with the yrast $4_1^+ \rightarrow 2_1^+$ transition ($E_\gamma = 1238.3$ keV). This state is also strongly fed in the gamma cascade following inelastic scattering, but the number of coincidence events in Fig. 9.4 is significantly less than Fig. 9.3.

Another possibility to increase the coincidence rate is to bring the scintillator detectors

Angular Coverage	Detectors	Average Radial Distance [cm]
$13.1^\circ - 20.0^\circ$	8, 19	72.5
$28.0^\circ - 37.7^\circ$	7, 17, 18	61.8
$47.3^\circ - 54.9^\circ$	6, 16, 25	52.1
$65.2^\circ - 67.7^\circ$	5, 24	48.0
$83.1^\circ - 95.0^\circ$	4, 15, 23	41.7
$114.5^\circ - 117.9^\circ$	3, 14, 22	46.1
$132.6^\circ - 136.5^\circ$	13, 21	55.8
$139.5^\circ - 148.1^\circ$	2, 12, 20	68.9
$155.3^\circ - 157.3^\circ$	1, 9, 11	83.4
$163.2^\circ - 168.6^\circ$	0, 10	87.1

Table 9.1: Potential grouping of all neutron detectors into angles for $n\gamma$ coincidence measurements

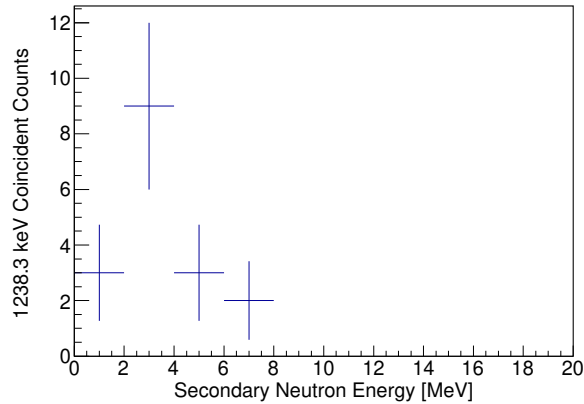


Figure 9.4: Outgoing neutron energy spectrum for neutrons in coincidence with the $E_\gamma = 1238.3$ keV transition in ^{56}Fe for EJ-309 Detector 8.

closer to the scattering target thereby increasing significantly the geometric efficiency. Doing this would eliminate all resolution on outgoing neutron energy from TOF, reduce the resolution on the outgoing neutron angle, and increase the amount of inter-element scatter, but the quality of information contained in the light yield spectra would remain the same. Figure 9.5 shows the light yield in Detector 8 versus Time since last RF for neutrons in coincidence with an 846.8 keV gamma in either of the CLOVER detectors. The statistics are small but the general shape of the distribution is similar to Figure 7.1 with the exception that the edge corresponds not to elastic scattering but inelastic scattering to the first excited state. Bringing this detector from 70.0 cm from the center of the array to ~ 20 cm would increase the number of events in this spectrum by an order of magnitude.

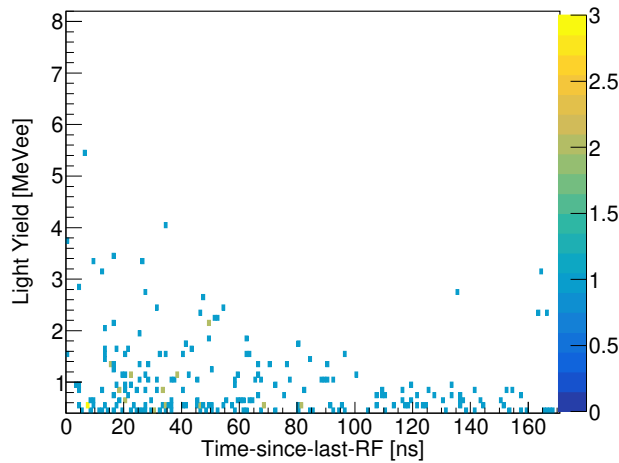


Figure 9.5: Time since last RF versus light yield for neutrons in EJ-309 Detector 8 in coincidence with an 846.8 keV gamma detected by either CLOVER.

In summary, there are two different paths that could be taken to realize a full neutron-gamma coincidence measurement at GENESIS. One way is to add more γ -detectors, ensure the quality of the neutron beam, and run for a long time on an isotope that has a strong collector state like the first excited state in ^{56}Fe . The second way is to bring the organic scintillator detectors closer to the target which would eliminate the outgoing neutron energy resolution and reduce the outgoing neutron angular resolution, but would increase statistics and maintain the ability to obtain incoming neutron energy information.

Chapter 10

Conclusion

GENESIS is a new experimental platform that couples an array of HPGe detectors to an array of organic liquid scintillators to perform simultaneous measurements of secondary neutrons and gamma-rays produced following neutron scattering on thin samples. The characteristics of this array were measured using calibrated gamma-ray sources and an encapsulated ^{252}Cf spontaneous fission source. A GEANT4 model of the array was developed and benchmarked against experimental data. The properties of the array that were determined are listed in Table 10.1 with references to where the details of the experimental and modeling work were discussed.

The preceding chapters presented the details of measurements of secondary neutron energy and angle distributions (Chapter 7) and production cross sections for 11 gamma rays emitted following neutron inelastic scattering (Chapter 8) on ^{56}Fe with GENESIS. Two analysis methods were used to determine the cross sections, a traditional approach and a new forward modeling approach. The forward modeling analysis was developed because of the existence of frame overlap of the TTDB neutron beams used in GENESIS experiments (Sec. 5.1). Given the amount and quality of historical data, the results of the measurements were not expected to change the understanding of neutron reactions with ^{56}Fe . Rather, the goal was to establish GENESIS as an experimental platform capable of performing the simultaneous measurement and to validate the forward modeling analysis approach of experimental neutron elastic and inelastic scattering data.

The threshold for the production of the 1238.3 keV gamma ray partially eliminated the frame overlap allowing for the direct calculation of the cross section between 3.4-6.8 MeV which was found to be in agreement with previous measurements. The production cross section for the 1810.8 keV gamma ray was measured between 3.4-11.1 MeV and also found to be in agreement with previous measurements. The cross sections for eight gamma rays coming from the $E_{ex} = 2941.5$ keV level and above were measured from threshold to 14.2 MeV. At neutron energies above 8 MeV, the cross sections for the 1037.8 keV, 1303.4 keV, and 1670.8 keV gamma rays disagreed with previous measurements (see Sec. 8.2). The production cross section for the 846.8 keV gamma ray was determined using a TALYS-based forward modeling approach. The forward model also yielded cross sections, across the whole

neutron energy range, for the other ten gamma rays. For these reactions, the forward modeling and direct calculations agreed, except for the three transition noted above, where there is disagreement above 8 MeV. The production cross section of the 2523.1 keV gamma ray from the forward modeling analysis disagreed with the results of the direct approach. This is because the measured production cross section is not, as previously reported in the literature, attributable solely to the $2_4^+ \rightarrow 2_1^+$ transition but includes the contribution from the $2_{10}^+ \rightarrow 4_1^+$, $E_\gamma = 2523.09$ keV transition. The uncertainties and neutron energy resolution on the cross sections obtained from the direct analysis technique are worse than the measurement by Negret [9] but the coupling of the GENESIS data with the forward modeling provides a new set of information about the TALYS nuclear reaction model parameters that obtain the best fit. Additionally, the agreement between the two analysis approaches indicates that the forward modeling analysis and any assumptions contain within it are valid and can therefore be expected to work for measurements on other nuclei, including those that lack the rich historical data that ^{56}Fe has.

GENESIS was also used to determine secondary neutron energy and angle distributions following elastic and inelastic scattering on ^{56}Fe . The forward modeling approach was used to find a set of TALYS parameters that best match the observed data. The optimal nOMP parameters that were found agree well with previously established values which was expected given the wealth of historical data on ^{56}Fe and its use in global nOMP parameter optimizations [93]. The results of TALYS calculations with the optimal parameters were compared to the ENDF/B-VIII.0 library and found to agree except at low and high incident neutron energy where the uncertainty on the measured neutron beam spectrum is greatest.

The gradient-descent minimizer Minuit2 was used in the forward modeling analysis to find the best-fit TALYS parameters and calculate the covariances between them. This was done by calculating χ^2 of the neutron and gamma data simultaneously. The covariance matrix is shown in Figure 10.1. The covariance matrix was used to determine uncertainties on the secondary neutron and gamma ray production cross sections calculated with TALYS.

The work presented in Chapters 7 and 8 could be improved in a few ways. The method to select the parameters included in the forward modeling could be improved. The method to select parameters outlined in Sec. 4.2 can be used for other nuclei but care will need to be paid to interdependencies not covered. Additionally, for experiments conducted at higher deuteron beam energies, the importance of pre-equilibrium processes will increase, and the relevant keywords will therefore need to be studied. A different minimization algorithm may be beneficial, especially one that can take advantage of multi-threading and one that can ensure that the minimum found is global. Chapter 9 discussed the experimental conditions necessary for a novel measurement of the correlations between discrete gamma rays and secondary neutron energy and angle distributions. The cost to implement the suggestions in that chapter would be minimal.

Recent work by the Cross Section Evaluation Working Group Covariance Committee has lead to the development of uncertainty templates [94]. The purpose of these templates is to standardize the reporting of uncertainties on experimentally measured nuclear data to ultimately improve the evaluated libraries. These templates were designed based on

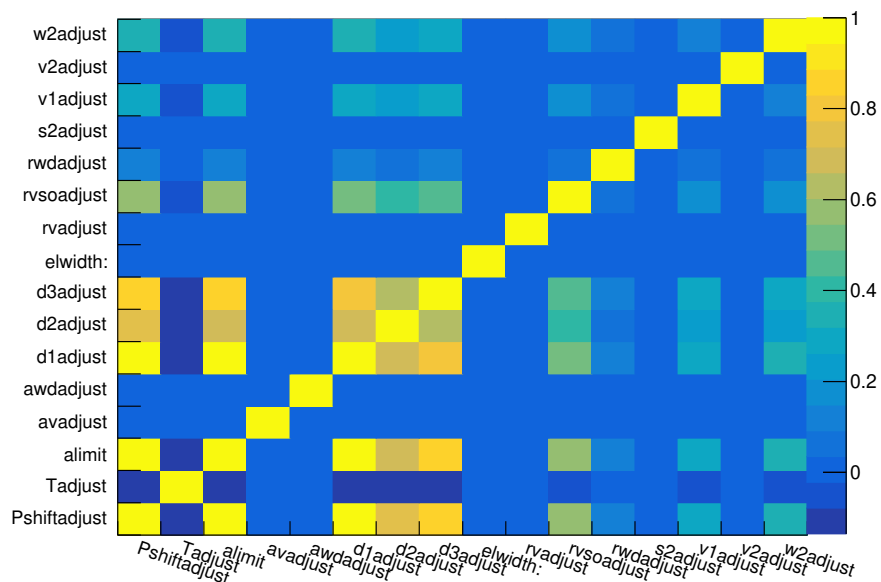


Figure 10.1: Correlation matrix for the simultaneous forward model

the types of experiments and analysis procedures historically used. The work presented in this dissertation is novel in many respects, including being the first to use the uncertainty templates, and many of the uncertainties presented in the template for (n, xn) reactions are not directly applicable [17]. For example, the neutron source used here, TTDB on Carbon, was not considered and neither was the sToF detector used to measure and monitor the neutron flux. The forward modeling analysis procedure is novel. Similar work by Kelly *et al.* [29] and Pirovano *et al.* [15] were mentioned but were not analyzed in depth, and the work developed here differs in some significant aspects. Nevertheless, many of the uncertainties included in the template for (n, xn) reactions are present and are presented in Table 10.1. The location in the text where the uncertainties are discussed is also given in the table.

Category	Quantity	Uncertainty	Description
Neutron Beam	Deuteron time spread	4 ns	Sec. 3.1
	Flight path	0.014%	Sec. 2.1
	Neutron beam spectrum	1.8%	Sec. 2.1
	Activation foil normalization	0.408×10^9 n/sr/ μ C	Sec. 6.3
Scattering target	Target mass	1×10^{-4} g	Sec. 6.1
	Target thickness	6.97%	Sec. 6.1
	Multiple scattering	2.235%	Sec. 6.1
	Isotopic composition	0.02%	Sec. 6.1
Gamma Production	Time resolution	3.3 ns	Sec. 3.1
	Efficiency	1 – 4.5%	Sec. 3.3
	Angle	$5.46^\circ - 7.03^\circ$	Sec 2.1
Neutron Production	Time resolution	0.281 ns	Sec. 3.1
	Efficiency [1.2-2.0 MeV]	1.35 – 4.56%	Sec. 3.3
	Efficiency [2.0-8.0 MeV]	0.83 – 1.42%	Sec. 3.3
	Efficiency [8.0-14.0 MeV]	1.05 – 2.59%	Sec. 3.3
	Angle	$1.22^\circ - 2.58^\circ$	Sec 2.1

Table 10.1: Summary of uncertainties or corrections in the measurement of gamma-ray production and secondary neutron energy/angle distributions, based on [17].

Bibliography

- [1] F. Bostelmann, G. Ilas, and W.A. Wieselquist. “Nuclear Data Sensitivity Study for the EBR-II Fast Reactor Benchmark Using SCALE with ENDF/B-VII.1 and ENDF/B-VIII.0”. In: *J. Nucl. Eng.* 2 (2021), pp. 345–367. DOI: doi.org/10.3390/jne2040028.
- [2] M.B. Chadwick et al. “ENDF/B-VII.1 Nuclear Data for Science and Technology: Cross Sections, Covariances, Fission Product Yields and Decay Data”. In: *Nuclear Data Sheets* 112.12 (2011). Special Issue on ENDF/B-VII.1 Library, pp. 2887–2996. ISSN: 0090-3752. DOI: <https://doi.org/10.1016/j.nds.2011.11.002>. URL: <https://www.sciencedirect.com/science/article/pii/S009037521100113X>.
- [3] D.A. Brown et al. “ENDF/B-VIII.0: The 8th Major Release of the Nuclear Reaction Data Library with CIELO-project Cross Sections, New Standards and Thermal Scattering Data”. In: *Nuclear Data Sheets* 148 (2018). Special Issue on Nuclear Reaction Data, pp. 1–142. ISSN: 0090-3752. DOI: <https://doi.org/10.1016/j.nds.2018.02.001>. URL: <https://www.sciencedirect.com/science/article/pii/S0090375218300206>.
- [4] F. Bostelmann et al. *Nuclear Data Assessments for Advanced Reactors*. Oak Ridge National Laboratory, 2001.
- [5] S. McConchie et al. *Transportable, Low-dose Active Fast-Neutron Imaging*. Oak Ridge National Laboratory, 2017.
- [6] P.A. Hausladen et al. *Induced-Fission Imaging of Nuclear Material*. Oak Ridge National Laboratory.
- [7] Seth McConchie et al. *Assessment of Modeling and Nuclear Data Needs for Active Neutron Interrogation*. Tech. rep. ORNL/TM-2021/1900. Oak Ridge National Laboratory, Apr. 2021. DOI: [10.2172/1778086](https://doi.org/10.2172/1778086).
- [8] M. Herman et al. “Evaluation of Neutron Reactions on Iron Isotopes for CIELO and ENDF/B-VIII.0”. In: *Nuclear Data Sheets* 148 (2018), pp. 214–253. DOI: doi.org/10.1016/j.nds.2018.02.004.
- [9] A. Negret et al. “Cross-section measurements for the $^{56}\text{Fe}(n, xn\gamma)$ reactions”. In: *Phys. Rev. C* 90 (2014). DOI: [10.1103/PhysRevC.90.034602](https://doi.org/10.1103/PhysRevC.90.034602).

- [10] R. Beyer et al. “Inelastic scattering of fast neutrons from excited states in ^{56}Fe ”. In: *Nuclear Physics A* 927 (2014), pp. 41–52. DOI: <http://dx.doi.org/10.1016/j.nuclphysa.2014.03.010>.
- [11] J.K. Dickens, J.H. Todd, and D.C. Larson. *Cross Sections for Production of 70 Discrete-Energy Gamma Rays Created by Neutron Interactions with ^{56}Fe for E_n to 40 MeV: Tabulated Data*. Oak Ridge National Laboratory, 1990.
- [12] A. Mittler, J. Nardini, and G.P. Couchell. “Measurements of neutron inelastic scattering cross sections for natural iron”. University of Wisconsin, Madison, 1975.
- [13] D.L. Smith. *Fast-neutron gamma-ray production from elemental iron: $E_n \leq 2$ MeV*. Argonne National Laboratory, 1976.
- [14] A.P.D. Ramirez et al. “Neutron scattering cross section measurements for ^{56}Fe ”. In: *Phys. Rev. C* 95 (2017). DOI: [10.1103/PhysRevC.95.064605](https://doi.org/10.1103/PhysRevC.95.064605).
- [15] E. Pirovano et al. “Cross section and neutron angular distribution measurements of neutron scattering on natural iron”. In: *Phys. Rev. C* 99 (2019), p. 024601. DOI: [10.1103/PhysRevC.99.024601](https://doi.org/10.1103/PhysRevC.99.024601).
- [16] A.B. Smith. “Neutron scattering and models: iron”. In: *Nuclear Physics A* 605 (1969), pp. 269–289.
- [17] J.R. Vanhoy et al. “Templates of expected measurement uncertainties for (n,xn) cross sections”. In: *EPJ Nuclear Sci. Technol.* 9 (31 2023). DOI: [10.1051/epjn/2023019](https://doi.org/10.1051/epjn/2023019).
- [18] K.P. Harrig et al. “Neutron Spectroscopy for pulsed beams with frame overlap using a double time-of-flight technique”. In: *Nuclear Instruments and Methods in Physics Research Section A: Accelerators, Spectrometers, Detectors and Associated Equipment* 877 (2018), pp. 359–366. ISSN: 0168-9002. DOI: <https://doi.org/10.1016/j.nima.2017.09.051>. URL: <http://www.sciencedirect.com/science/article/pii/S0168900217310215>.
- [19] D. L. Bleuel et al. “Characterization of a tunable quasi-monoenergetic neutron beam from deuteron breakup”. In: *Nuclear Inst. and Methods in Physics Research B* 261 (2007), pp. 974–979.
- [20] James E. Bevins et al. “Performance evaluation of an energy tuning assembly for neutron spectral shaping”. In: *Nuclear Inst. and Methods in Physics Research A* 923 (2019), pp. 79–87.
- [21] J.T. Morrell et al. “Secondary neutron production from thick target deuteron breakup”. In: *Phys. Rev. C* 108 (2023). DOI: [10.1103/PhysRevC.108.024616](https://doi.org/10.1103/PhysRevC.108.024616).
- [22] R. Serber. “The Production of High Energy Neutrons by Stripping”. In: *Phys. Rev.* 72 (1947), pp. 1008–1016.
- [23] J. Morrell. “Next-Generation Isotope Production via Deuteron Breakup”. PhD thesis. University of California, Berkeley, 2021.

- [24] G.W. Schweimer. “Fast neutron production with 54 MeV deuterons”. In: *Nuclear Physics A* 100.3 (1967), pp. 537–544. ISSN: 0375-9474. DOI: [https://doi.org/10.1016/0375-9474\(67\)90122-4](https://doi.org/10.1016/0375-9474(67)90122-4).
- [25] K. A. Weaver et al. “Neutron Spectra from Deuteron Bombardment of D, Li, Be, and C”. In: *Nuclear Science and Engineering* 52.1 (1973), pp. 35–45. DOI: 10.13182/NSE73-A23287.
- [26] J. P. Meulders et al. “Fast Neutron Yields and Spectra from Targets of Varying Atomic Number Bombarded with Deuterons from 16 to 50 MeV”. In: *Phys. Med. Biol.* 20.2 (1975), pp. 235–243.
- [27] M. A. Lone et al. “Thick Target Neutron Yields and Spectral Distributions from the ${}^7\text{Li}(\text{d},\text{n})$ and ${}^9\text{Be}(\text{d},\text{n})$ Reactions”. In: *Nuclear Inst. and Methods* 143 (1977), pp. 331–344.
- [28] M.J. Saltmarsh et al. “Characteristics of an intense neutron source based on the d+Be reaction”. In: *Nuclear Instruments and Methods* 145.1 (1977), pp. 81–90. ISSN: 0029-554X. DOI: [https://doi.org/10.1016/0029-554X\(77\)90559-6](https://doi.org/10.1016/0029-554X(77)90559-6).
- [29] K.J. Kelly et al. “Correlated $n - \gamma$ angular distributions from the $Q = 4.4398$ MeV ${}^{12}\text{C}(n, n'\gamma)$ reaction for incident neutron energies from 6.5 MeV to 16.5 MeV”. In: *Phys. Rev. C* 104 (2021). DOI: <https://doi.org/10.1103/PhysRevC.104.064614>.
- [30] J. Allison et al. “Recent developments in GEANT4”. In: *Nuclear Inst. and Methods in Physics Research A* 835 (2016), pp. 186–225. DOI: 10.1016/j.nima.2016.06.125.
- [31] Eljen Technology. *Neutron/Gamma PSD EJ-301, EJ-309*. <https://eljentechnology.com/products/liquid-scintillators/ej-301-ej-309>. Accessed: 5 Oct 2021.
- [32] Hamamatsu Photonics. *Photomultiplier tube assembly H1949-51*. Accessed: 3 Dec 2021. URL: <https://www.hamamatsu.com/eu/en/product/type/H1949-51/index.html>.
- [33] Scionix Holland B.V. *Compton suppression spectrometry*. <https://scionix.nl/wp-content/uploads/2017/07/Compton-suppression-shields.pdf>.
- [34] Ortec. *GEM Series Coaxial HPGe Detector Product Configuration Guide*. <https://www.ortec-online.com/-/media/ametektortec/brochures/g/gem.pdf?la=en&revision=cf45d0c5-a261-4a9f-882d-443a30d03342>.
- [35] Saint-Gobain Crystals. *LaBr Scintillation Crystal*. <https://www.crystals.saint-gobain.com/radiation-detection-scintillators/crystal-scintillators/lanthanum-bromide-labr3>.
- [36] Hamamatsu Photonics. *Photomultiplier tube assembly R2083*. https://www.hamamatsu.com/content/dam/hamamatsu-photonics/sites/documents/99_SALES_LIBRARY/etd/R2083_R3377_TPMH1227E.pdf.
- [37] Glenn F. Knoll. “Radiation Detection and Measurement”. In: Third. John Wiley & Sons, Inc., 2000.

- [38] J.B. Birks. *The Theory and Practice of Scintillation Counting*. Pergamon Press, 1967.
- [39] Eljen Technology. *Silicone Grease EJ-550, EJ552*. <https://eljentechnology.com/products/accessories/ej-550-ej-552>. Accessed: 3 Dec 2021.
- [40] CAEN Technologies. *R8033*. <https://www.caen.it/products/r8033/>. Accessed: 3 Dec 2021.
- [41] CAEN Technologies. *R1470ET*. <https://www.caen.it/products/r1470et/>. Accessed: 3 Dec 2021.
- [42] Kenneth S. Krane. *Introductory Nuclear Physics*. John Wiley and Sons, Inc., 1988.
- [43] I.Y. Lee. “Gammasphere”. In: *Proceedings of the Workshop on Gammasphere Physics*. Ed. by M.A. Deleplanque, I.Y. Lee, and A.O. Macchiavelli.
- [44] G. Duchêne et al. “The Clover: a new generation of composite Ge detectors”. In: *Nuclear Inst. and Methods in Physics Research A* 432 (1999), pp. 90–110.
- [45] Hamamatsu Photonics. *Photomultiplier tube R3998-02*. <https://www.hamamatsu.com/us/en/product/type/R3998-02/index.html>. Accessed: 3 Dec 2021.
- [46] iseg. *NHR: High Precision Versatile High Voltage Module in NIM Standard*. <https://iseg-hv.com/en/products/detail/NHR>. Accessed: 3 Dec 2021.
- [47] Mesytec. *MDPP-16*. <https://www.mesytec.com/products/nuclear-physics/MDPP-16.html>. Accessed: 3 Dec 2021.
- [48] Andreas Ruben et al. *A New, Versatile, High-performance Digital Pulse Processor with Application to Neutron/Gamma-Ray Pulse-Shape Discrimination in Scintillator Detectors*. July 2018. DOI: 10.13140/RG.2.2.14187.18727.
- [49] mesytec. *MDPP-16 SCP/RCP*. Accessed: 9 Jan 2022.
- [50] mesytec. *Software Module MDPP-16-QDC*. https://www.mesytec.com/products/datasheets/MDPP-16_QDC.pdf. Accessed: 9 Jan 2022.
- [51] LeCroy. *429A Quad Logic Fan-in/Fan-Out*. <https://teledynelecroy.com/lrs/dsheets/428.htm>. Accessed: 3 Dec 2021.
- [52] J. A. Brown et al. “Proton light yield in organic scintillators using a double time-of-flight technique”. In: *Journal of Applied Physics* 124.4 (July 2018). ISSN: 0021-8979. DOI: 10.1063/1.5039632.
- [53] W. Mannhart. “Status of the Cf-252 fission neutron spectrum evaluation with regard to recent experiments”. In: *International Nuclear Data Committee: Consultants’ meeting on physics of neutron emission in fission*. International Atomic Energy Agency, 1989, pp. 305–336. URL: <https://www.osti.gov/servlets/purl/1414710>.
- [54] T.A. Laplace et al. “Comparative scintillation performance of EJ-309, EJ-276, and a novel organic glass”. In: *Journal of Instrumentation* 15.11 (Nov. 2020), P11020. DOI: 10.1088/1748-0221/15/11/P11020. URL: <https://dx.doi.org/10.1088/1748-0221/15/11/P11020>.

- [55] S. Yoshida et al. “Light output response of KamLAND liquid scintillator for protons and ^{12}C nuclei”. In: *Nuclear Instruments and Methods in Physics Research Section A: Accelerators, Spectrometers, Detectors and Associated Equipment* 622 (2010), pp. 574–582. ISSN: 0168-9002. DOI: [10.1016/j.nima.2010.07.087](https://doi.org/10.1016/j.nima.2010.07.087).
- [56] T.A. Laplace et al. “Modeling ionization quenching in organic scintillators”. In: *Materials Advances* 3 (2022), pp. 5871–5881. DOI: [10.1039/d2ma00388k](https://doi.org/10.1039/d2ma00388k).
- [57] G. Dietze and H. Klein. “Gamma-calibration of NE 213 scintillation counters”. In: *Nuclear Instruments and Methods in Physics Research* 193.3 (1982), pp. 549–556. ISSN: 0167-5087. DOI: [https://doi.org/10.1016/0029-554X\(82\)90249-X](https://doi.org/10.1016/0029-554X(82)90249-X).
- [58] S. Agostinelli et al. “Geant4 – a simulation toolkit”. In: *Nuclear Instruments and Methods in Physics Research Section A: Accelerators, Spectrometers, Detectors and Associated Equipment* 506.3 (2003), pp. 250–303. ISSN: 0168-9002. DOI: [https://doi.org/10.1016/S0168-9002\(03\)01368-8](https://doi.org/10.1016/S0168-9002(03)01368-8).
- [59] GEANT4 Collaboration. *Guide For Physics List Release 1.1*. Dec. 2022. URL: <https://geant4-userdoc.web.cern.ch/UsersGuides/PhysicsReferenceManual/html/index.html>.
- [60] Emilio Mendoza et al. “New Standard Evaluated Neutron Cross Section Libraries for the GEANT4 Code and First Verification”. In: *IEEE Transactions on Nuclear Science* 61.4 (2014), pp. 2357–2364. DOI: [10.1109/TNS.2014.2335538](https://doi.org/10.1109/TNS.2014.2335538).
- [61] D. L. Bleuel et al. “Precision measurement of relative γ -ray intensities from the decay of ^{61}Cu ”. In: *Applied Radiation and Isotopes* 170 (2021), p. 109625. ISSN: 0969-8043. DOI: <https://doi.org/10.1016/j.apradiso.2021.109625>.
- [62] K. Debertin. “The effect of correlations in the efficiency calibration of germanium detectors”. In: *Nuclear Instruments and Methods in Physics Research Section A: Accelerators, Spectrometers, Detectors and Associated Equipment* 226.2 (1984), pp. 566–568. ISSN: 0168-9002. DOI: [https://doi.org/10.1016/0168-9002\(84\)90084-6](https://doi.org/10.1016/0168-9002(84)90084-6).
- [63] Z. Kis et al. “Comparison of efficiency functions for Ge gamma-ray detectors in a wide energy range”. In: *Nuclear Instruments and Methods in Physics Research Section A: Accelerators, Spectrometers, Detectors and Associated Equipment* 418.2 (1998), pp. 374–386. ISSN: 0168-9002. DOI: [https://doi.org/10.1016/S0168-9002\(98\)00778-5](https://doi.org/10.1016/S0168-9002(98)00778-5).
- [64] D.L. Smith and N. Otuka. “Experimental Nuclear Reaction Data Uncertainties: Basic Concepts and Documentation”. In: *Nuclear Data Sheets* 113 (2012), pp. 3006–3053. DOI: [doi:10.1016/j.nds.2012.11.004](https://doi.org/10.1016/j.nds.2012.11.004).
- [65] A. Arectout et al. “Optimization of the n-type HPGe detector parameters using the “design of experiments” technique”. In: *Radiation Physics and Chemistry* 189 (2021).
- [66] Thiery Granier. “Reanalysis of ^{239}Pu prompt fission neutron spectra”. In: *Physics Procedia* 64 (2015), pp. 183–189.

- [67] William H. Press et al. *Numerical Recipes in C*. Third. Cambridge, UK: Cambridge University Press, 2007.
- [68] A.J. Koning, S. Hilaire, and M.C. Duijvestijn. “TALYS-1.0”. In: *Proceedings of the International Conference on Nuclear Data for Science and Technology*. Ed. by O. Bersillon et al. 2008, pp. 211–214.
- [69] M. Herman et al. “EMPIRE: Nuclear Reaction Model Code System for Data Evaluation”. In: *Nucl. Data Sheets* 108 (2007), pp. 2655–2715.
- [70] W.E. Ormand. *Monte Carlo Hauser-Feshbach computer code system to model nuclear reactions: YAHFC LLNL-TR-824700*. Lawrence Livermore National Laboratory, 2021.
- [71] J. Raynal. *Notes on ECIS94 CEA-N-2772*. CEA Saclay, 1994.
- [72] Arjan Koning, Stephane Hilaire, and Stephane Goriely. *TALYS-1.96/2.0: Simulation of nuclear reactions*. 2021.
- [73] G. R. Satchler. *Introduction to Nuclear Reactions*. 2nd ed. Macmilan Education Ltd., 1990.
- [74] A. Gilbert and A.G.W. Cameron. “A Composite Nuclear-Level Density Formula with Shell Corrections”. In: *Canadian Journal of Physics* 43 (1965).
- [75] H. A. Bethe. “An Attempt to Calculate the Number of Energy Levels of a Heavy Nucleus”. In: *Phys. Rev.* 50 (4 Aug. 1936), pp. 332–341. DOI: 10.1103/PhysRev.50.332. URL: <https://link.aps.org/doi/10.1103/PhysRev.50.332>.
- [76] Eric Sheldon and Douglas M. Van Patten. “Compound Inelastic Nucleon and Gamma-Ray Angular Distributions for Even- and Odd-Mass Nuclei”. In: *Reviews of Modern Physics* 38 (1 1966), pp. 143–186.
- [77] J.R. Huizenga and L.G. Moretto. “Nuclear Level Densities”. In: *Annu. Rev. Nucl. Sci.* 22 (1972), pp. 427–464.
- [78] T. Kawano et al. “Statistical and evaporation models for the neutron emission energy spectrum in the center-of-mass system from fission fragments”. In: *Nuclear Physics A* 913 (2013), pp. 51–70.
- [79] V. A. Plujko et al. *Verification of Models for Calculation of E1 Radiative Strength*. 2008. arXiv: 0802.2183 [nucl-th].
- [80] R. Capote et al. “RIPL – Reference Input Parameter Library for Calculation of Nuclear Reactions and Nuclear Data Evaluations”. In: *Nuclear Data Sheets* 110 (12 Dec. 2009), pp. 3107–3214.
- [81] Rene Brun and Fons Rademakers. “ROOT - An Object Oriented Data Analysis Framework”. In: *Nuclear Inst. and Methods in Physics Research, A* 389 (1997), pp. 81–86. DOI: 10.1016/S0168-9002(97)00048-X.
- [82] Fred James and Matthias Winkler. *Minuit 2*. URL: <https://root.cern.ch/root/html/doc/guides/minuit2/Minuit2.pdf>.

- [83] Fred James. *The Interpretation of Errors*. URL: <https://seal.web.cern.ch/documents/minuit/mnerror.pdf>.
- [84] *National Isotope Development Center*. URL: isotopes.gov.
- [85] J.H. Hubbell and S.M. Seltzer. *Tables of X-Ray Mass Attenuation Coefficients and Mass Energy-Absorption Coefficients from 1 keV to 20 MeV for Elements Z=1 to 92 and 48 Additional Substances of Dosimetric Interest*. 1996. DOI: <https://dx.doi.org/10.18434/T4D01F>.
- [86] J.L. Conlin et al. *Release of ENDF/B-VIII.0-Based ACE Data Files LA-UR-18-24034*. Los Alamos National Laboratory, 2018.
- [87] *MCNP User Manual, Version 5*.
- [88] A. Trkov et al. “IRDF-II: A New Neutron Metrology Library”. In: *Nuclear Data Sheets* 163 (2020), pp. 1–108. ISSN: 0090-3752. DOI: <https://doi.org/10.1016/j.nds.2019.12.001>. URL: <https://www.sciencedirect.com/science/article/pii/S0090375219300687>.
- [89] Huo Junde, Huo Su, and Yang Dong. “Nuclear Data Sheets for A = 56”. In: *Nuclear Data Sheets* 112 (6 2011), pp. 1513–1645. DOI: doi.org/10.1016/j.nds.2011.04.004.
- [90] L.C. Mihailescu et al. “A new HPGe setup at Gelin for measurement of gamma-ray production cross-sections from inelastic neutron scattering”. In: *Nuclear Inst. and Methods in Physics Research, A* 531 (2004), pp. 375–391. DOI: [doi:10.1016/j.nima.2004.05.119](https://doi.org/10.1016/j.nima.2004.05.119).
- [91] A.M. Hurst et al. “The Baghdad Atlas: A relational database of inelastic neutron-scattering (n,n’g) data”. In: *Nuclear Inst. and Methods in Physics Research, A* 995 (2021), p. 165095. DOI: doi.org/10.1016/j.nima.2021.165095.
- [92] M.V. Savin et al. “Evaluation of Angular Distributions and Gamma-Ray Production Cross Sections for Iron”. In: *Journal of Nuclear Science and Technology* 37 (2000), pp. 748–752. DOI: doi.org/10.1080/00223131.2000.10874989.
- [93] A.J. Koning and J.P. Delaroche. “Local and global nucleon optical models from 1 keV to 200 MeV”. In: *Nuclear Physics A* 713 (2003), pp. 231–310.
- [94] Denise Neudecker et al. “emplates of expected measurement uncertainties”. In: *EPJ Nuclear Sci. Tehcnol.* 9 (35 2023). DOI: [10.1051/epjn/2023014](https://doi.org/10.1051/epjn/2023014).

Appendix A

Scintillator Locations

The position of the EJ-309 organic liquid scintillators in the GENESIS array are given in Table A.1.

Detector ID	(x, y, z) [m]	Normal Vector
0	(0.804, 0.162, -0.0227)	(0.812, 0.585, 0)
1	(0.628, 0.285, -0.0261)	(0.812, 0.585, 0)
2	(0.4669, 0.399, -0.0258)	(0.812, 0.585, 0)
3	(0.225, 0.255, -0.342)	(0, 0, -1)
4	(0.0367, 0.253, -0.343)	(0, 0, -1)
5	(-0.175, 0.252, -0.343)	(0, 0, -1)
6	(-0.315, 0.398, -0.027)	(-0.8023, 0.596, 0)
7	(-0.468, 0.275, -0.0274)	(-0.8023, 0.596, 0)
8	(-0.659, 0.151, -0.0278)	(-0.8023, 0.596, 0)
9	(0.839, -0.246, 0.252)	(1, 0, 0)
10	(0.836, 0.0147, 0.254)	(1, 0, 0)
11	(0.767, 0.269, 0.230)	(0, 1, 0)
12	(0.563, 0.2650, 0.231)	(0, 1, 0)
13	(0.367, 0.263, 0.230)	(0, 1, 0)
14	(0.162, 0.261, 0.229)	(0, 1, 0)
15	(-0.0419, 0.258, 0.226)	(0, 1, 0)
16	(-0.241, 0.2575, 0.2255)	(0, 1, 0)
17	(-0.441, 0.2530, 0.2289)	(0, 1, 0)
18	(-0.624, 0.248, 0.219)	(0, 1, 0)
19	(-0.682, 0.00425, 0.247)	(-1, 0, 0)
20	(0.609, -0.0091, 0.441)	(0, 1, 0)
21	(0.403, -0.0100, 0.439)	(0, 1, 0)
22	(0.200, -0.0108, 0.439)	(0, 1, 0)
23	(-0.00012, -0.008, 0.437)	(0, 1, 0)
24	(-0.202, -0.0100, 0.436)	(0, 1, 0)
25	(0.111, -0.0005723, 0.00182)	(0, 1, 0)

Table A.1: Scintillator detector locations relative to the center of the GENESIS frame. The EJ-309 detectors are not pointed at the GENESIS target, so the normal vector of the front face of the detector is given. The neutron beam travels in the $-\hat{x}$ direction.

ProQuest Number: 30818264

INFORMATION TO ALL USERS

The quality and completeness of this reproduction is dependent on the quality and completeness of the copy made available to ProQuest.



Distributed by ProQuest LLC (2024).

Copyright of the Dissertation is held by the Author unless otherwise noted.

This work may be used in accordance with the terms of the Creative Commons license or other rights statement, as indicated in the copyright statement or in the metadata associated with this work. Unless otherwise specified in the copyright statement or the metadata, all rights are reserved by the copyright holder.

This work is protected against unauthorized copying under Title 17, United States Code and other applicable copyright laws.

Microform Edition where available © ProQuest LLC. No reproduction or digitization of the Microform Edition is authorized without permission of ProQuest LLC.

ProQuest LLC
789 East Eisenhower Parkway
P.O. Box 1346
Ann Arbor, MI 48106 - 1346 USA